# Fabrication of Nanostructured ZnO Films by Electrochemical Deposition for Hybrid Solar Cell Application

## (電解析出によるナノ構造酸化亜鉛薄膜の作製とハイブリッド太陽電池への応用)

Jennifer T. Damasco Ty

March 2016

Graduate School of Materials Science
Nara Institute of Science and Technology

# Abstract

In the midst of climate change and environmental sustainability concerns, solar technology is expected to play a big role in energy security due to its renewable source and low carbon emissions. In an effort to reduce the cost of produced electricity, hybrid solar cells are have been intensively investigated as promising approaches to low-cost photovoltaics. Thin and lightweight, hybrid solar cells lead to reduced material costs and compatibility with versatile solution processing methods to reduced fabrication costs.

Among the inorganic semiconductors used in hybrid cells, zinc oxide (ZnO) has particularly gained a lot of interest owing to its stability and optoelectronic properties. Its wide bandgap and high mobility are favorable for efficient electron transport and reduced recombination loss. Furthermore, ZnO possesses a diverse morphologies that can be fabricated by various synthesis methods. In particular, the ZnO nanorod array structure is seen as ideal for hybrid solar cell applications because it provides a huge interfacial area as well as direct charge transport pathways.

For nanostructured ZnO films to succeed in hybrid solar cell applications, its controlled growth must be understood. Among the available methods to grow nanostructured ZnO, the electrochemical deposition process is compatible with the low temperature conditions necessary for fabricating devices on flexible substrates. In this study, the growth of ZnO nanostructured films by electrochemical deposition from a chloride electrolyte is investigated. The resulting films are evaluated on their application in hybrid solar cell devices with a structure of Au/$MoO_3$/P3HT:PCBM/ZnO/ITO.

A background of the study is presented in Chapter 1.

The growth of ZnO nanorods is discussed in Chapter 2. Here, the deposition of a ZnO seed layer on the ITO substrate prior to electrodeposition is shown to influence the growth of nanorods with homogeneous diameters and highly ordered orientation perpendicular to the substrate. Additionally, the effect of decreasing the KCl concentration from 0.1 M to 0.05 M on inhibiting the growth of micron-sized hexagonal flakes and the morphology of the nanorods is demonstrated. A hybrid solar cell with power conversion efficiency (*PCE*) of 2.9% was fabricated.

Growing aluminum-doped ZnO is discussed in Chapter 3. Electrodeposition was conducted with the addition of aluminum chloride hexahydrate as a dopant source. Nanorod arrays with isolated hexagonal flakes were grown at electrolytes with 3 mM $ZnCl_2$ and Al/Zn ratio of 0.5%. Decreasing the KCl concentration from 0.05 M to 0.025 M decreased the number of flakes. Among the devices fabricated, the highest *PCE* of 1.7% was obtained.

Growing fullerene-doped ZnO is discussed in Chapter 4. Here, electrodeposition was conducted by adding a water-soluble fullerene derivative, $C_{60}$ pyrrolidine tris-acid (CPTA), to the electrolyte. Films with high optical transmittance and nanorods were grown successfully. Hybrid solar cells with fullerene-doped ZnO exhibited higher series resistance and improved shunt resistance compared to undoped ZnO. The best *PCE* obtained was 2.2%.

In summary, this research demonstrates the growth of ZnO nanorod arrays by electrochemical deposition for application in hybrid solar cells. The role of nucleation and the concentration of KCl towards the control of nanorod microstructure were demonstrated. In addition, Al-doped ZnO and fullerene-doped ZnO nanostructured films were grown successfully by electrochemical deposition. These results and analysis are valuable in developing nanostructured ZnO films through structural control and doping for hybrid solar cell applications.

# Table of Contents

# Acknowledgements

I am enormously grateful to various individuals who, with their generosity, made this work possible.

I express my sincerest gratitude to my adviser, Prof. Hisao Yanagi, for his guidance, support, and patience throughout my graduate studies.

Many thanks goes to the members my advisory panel, Prof. Yukiharu Uraoka, Prof. Masakazu Nakamura, and Assoc. Prof. Hiroyuki Katsuki. Their valuable advice and comments improved this dissertation.

I would also like to thank Prof. Derck Schlettwein who provided great insight to the study on Al-doped ZnO and to Nadine Dannehl for her help with the study.

I am thankful to all the professors and colleagues in the Quantum Materials Laboratory, past and present, for all the interesting discussions, experiments, and gatherings we shared. Thank you for always taking care of me.

I am thankful to my fellow Filipinos in NAIST; their friendship has made studying in Japan more enjoyable.

I am also thankful to my friends back home who sent well-wishes and prayed for the success of my graduate studies.

Finally, I would like to thank JohnP for his ever constant support and encouragement. Likewise, I thank my parents Jojo and Brenda and my siblings Janille, Don, and Ikka for the many years of love and support.

# 1 Introduction

In the midst of climate change and rising energy needs, more and more nations are pledging to reduce emissions and transition to clean energy. The move is seen as a step towards environmental sustainability. Shifting the world’s energy consumption away from fossil fuels mitigates carbon released to the atmosphere and reduces reliance on non-renewable resources of energy which will eventually be depleted. As one of the clean renewable sources of energy, solar technologies will play a major role in the energy security of the world in the future.

Reducing carbon emissions to the atmosphere will mitigate climate change. Since 1880 up to 2015, the Earth had warmed by 0.94 $^o$C – a high number as an average over the surface of the entire planet. The effect of warming has been felt in the melting of glaciers and more unpredictable weather patterns. Scientists believe that the warming is probably caused by the release of greenhouse gases from human activity. [1] The world derives most of its heat and electricity from burning fossil fuels such as coal, oil, and natural gas. Burning fossil fuels for electricity generation is the largest single source of global greenhouse gas emissions. As a result, tons of carbon dioxide, a potent greenhouse gas, is released into the atmosphere.

Burning fossil fuels for electricity, aside from its emissions, also raises the concern of sustainability. Fossil fuel reserves are finite so they will be depleted eventually. The depletion of fossil fuel reserves poses a threat to the energy security of the world because, as mentioned previously, most of the world’s energy is derived from fossil fuels. Researchers cannot say for sure how much more is left or how long it will last. Therefore, the development of energy sources with low emissions and renewable resources is vital for the world’s energy security in the future.

Recently, with the development of renewable energy technology, the ideas about development and environmental sustainability being at odds are becoming outdated. Although solar, wind, hydro energy conversion has been around for centuries, it is only with recent technological advances that such systems can be implemented at a scale where it is useful and viable. As the world continues to embrace a renewable-energy future, the advancement in related technologies is vital.

Among current clean and renewable sources of energy, solar energy is exceptionally appealing because of its low carbon emissions and its inexhaustible source – the Sun. The world has seen the growth of solar energy in the past two decades with silicon solar cells having conversion efficiencies of 25%. [2]  In 2014, worldwide solar energy capacity was sufficient to supply 1% of the world’s total electricity consumption. The growth of global solar energy capacity is yet to continue growing as more countries are expected to install photovoltaic systems.

Silicon solar cells were developed at Bell Labs in the 1950’s. Within the same decade, space satellites were launched with photovoltaic-powered systems onboard. The following decades, silicon solar cells were only deployed for niche applications due to the high cost and complex fabrication. With the development of technologies and the aid of governmental policies, large scale installations in countries like United States, Germany, and Japan became possible in the 90’s. While silicon is efficient and stable, its cost has limited its widespread applications. Due to the high cost of manufacture and the long energy payback time, energy produced by silicon solar cells is more expensive than the grid.

Nevertheless, the price of photovoltaic power is projected to be competitive with traditional sources of electricity within the next ten years. Technology roadmaps for the future outline the research and development path to full competitiveness of concentration solar power with conventional power generation technologies within a decade. The goal of photovoltaics research and development is to make solar power more efficient, more affordable and accessible. The future of photovoltaic energy does not lie merely on silicon solar cells so there intense interest in new materials, cell designs, and novel approaches to solar material and product development.

In an effort to reduce the cost of produced electricity, novel materials and devices are have been intensively investigated as promising approaches to low-cost photovoltaics. Most of the so-called third generation solar technologies which include dye-sensitized solar cells (DSSCs), organic solar cells, and hybrid solar cells can be fabricated using less material and less costly fabrication techniques.

Hybrid solar cells are of particular interest because it combines the advantages associated to both organic and inorganic materials. And compared to conventional solar cells, organic and hybrid solar cells have many advantages, such as light weight, flexibility and potential low cost due to their compatibility with versatile solution processing methods.

Among the choices of inorganic semiconductors for hybrid solar cells, ZnO has gained a lot of attention due to its non-toxicity, good stability, good optoelectronic properties, and low cost. Unlike other common solar cell which contain heavy metals such as cadmium and lead, ZnO is non-toxic and is abundant on the earth’s crust. It has a high electron mobility (up to ~1000

$cm^2 V s^{-1}$), which is favorable for efficient electron transport and reduced recombination loss. It is fabricated through various synthesis methods and possesses diverse morphologies [3].

The following sections will discuss fundamentals of hybrid solar cells, ZnO, and electrochemical deposition.

## 1.1 Hybrid solar cells

Hybrid solar cells fall under the category of third-generation solar technology. The first generation solar cells are based on silicon wafers and the second generation solar cells are based on amorphous silicon, copper indium gallium selenide (CIGS), and cadmium telluride (CdTe). Third generation solar cells are characterized as solution processed devices based on semiconducting organic macromolecules, inorganic nanoparticles, or hybrids [4]. Also under third-generation solar cells are dye sensitized, polymer:fullerene, and perovskite solar cells. Third-generation solar technology is promising for large-scale production due to the lower cost of fabrication and lighter weight of the devices compared to that of previous generations.

Hybrid solar cells composed of organic and inorganic semiconductors combine the advantages associated to both material classes. Organic solar cells (OSCs) are flexible, thin, and can be fabricated by solution processing. Inorganic materials have the advantages of high dielectric constant, high electron mobility and affinity, and tunable optoelectronic properties.

This section gives an overview on hybrid solar cells, its operating principles, and its characterization.

### 1.1.1 Inverted hybrid solar cells

Hybrid solar cells come in various device architectures and are classified mainly depending on the morphology of the inorganic material. In this study, the hybrid solar cells are fabricated in the inverted configuration where electrons are collected at the ITO electrode while holes are collected at the back metal electrode. The ordered ZnO nanorod film is infiltrated with organic bulk heterojunction active layer, as shown in Figure 1.1.

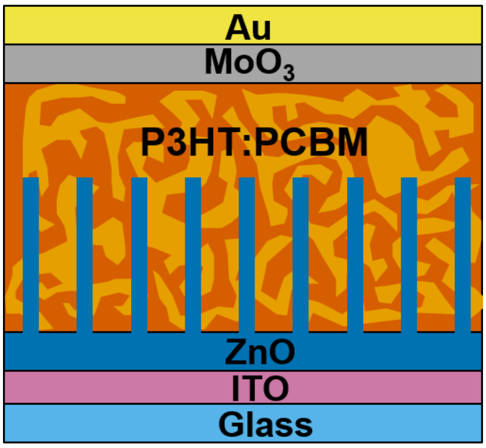

Figure 1.1 Illustration of the cross section of the device

An advantage of ZnO in inverted solar cells is the improved stability compared to the conventional cell devices (holes collected at ITO, electrons at metal electrode). In one study, Jen et al. found that the inverted cells showed only a 20% decrease in efficiency after 40 days under ambient conditions, while the conventional device barely exhibited any photovoltaic activity after 4 days. [5]

The organic bulk heterojunction active layer in this device is a mixture of poly(3-hexylthiophene-2,5-diyl) (P3HT) and phenyl-$C_{61}$-butyric acid methyl ester (PCBM). The P3HT is a donor material while the PCBM is an acceptor material. The electrical conductivity of P3HT results from the delocalization of electrons along the conjugated backbone of the polymer; its side chains aids in its crystallization which helps increase its conductivity. PCBM, a widely used electron acceptor material, is a fullerene derivative with a functional group that enables solubility in the same organic solvents as donor materials.

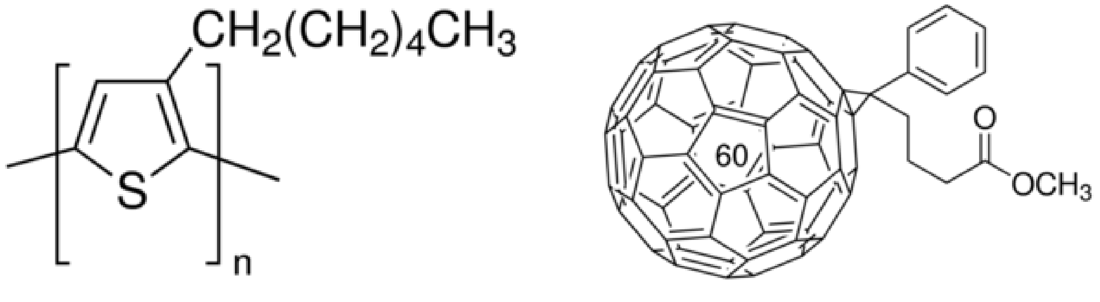

**(a)** **(b)**

Figure 1.2 (a) poly(3-hexylthiophene-2,5-diyl) (P3HT) and (b) phenyl-$C_{61}$-butyric acid methyl ester (PCBM). [6]

### 1.1.2 Mechanism

From solar energy to electricity, four processes are involved in the operation of hybrid solar cells. These processes: exciton generation, exciton diffusion, exciton dissociation, and charge transport to the electrodes are discussed.

1. Exciton generation

   Light absorption in hybrid solar cells is mainly attributed to the conjugated polymers such as P3HT. After absorbing the incident photons, electrons will be excited from the highest occupied molecular orbit (HOMO) to the lowest unoccupied molecular orbit (LUMO). Due to the low dielectric constant of the polymers, the electrons in LUMO and the holes in HOMO are not free charges but excitons with strong Coulomb interaction.

2. Exciton diffusion

The excitons have to diffuse to the donor/acceptor (D/A) interfaces and are separated into free charges. Because that the exciton diffusion length is 4–20 nm for most conjugated polymers [7] [8], the D/A domains in hybrid solar cells should also be in this range for high exciton diffusion efficiency.

3. Exciton dissociation

Upon reaching the D/A interface, excitons could be dissociated into free electrons and holes. The relative positions of the LUMO of the Donors and the CB level of the inorganic acceptors determine the exciton dissociation efficiency.

4. Charge transport to the electrodes

After the exciton dissociation, the free electrons and holes transfer through the inorganic nanocrystals and conjugated polymers until they are collected at the electrodes. The charge transfer efficiency is related to the intrinsic properties of the materials, e.g., the carrier mobility, the crystallinity and the purity, and so on. Continuous pathways are also needed for efficient charge transfer.

### 1.1.3 Characterization of hybrid solar cells

Performance of solar cells is evaluated through current density-voltage characteristics. It is obtained by measuring the current density as the voltage across the device is biased with variable load as the device is irradiated with light. The measurement is performed under AM1.5G, air mass 1.5 global at 100 mW/cm$^2$.

Figure 1.3 shows a typical current density-voltage J-V characteristic for solar cells. The following set of parameters are extracted from the J-V characteristic: open circuit voltage ($V_{OC}$), short circuit current density ($J_{SC}$), fill factor ($FF$), and power conversion efficiency ($PCE$). $J_{max}$ and $V_{max}$ are the current density and voltage at maximum output power.

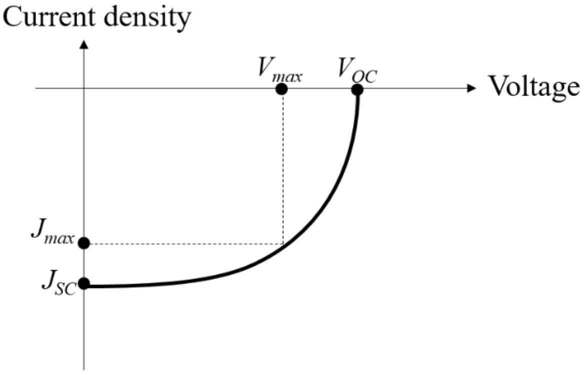

Figure 1.3 Current density-voltage ($J$-$V$) characteristics

1. Short circuit current density ($J_{SC}$)

Short circuit current density is the current density at which the applied external voltage is 0 V. $J_{SC}$ represents the number of charge carriers that are generated and eventually collected at the electrodes at short circuit condition. Enhanced optical/electrical parameters such as, high absorption coefficient, smaller phase separation, and high carrier mobility improve $J_{SC}$.

2. Open circuit voltage ($V_{OC}$)

The open circuit voltage defined as the voltage at which the current density output is 0. $V_{OC}$ has been reported to be mainly dependent on the work function difference of metal contacts.

3. Fill factor ($FF$)

The fill factor defines the shape of the J-V curve. It is defined by the equation below.

$$FF = \frac{J_{max} \times V_{max}}{J_{SC} \times V_{OC}} \quad \text{(Eq. 1.1)}$$

$J_{max}$ and $V_{max}$ are the current density and voltage at the point where the power output is at maximum. FF represents dependence of current output on the internal field of the device and is quantified by the series resistance and shunt resistance.

4. PCE

The power conversion efficiency represents the efficiency of the solar cell and can be calculated as follows from the equation below, where $P_{in}$ is the input power density.

$$PCE = \frac{V_{OC} \times J_{SC} \times FF}{P_{in}} \qquad \text{(Eq. 1.2)}$$

## 1.2 ZnO in hybrid solar cells

Among the choices of inorganic semiconductors for hybrid solar cells, ZnO has gained a lot of attention due to its non-toxicity, good stability, good optoelectronic properties, and low cost. It has a high electron mobility (up to up to ~1000 $cm^2\ V\ s^{-1}$), which is favorable for efficient electron transport and reduced recombination loss. It is fabricated through various synthesis methods and possesses diverse morphologies [3].

ZnO has a wurtzite crystal structure. It has a hexagonal unit cell with lattice parameters $a$ = 0.3249 nm and $c$ = 0.5207 nm. The structure of ZnO has non-central symmetry and polar surfaces. Alternating planes of tetrahedral-coordinated $O^{2-}$ and $Zn^{2+}$ ions stacked along the c-axis produced the charged Zn-(0001) and O-($000\bar{1}$) polar surfaces [3]. The different surface energies, surface polarities, and chemical activities in this crystal structure [9], ZnO growth is anisotropic.

ZnO, therefore, has diverse nanostructures including rosettes, flakes, belts, dots. When nanostructured ZnO was used as a cathode buffer layers in the inverted solar cells, they could show distinctive nano-effects in addition to some beneficial effects for high performance solar cells as provided by intrinsic ZnO films [10]. But the special structure and novel properties of one-dimensional ZnO nanostructures has gained much interest in the field of hybrid solar cells recently. One-dimensional nanostructures, with direct paths for a charge transport and high surface area for light harvesting, are emerging as promising candidates for building solar cells. In addition, confinement of the organic active layer in the cavities of the nanostructures can induce alignment of organic molecules which further enhances the hole mobility [7].

### 1.2.1 Related literature

Two of the first few studies that used ZnO nanorods in hybrid solar cells were by Olson et al. [11] and Takanezawa et al. [12] in 2007. Since then, many hybrid solar cell devices based on ZnO nanorods have been reported. A list of some studies using the same active layer, P3HT:PCBM, is shown in Table 1.

Table 1 Examples of inverted solar cells with nanostructured ZnO

| Device configuration | $V_{OC}$ (V) | $J_{SC}$ (mA/cm$^2$) | *FF* | *PCE* (%) | Ref |
|---|---|---|---|---|---|
| ITO/ZnO NR/ P3HT:PCBM/Ag | 0.57 | 9.6 | 50 | 2.70 | [12] |
| ITO/ZnO NR/ P3HT:PCBM/ $VO_x$/Ag | 0.58 | 10.4 | 65 | 3.90 | [13] |
| ITO/ZnO NR/ P3HT:PCBM/ Ag | 0.53 | 11.7 | 58 | 3.58 | [14] |
| ITO/ZnO NR/ P3HT:PCBM/ $V_2O_5$/Ag | 0.55 | 10.75 | 60 | 3.56 | [15] |
| ITO/ZnO NR/ P3HT:PCBM/ Ag | 0.48 | 14.99 | 34 | 2.44 | [16] |

Olson et al. [11] discussed that the addition of the nanorod arrays as direct charge transport paths from the active layer to the electrode could introduce structuring in the active layer and allow the fabrication of thicker active layers to improve absorption. Takanezawa et al. [12] showed in their study that the role of the ZnO nanostructured array in the device is an electron collector rather than acceptor material.

### 1.2.2 Electrochemical deposition of ZnO

Zinc oxide nanostructured thin films can be fabricated by various methods [17,18]: electron beam lithography [19], vapor-liquid-solid (VLS) growth [20], physical vapor deposition (PVD) [21], chemical vapor deposition (CVD), hydrothermal method [22]. Compared to vapor phase, vacuum, or high temperature routes, electrochemical deposition is an especially appealing technique because it complements the low-cost fabrication processes characteristic of third-generation solar cells. Large area films can be synthesized at low temperature and ambient pressure, thus not requiring a high capital investment. Furthermore, in contrast to top-down synthetic techniques such as lithographic patterning or nanoimprint molding, bottom-up solution growth enable scalable, large area production of 1D nanostructures on various electrode materials. [23] The microstructure and optoelectronic properties can by controlled through adjusting deposition conditions, making electrochemical deposition a suitable technique for designing new solar cells.

In addition, it is a versatile and easy way to grow doped ZnO films [24, 25, 26]. Doped ZnO films grown by electrochemical deposition is explored in Chapters 3 and 4 of this dissertation.

In this study, electrochemical deposition is performed in an aqueous solution containing zinc chloride ($ZnCl_2$). Electrochemical synthesis of ZnO proceeds through a cathodic path; it involves oxidizing the metal ions in solution into an oxidation state where they readily interact with water or hydroxide ions to yield an insoluble deposit. The sequence of reactions to the formation of ZnO can be expressed as follows:

$$\frac{1}{2}O_2 + H_2O + 2e^- \rightarrow 2OH^- \qquad \text{(Eq. 1.3)}$$

$$Zn^{2+} + 2OH^- \rightarrow ZnO + H_2O \qquad \text{(Eq. 1.4)}$$

The deposition of the oxide occurs via the electrogeneration of a base near the working electrode. It produces hydroxide ions via the reduction water or reduction of dissolved oxygen, as in Equation 1.3. The oxygen precursor used in this study is classically molecular oxygen provided by bubbling the electrolyte solution with oxygen gas. The production of hydroxide near the substrate increases the local pH and causes the metal ions to react with hydroxide ions, precipitating out as the desired metal oxide, as in Equation 1.4.

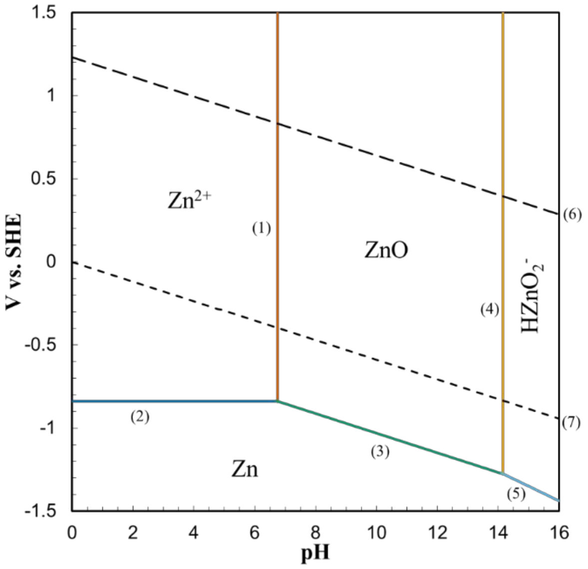

Figure 1.4 Pourbaix diagram for Zn in water (3mM). The lines represent equilibrium between (1) $Zn^{2+}$ and ZnO, (2) $Zn^{2+}$ and Zn, (3) ZnO and Zn, (4) ZnO and $HZnO^-_2$, (5) $HZnO^-_2$ and Zn, (6) $O_2$ and $H_2O$, and (7) $H^+$ and $H_2$.

## 1.3 Objectives and outline

Hybrid solar cells are strong candidates for the emerging photovoltaic market due to the low costs of fabrication and the potential to create lightweight and flexible devices. One of the strategies shown to be effective in improving the performance of hybrid solar cells is the addition of inorganic nanorod structures. For this application, ZnO has gained a lot of interest because its crystal structure and optoelectronic properties are suited for growing nanostructured films with a wide band gap and good carrier mobility.

Electrochemical deposition is a suitable method to grow ZnO nanostructures for hybrid solar cell applications. Because it is low cost, low temperature, and fast, the conditions of electrochemical deposition are compatible with the goal to produce more affordable devices.

For electrodeposited ZnO to be successful in hybrid solar cell applications, methods of controlling the nanostructure and growth mechanism must be understood. Furthermore, methods to tailor the optoelectronic properties and interfaces of the ZnO by electrodeposition should be developed and analyzed. The objectives of this thesis are:

1. Control the growth of electrodeposited ZnO nanorod structures

   Recently, interest in the possibility to fabricated designed structures in nanometer dimensions has increased. In particular, the nanorod array structure is thought of as ideal for hybrid solar cell structures due to the large interfacial area and direct charge transport. However, electrodeposition of ZnO nanorods also come with the growth of micron-sized hexagonal flakes. The objective is to determine the conditions to grow homogeneous ZnO nanorod films by electrochemical deposition in a chloride electrolyte and apply these in hybrid solar cell applications.

2. Develop a method to grow Al-doped ZnO nanostructures

By doping the ZnO with Al the electron mobility can be increased and thus the serial resistance of the material can be decreased. Various methods of growing Al-doped ZnO have been reported, and very few are about the electrodeposition method. The objective is to grow Al-doped ZnO nanostructured films by electrodeposition in a chloride electrolyte apply these in hybrid solar cell applications.

3. Develop a method to grow fullerene-doped ZnO nanostructures

   The interfacial layers in hybrid solar cells, found between the interfaces of the charge separation and charge collection, play a crucial role in determining the efficiency and lifetime of the devices. The objective of the research is to successfully incorporate fullerene on the ZnO nanorod array by electrochemical deposition and use this to fabricate solar cells with improved performance. The resulting films must maintain the nanostructure and have the proper band gap.

Achieving these objectives will aid in the development of low cost hybrid solar cells based on ZnO.

Chapter 1 provides an introduction to the study and discusses the objectives. A brief overview of important concepts in hybrid solar cells and electrochemical deposition is provided.

Chapter 2 discusses the growth of ZnO by electrochemical deposition from a chloride electrolyte. Here, methods to control the ZnO film nanostructure are discussed. First, the effect of the substrate on the nanostructure is investigated. In particular, bare ITO and ZnO seed layer are compared. Second, the effect of the supporting electrolyte concentration on the nanostructure is investigated. A ZnO nanostructured film as a cathode buffer layer is demonstrated.

Chapter 3 discusses the growth of aluminum-doped ZnO films by electrochemical deposition from a chloride electrolyte. Aluminum chloride hexahydrate is added to the electrolyte as the dopant source. The chapter also discusses attempts to inhibit the growth of hexagonal flakes.

Chapter 4 discusses the growth of fullerene-doped ZnO films by electrochemical deposition from a chloride electrolyte. A water-soluble fullerene derivative, $C_{60}$ pyrrolidine tris-acid (CPTA), is added to the electrolyte as the dopant source. ZnO films with nanorod arrays structures were successfully grown without the flakes.

Chapter 5 gives a summary of the research. In addition, the chapter provides outlook for future studies.

# References

[1] J. Gillis, "Short answers to hard questions about climate change," 28 11 2015. [Online]. Available: http://www.nytimes.com/interactive/2015/11/28/science/what-is-climate-change.html?_r=0. [Accessed 1 12 2015].

[2] J. Zhao, A. Wang and M. A. Green, *Progress in Photovoltaics: Research and Applications,* vol. 7, p. 471, 1999.

[3] L. Li, T. Zhai, Y. Bando and D. Goldberg, *Nano Energy,* vol. 1, p. 91, 2012.

[4] J. Yan and B. R. Saunders, *RSC Adv.,* vol. 4, p. 43286, 2014.

[5] S. K. Hau, H. -L. Yip, H. Ma and A. K. -Y. Jen, *Appl. Phys. Lett.,* vol. 93, p. 233304, 2008.

[6] "Sigma aldrich," [Online]. Available: http://www.sigmaaldrich.com/catalog/product/aldrich/684430?lang=ja&region=JP. [Accessed 31 December 2015].

[7] J. Weickert, R. B. Dunbar, H. C. Hesse, W. Wiedemann and L. Schmidt-Mende, *Adv. Mater.,* vol. 23, p. 1810, 2011.

[8] T. Xu and Q. Qiao, *Energy Environ. Sci.,* vol. 4, p. 2700, 2011.

[9] T. Zhai, X. Fang, L. Li, Y. Bando and D. Goldberg, *Nanoscale,* vol. 2, p. 168, 2010.

[10] J. Huang, Z. Yin and Q. Zhen, *Energy. Environ. Sci.*, vol. 4, p. 3861, 2011.

[11] D. C. Olson, J. Piris, R. T. Collins, S. E. Shaheen and D. S. Ginley, *Thin Solid Films,* vol. 496, p. 26, 2006.

[12] K. Takanezawa, K. Hirota, Q. S. Wei, K. Tajima and K. Hashimoto, *J. Phys. Chem. C,* vol. 111, p. 7218, 2007.

[13] K. Takanezawa, K. Tajima and K. Hashimoto, *Appl. Phys. Lett.*, vol. 93, p. 063308, 2008.

[14] C. Y. Chou, J. S. Huang, C. H. Wu, C. Y. Lee and C. F. Lin, *Solar Energ. Mater. and Solar Cells,* vol. 93, p. 1608, 2009.

[15] J. S. Huang, C. Y. Chou, M. Y. Liu, K. H. Tsai, W. H. Lin and C. F. Lin, *Org. Electron.,* vol. 10, p. 1060, 2009.

[16] Y. Hames, Z. Alpaslan, A. Kosemen, S. E. San and Y. Yerli, *Sol. Energy,* vol. 84, p. 426, 2010.

[17] A. B. Djurišić, X. Chen, Y. H. Leung and A. M. C. Ng, *J. Mater. Chem.,* vol. 22, p. 6526, 2012.

[18] J. L. Gomez and O. Tigli, *J. Mater. Sci.*, vol. 48, p. 612, 2013.

[19] S. Xu, Y. Ding, G. Wei, H. Fang, Y. Shen, A. K. Sood, D. L. Polla and Z. L. Wang , *J. Am. Chem. Soc.*, vol. 131, p. 6670, 2009.

[20] T. Hsueh, C. Hsu, Y. Lin, T. Lin and I. Chen, *J. Electrochem. Soc.*, vol. 154, p. H153, 2007.

[21] Y. Zhang, H. Jia, R. Wang, C. Chen, X. Luo and D. Yu, *Appl. Phys. Lett.*, vol. 83, p. 4631, 2003.

[22] L. E. Greene, M. Law, D. H. Tan, M. Montano, J. Goldberger, G. Somorjai and P. Yang, *Nano Lett.*, vol. 5, p. 1231, 2005.

[23] J. Jean, S. Chang, P. R. Brown, J. J. Cheng, P. H. Reckemeyer, M. G. Bawendi, S. Gradecak and V. Bulovic, *Adv. Mater.*, vol. 25, p. 2790, 2013.

[24] O. Lupan, T. Pauporté, V. B., P. Aschehoug, M. Ahmadi, B. Roldan Cuenya, Y. Rudzevich, Y. Lin and L. Chow, *Appl. Surf. Sci.*, vol. 282, p. 782, 2013.

[25] J. Chen, J. Chen, D. Chen, Y. Zhou, W. Li, Y. Ren and L. Hu, *Mater. Lett.*, vol. 117, p. 162, 2014.

[26] M. A. Thomas and J. B. Cui, *J. Appl. Phys.*, vol. 105, p. 093533, 2009.

[27] W. Beek, M. Wienk and R. Janssen, *J. Mater. Chem.*, vol. 15, p. 2985, 2005.

[28] M. A. Thomas, W. W. Sun and J. B. Cui, *J. Phys. Chem. C*, vol. 116, p. 6383, 2012.

[29] A. Goux, T. Pauporté, J. Chivot and D. Lincot, *Electrochim. Acta*, vol. 50, p. 2239, 2005.

[30] J. Cembrero and D. Busquets-Mataix, *Thin Solid Films*, vol. 517, p. 2859, 2009.

[31] J. Jean, S. Chang, P. R. Brown, J. J. Cheng, P. H. Reckemeyer, M. G. Bawendi, S. Gradečak and V. Bulović, *Adv. Mater.*, vol. 25, p. 2790, 2013.

[32] D. Olson, J. Piris, R. Collins, S. Shaheen and D. Ginley, *Thin Solid Films,* vol. 496, p. 26, 2006.

# 2 Electrochemical deposition of nanostructured ZnO

## 2.1 Introduction

Zinc oxide (ZnO) is an oxide semiconductor with a wide and direct bandgap at 3.37 eV, good semiconductor properties, and high carrier mobility [1]. Because of this, it is a popular choice for hybrid organic/inorganic solar cells [2]. ZnO can be grown by various techniques into an array of structures such as nanoparticles [3], nanorods [4], nanotubes [5], flakes [6], and porous films [7].

For hybrid solar cells, an ideal structure for optimal charge collection is that of an ordered bulk heterojunction where an inorganic film grown into an array of vertically aligned, crystalline nanorods is encased by a polymer active layer. The nanorod array provides a very large interfacial area compared to a planar heterojunction. Furthermore, the individual crystalline nanorods act as direct charge transport paths. With the ordered bulk heterojunction structure, thicker solar cells with improved absorption can be fabricated without sacrificing the quality of charge transport. Various groups have reported on the use of ZnO nanorod arrays for hybrid solar cells using different ZnO synthesis techniques and organic components. This study is particularly related to the studies by Olson et al. [8] and Takanezawa et al. [9] who demonstrated hybrid solar cells using ZnO nanorod array with poly(3-hexylthiophene) (P3HT) and phenyl-$C_{61}$-butyric-acid-methyl ester (PCBM).

## 2.2 Experimental

### 2.2.1 ITO substrate preparation

The as-purchased substrates were 20 mm x 20 mm glass substrates fully-covered with a 150 nm layer of ITO on one side. The substrates are first patterned and then cleaned before the seed layer is deposited.

Because an area without ITO is necessary in the fabrication of hybrid solar cells, a strip of ITO (3mm x 20 mm) must be etched away from the as-purchased ITO substrates, as seen in Figure 2.1. A plastic tape used to pattern the substrates, protects the area it covers from being etched away.

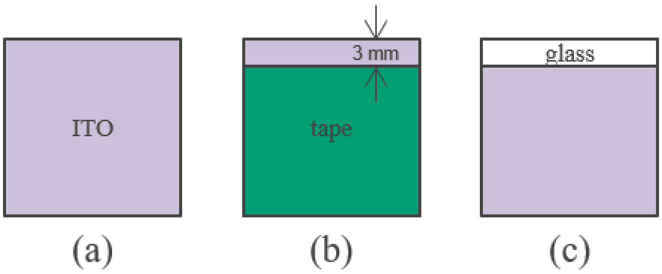

Figure 2.1 As-purchased ITO substrates (a) are patterned with tape (b) to prepare for etching. A rectangular area is etched away from the patterned substrates (c).

To etch the ITO, a paste of zinc dust and 2-propanol is applied to the exposed area. After a few minutes, the solvent dries off and leaves a thick and compact layer of zinc dust. Concentrated hydrochloric acid (HCl) carefully dropped onto the layer of zinc dust etches away the exposed ITO. The reaction of Zn and HCl produces $ZnCl_2$ and $H_2$. The hydrogen gas reduces the ITO to its metallic state, which upon reacting with HCl produces more hydrogen gas and soluble $SnCl_4$.

The plastic tapes are peeled off from the substrates. After which, the substrates are pre-rinsed in water to remove excess Zn powder and salts before starting the cleaning process. With an ultrasonicator, the substrates undergo ultrasonication three times each in distilled water, acetone, and ethanol for 10-minute periods. A metal basket with a holder for each substrate is used. The basket is submerged in a glass container with enough liquid to submerge the substrates. After cleaning, the substrates are kept in ethanol solution.

Before using, the substrates are dried in a vacuum oven for at least 15 min to dry off the excess solution. They then undergo the final process of cleaning – UV-ozone treatment.

### 2.2.2 ZnO seed layer deposition

A seed layer made up of ZnO nanocrystals forming a continuous film is deposited over the ITO substrates via a sol-gel process. Here, a methanolic precursor is first spin-coated over the ITO substrates. Then, the substrates are placed in an oven where the coated film is dehydrated into ZnO.

The precursor is prepared by dissolving zinc acetate dihydrate ($Zn\ (CH_3COO)_2{\cdot}2H_2O$) in methanol in a 0.1 g/mL concentration. It is observed that a clear solution is obtained when the ZAD is added to the methanol in two or three parts. Also, it is recommended to use high-grade methanol such as spectroscopic methanol. The solution can be placed in an ultrasonicator to aid the dissolving process.

For the purpose of fabricating hybrid solar cells, it is necessary to have a bare ITO surface, i.e. not covered by ZnO. For that reason, the cleaned ITO substrates are patterned with plastic tape so to leave a portion of the substrates uncoated with ZnO. Plastic tapes are placed such that it covers an area 3 mm x 20 mm on the edge of the substrates.

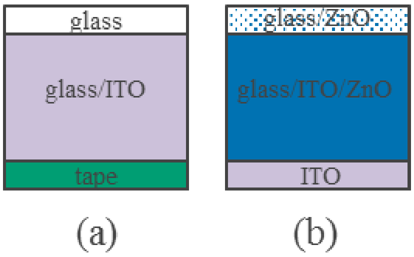

Figure 2.2 Patterning for ZnO seed layer deposition.

Using a pipette, 200 μL of the precursor is dropped on the substrate. This volume is enough to cover the entire substrate surface. The precursor is spin-coated on the substrates at a speed of 4000 rpm for 60 s. The plastic tapes are peeled off and the substrates are then placed in an oven under atmosphere at 350 °C for 30 min. The substrates cool down in the oven as it is turned off. These conditions result in a continuous film of ZnO about 30 nm in thickness made up of nanocrystals about 30 nm in diameter.

The ZnO seed layer film thickness can be modified by changing the precursor concentration, spin-coating speed, and number of spin-coating instances. The precursor concentration can be increased up to saturation, which this study has observed to be 0.2 mg/mL. A higher concentration will result in a thicker film thickness whereas a lower concentration will result in a thinner film. This study did not explore precursors with concentrations less than 0.1 mg/mL. Decreasing the spin-coating speed will result in a thicker film whereas increasing the film thickness will result in a thinner film. Multiple spin-coating instances can also be a way to increase the thickness of the film.

### 2.2.3 ZnO electrochemical deposition

Electrochemical deposition of ZnO films are carried out with a rotating disk electrode set-up in chloride electrolyte baths. The rotation stirs the electrolyte and makes the solution flow up to the electrode and move across away from the center. As a result, the steady state current is controlled by the solution flow rather than diffusion through the boundary layer. The set-up is connected to a potentiostat (Hokuto Denko HSV-110) that supplies the applied potential.

There are three electrodes in the system: working electrode, reference electrode, and counter electrode. The working electrode is the rotating disk to which the ITO substrates are mounted to with conducting tape. The substrates are masked with plastic tape such that ZnO is deposited in the shape of a circle with a diameter of 14 mm. The reference electrode used in this study is a saturated calomel electrode (SCE). The counter electrode is a coiled zinc wire.

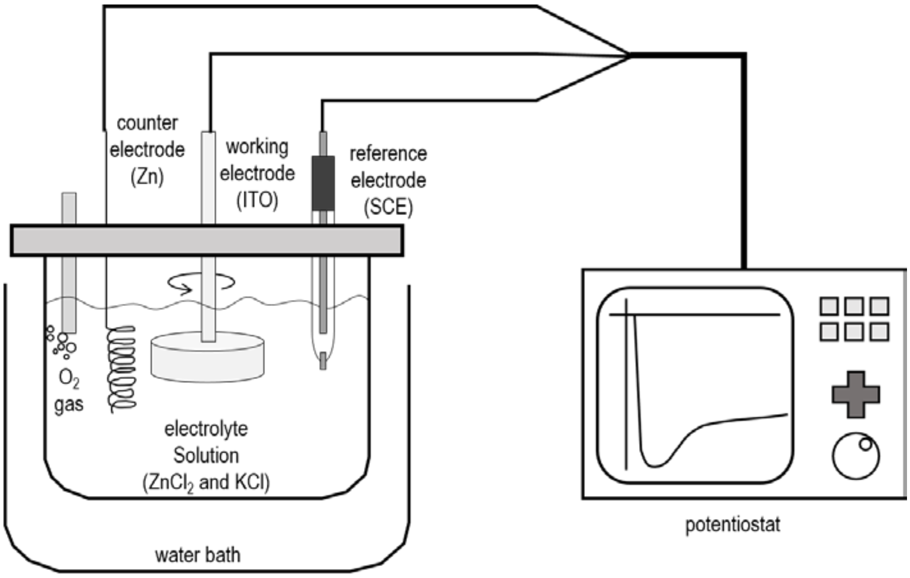

Figure 2.3 Schematic diagram for the electrochemical deposition set-up

The electrolyte is a solution of 0.1 M KCl and 3 mM $ZnCl_2$ in water. The total volume of the electrolyte for the setup is 310 mL. The electrolyte was heated to 70 $^{o}$C prior to deposition and kept at the same temperature during deposition with a water bath. It was saturated with oxygen by bubbling oxygen gas through a glass frit at least 20 min prior to deposition and during deposition.

When the electrolyte reaches the set temperature and is saturated with oxygen, the electrodes are lowered into the electrolyte to begin the deposition. Upon lowering the electrodes, the rotating disk starts to rotate. Deposition begins when the potentiostat supplies a constant voltage of -1.0V vs. SCE and continues until a set deposition time.

The samples are immediately removed and rinsed with water to remove excess salts. They are then placed inside a vacuum oven to dry.

### 2.2.4 Hybrid solar cell fabrication and characterization

Using the ZnO samples described in the previous subsection, inverted hybrid solar cells with ordered bulk heterojunction structure are fabricated in this study. First, the organic active layer of P3HT and PCBM is deposited by spin-coating. Then, after the active layer has dried, the subsequent layers – $MoO_3$ and Au are deposited by thermal evaporation. The figure below is a diagram of the cross-section of the finished device.

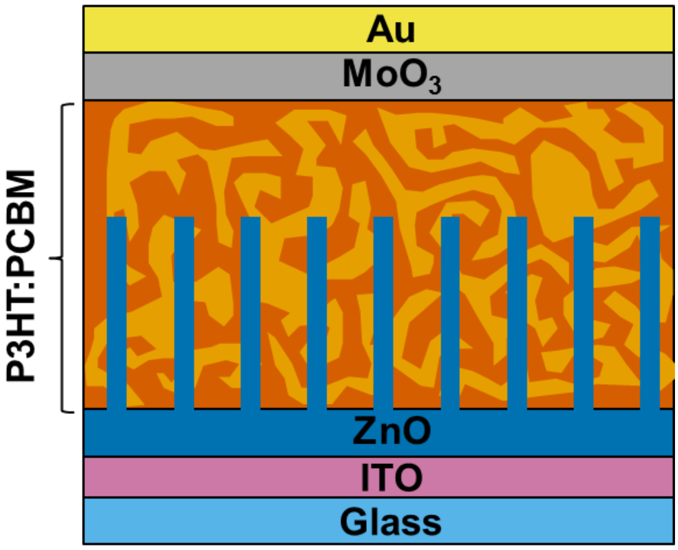

Figure 2.4 Schematic diagram of inverted nanorod array bulk heterojunction hybrid solar cell.

The active layer solution is prepared by dissolving the P3HT and PCBM in chlorobenzene or a mixture of chlorobenzene and trichlorobenzene. The solution is placed in a small bottle and is mixed by a magnetic stirrer for a few hours. Mixing is aided by placing the bottle on a hot plate set at 85 $^{o}$C.

Deposition by spin-coating is performed inside a nitrogen-filled glove box. Using a pipette, 250 μL of the solution is dropped on the ZnO-covered ITO substrates. Spin-coating is performed at 600 rpm for 60 s.

After the active layer has dried, $MoO_3$ and Au are subsequently deposited by vacuum deposition. The samples are placed in a holder with a metal shadow mask. The pattern of the shadow mask creates three 3 mm x 3 mm devices for each substrate.

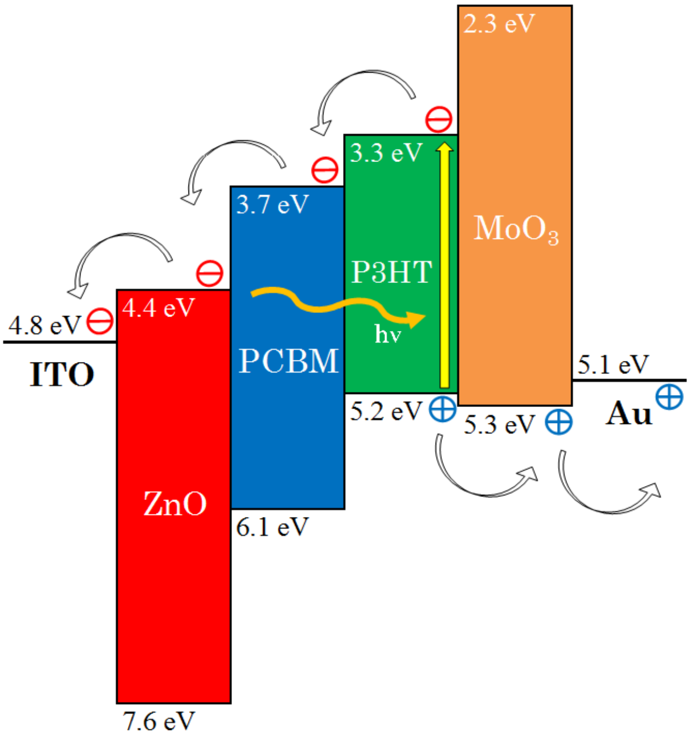

Figure 2.5 Energy diagram of the device

Molybdenum oxide is deposited until the quartz crystal monitor registers a 30 Hz decrease in the frequency. In this condition, the thickness of the $MoO_3$ film is about 10 nm. Gold is deposited until a film about 60 nm is deposited.

Figure 2.5 shows the energy diagram of the device. Photons absorbed in the P3HT:PCBM layer leads to the generation of excitons. The exciton then diffuse to P3HT:PCBM (donor-acceptor) interface where they undergo exciton dissociation to form geminate pairs. Electrons and holes are then transported for extraction at the electrodes. Because the work function of ITO (4.8 eV) lies between the typical HOMOs and LUMOs of P3HT and PCBM, it is capable of collecting either holes or electrons. The ZnO layer acts as a cathode buffer layer for efficient electron extraction by virtue of its energy level which prevents hole extraction at the ITO electrode. Similarly, $MoO_3$ is an anode buffer layer that prevents electron extraction at the Au electrode.

## 2.3 Effect of the ZnO seed layer

The study aims to grow nanostructured ZnO films on ITO substrates for hybrid solar cell applications. A nanorod array structure is ideal for this application. Not only does it provide a larger interfacial area compared to a planar heterojunction, the individual crystalline nanorods also act as direct charge transport paths.

However, the growth of highly ordered nanorod arrays on ITO is not straightforward. Similar studies have relied on pre-treatment of the ITO with HCl [10, 11] or galvanostatic electrodeposition of a buffer layer prior to the actual deposition of ZnO [5]. For this study, we deposited ZnO seed layers on the ITO substrates via a sol-gel method prior to electrochemical deposition. ZnO seed layers have been reported to assist in the growth of highly oriented nanorod arrays. [12]

The seed layer deposition process is adapted from the method employed in a previous study [12]. In their experiment, the seed layer is deposited by spin-coating a saturated solution of methanol and zinc acetate dihydrate. The film is then baked in an oven at 350 $^{o}$C for 30 min. The process of spin-coating and baking is repeated until the desired thickness is achieved. In this study, only a single layer of ZnO nanocrystals are deposited. Another modification to the method is in the preparation of the precursor. In this study, the precursor is prepared by mixing zinc acetate dihydrate and methanol in a fixed concentration of 0.1 g/mL instead of using a saturated solution. A similar non-saturated solution was used in a previous study [13]. By doing so, it makes sure that there are no undissolved zinc acetate dihydrate crystals in the solution. The solution also yields a thinner ZnO seed layer film.

This particular sol-gel method of depositing a film of ZnO nanocrystals is one among many. But compared to other methods, it is simpler because it uses the least components (only methanol and zinc acetate dihydrate) and preparing the precursor solution only requires mixing the two components at room temperature for a few minutes just until dissolved. More popular sol-gel methods use a precursor that contains 2-methoxyethanol and methanolamine in addition of zinc acetate dihydrate. The solution is prepared by mixing for 30 min at 60 $^{o}$C [14]. Some precursors are aged for some time before using. This aging process usually for 24 h [15] up to a few days [16, 17].

This section discusses the effect of the additional ZnO seed layer to the growth of the nanostructured ZnO film.

### 2.3.1 Nanostructure

ZnO nanostructured films were grown on bare ITO and on seeded ITO substrates. The specific conditions for electrochemical deposition of these set of samples are described.

Electrochemical deposition of ZnO on bare ITO substrates and ZnO-seeded ITO substrates were carried out on an RDE setup with a Zn wire counter electrode and saturated calomel electrode (SCE) reference. Deposition was performed for 600 s at RDE rotation speeds of 300 and 500 rpm and at a fixed potential of −1.0 V versus SCE. The electrolyte solution contained 0.1 M KCl and 5 mM $ZnCl_2$ and was kept at 70 °C during deposition. The solution was bubbled with $O_2$ through a glass frit prior to and during the deposition process.

The different morphologies between the ZnO films electrodeposited on bare ITO and seeded ITO substrates are seen in the figure below. These are top view SEM images of the samples. The nanostructure of the ZnO deposited on the bare ITO substrates are made up of tapered rods with diameters varying from 400 to 900 nm. On the other hand, the nanostructure of the ZnO deposited on seeded ITO substrates are arrays of densely packed nanorods about 100 nm in diameter.

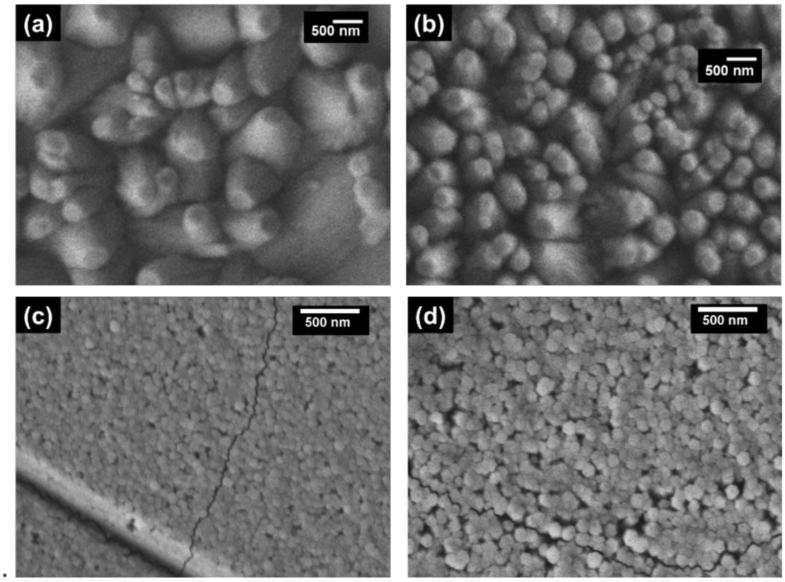

Figure 2.6 SEM images of the electrochemically deposited ZnO on bare ITO substrates (a) 300 rpm and (b) 500 rpm, and on seeded ITO substrates at (c) 300 rpm and (d) 500 rpm.

The thickness of the films are also different, as seen in the figure below. The ZnO film deposited on the bare ITO substrate is thicker at about 750 nm compared to the thickness of the film deposited on the seeded ITO substrate at about 400 nm. Because these cross-section SEM images were taken after the samples have been fabricated into solar cells, the organic active layer can be seen coating the ZnO nanostructures. The seed layer, although comparably thin, can be seen Figure 2.6 (b) between the electrodeposited ZnO and ITO.

These figures show the improvement on the morphology of the nanorod array with the addition of the ZnO seed layer. The nanorods deposited on the seeded ITO substrates have a higher degree of vertical orientation, perpendicular to the substrate.

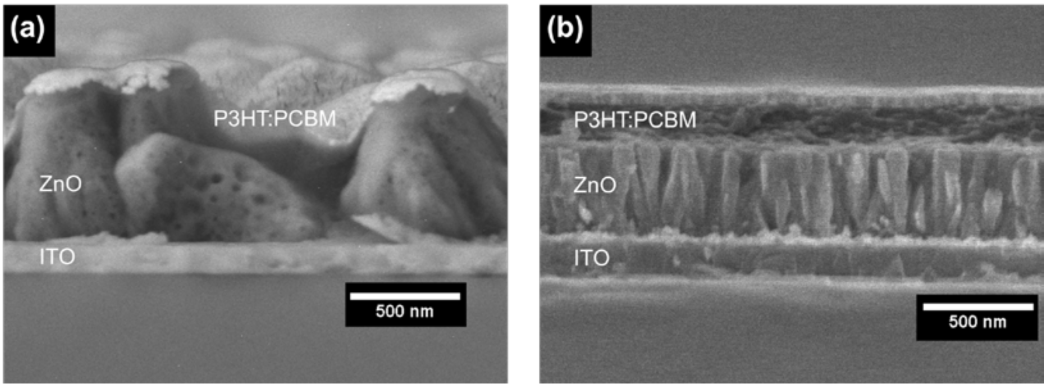

Figure 2.7 SEM images of the cross-sections of electrochemically deposited ZnO on (a) bare ITO substrate and on (b) seeded ITO substrate.

The X-ray diffraction patterns shown in the figure below show the strong intensity of the diffraction peak at 34.3°. It corresponds to the ZnO (0002) spacing which indicates that the nanorods grew preferentially along the [0001] direction for both ZnO films grown on bare ITO substrates and on seeded ITO substrates.

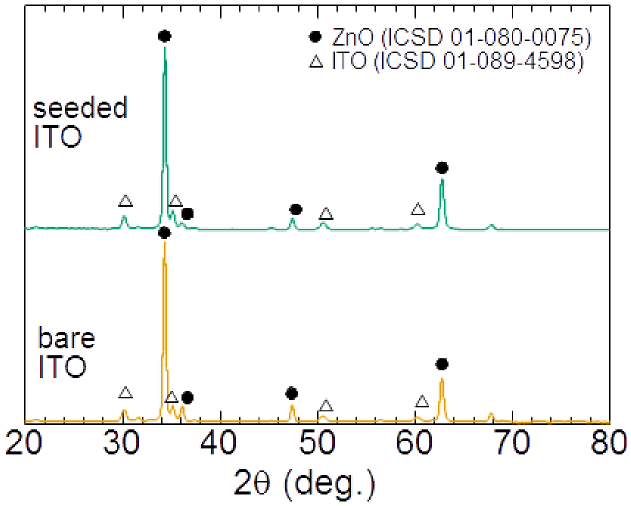

Figure 2.8 X-ray diffraction patterns of the ZnO electrochemically deposited on bare ITO and seeded ITO substrates.

### 2.3.2 Growth

To further understand the difference in morphologies, the growth of ZnO films during deposition is analyzed from chronoamperometric transient curves, shown in the figure below. These curves plot the current density, as measured by the potentiostat, against the deposition time. Note that the current density axis goes from 0 to -1 mA/cm$^2$. The shape of these curves are typical for ZnO electrochemical deposition. [18] The electrochemical deposition process can be divided into two stages: the nuclei growth stage and the nanostructure growth stage. [11] These two stages can be distinguished from the chronoamperometric curves.

First, the nuclei growth stage is observed when the deposition begins. As the negative potential (-1.0 V) is applied to the system, the cathode current immediately increases because of the increase in the active surface area of the nuclei as they undergo three-dimensional growth. These nuclei continue to grow until eventually the edges of the individual nuclei meet. A current maximum is reached upon the coalescence of nuclei [19].

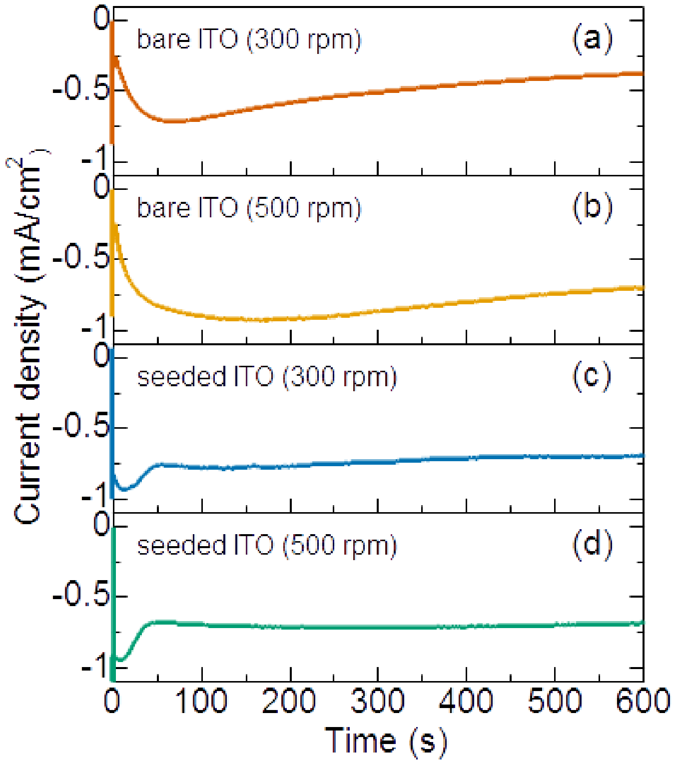

Figure 2.9 Chronoamperometric transient curves of ZnO electrochemically deposited on bare ITO at (a) 300 rpm and at (b) 500 rpm, and on seeded ITO substrates at (c) 300 rpm and at (d) 500 rpm.

The nanostructure growth stage begins right after the coalescence of the nuclei. The three-dimensional growth of the nuclei stops and one dimensional growth, along the c-axis, commences. In this stage, the current decays and reaches a steady state value.

The chronoamperometric curves in Figure 2.9 (c) and (d) show that the nucleation and coalescence (maximum current density) process occurs much more quickly for the seeded ITO substrates. Coalescence is reached at 8 s (300 rpm) and 13 s (500 rpm) on the seeded ITO substrates.

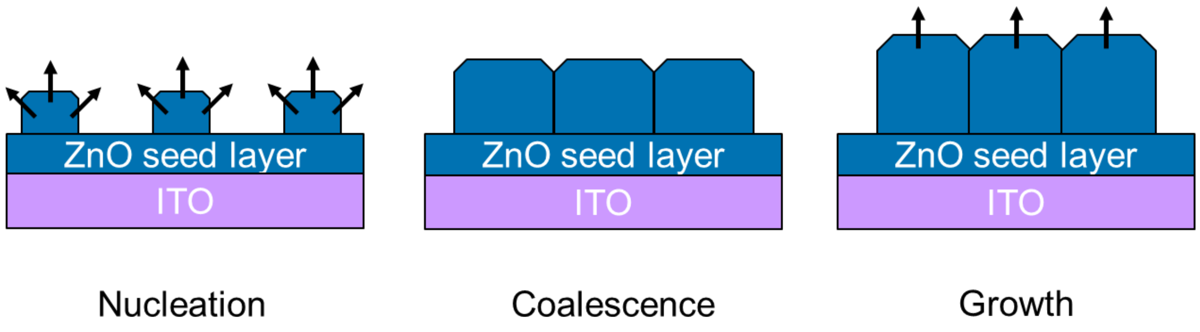

Figure 2.10 Diagram of nanorod growth process: nucleation, coalescence, and growth.

After the early sharp dip in the curve, the current density then decreases and assumes a steady value until the end of the deposition process. The quick nucleation and coalescence indicate a high density of starting nuclei. The shorter time it takes to reach the nuclei coalescence stage suggests that the nuclei did not grow very large before the nanostructure growth stage. The smaller the nuclei are at coalescence, the smaller the diameter of the nanorods grown. Furthermore, the diameters are more likely to be the same size if the nuclei are evenly spaced and grew the same amount before coalescence. The high density of the starting nuclei, all growing preferentially along the c-axis, would result in a nanorod array with a high degree of orientation.

In the case of ZnO deposited on bare ITO, the chronoamperometric curves in Figure 2.9 (a) and (b) show that coalescence is achieved at a later time after the start of deposition, 74 s (300 rpm) and 161 s (500 rpm). The curves show the current densities increase in a more gradual manner. It has a milder slope upon the start of deposition compared to the sharp dip of the curves for the ZnO deposited on ZnO-seeded ITO. The longer time it took to reach the coalescence stage indicates a low density of starting nuclei. As a result of the nuclei being farther away from one another, the nuclei need to grow larger to reach the coalescence stage.

This explains the growth of larger nanostructures on bare ITO substrates, as seen in Figure 2.7 (a).

In addition, Figure 2.9 (a) and (b) shows that after nucleation and coalescence, in the growth stage, the current densities do not assume a steady value. Instead, the current density gradually decreases as the deposition proceeds. This slope in the curves suggest that nucleation may not have happened simultaneously, such that new, smaller nuclei continue to form on the bare ITO even as the initial nuclei have already started growing. This explains the different diameters of the nanorods grown on the bare ITO substrates.

The higher density of the nuclei on the seeded ITO substrates can be attributed to the ZnO seed layer. The morphology of this film is shown in Figure 2.11. It is composed of ZnO nanoparticles, about 20 to 30 nm in diameter, closely packed, and forming a continuous film. This ZnO seed layer has been found to have a preferential orientation to the substrate. A previous study has shown that the decomposition of zinc acetate at 350 $^{o}$C forms a layer of ZnO nanocrystals with their c-axes oriented perpendicular to the substrate [20].

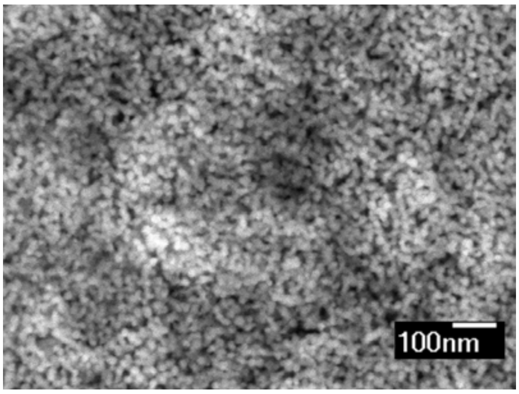

Figure 2.11 SEM image of the ZnO seed layer

Figure 2.12 shows the XRD spectra of a bare ITO substrate and of a ZnO-seeded ITO substrate. The intensity of the ITO peaks are very large compared to the ZnO peaks because of the larger thickness of the ITO film (~150 nm) compared to the ZnO seed layer (~30nm). Still, the peaks corresponding to ZnO can be distinguished. Among the ZnO peaks, the peak corresponding to the ZnO (0002) plane has the highest intensity. It suggests preferential orientation of the crystals along the c-axis. The XRD spectra of the ZnO seed layer agrees with the results of the previous study which shows the preferential c-axis orientation of the nanocrystals formed from the decomposition of zinc acetate.

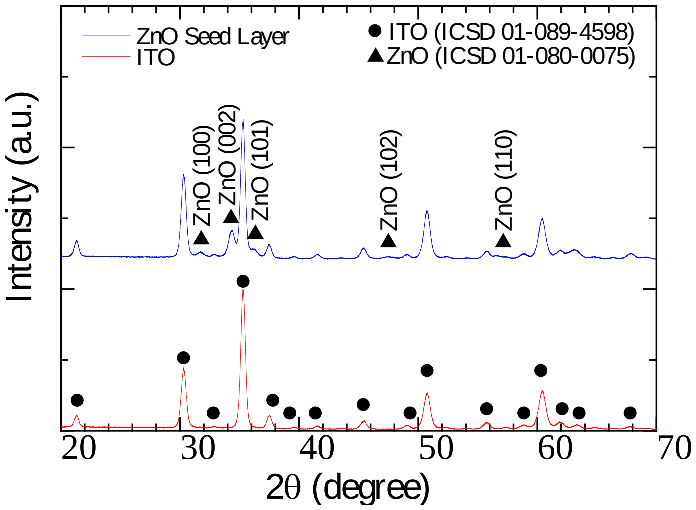

Figure 2.12 XRD spectra of a bare ITO substrate and ZnO-seeded ITO substrate

During electrodeposition, the densely packed film of ZnO nanocrystals act as homoepitaxial nucleation sites [21]. This results in the formation of nuclei in a high density across the ZnO seed layer surface. Conversely, bare ITO has a high nucleation potential barrier which results to a lower density of nucleation sites. As shown by the results, the seed layer improves the density, morphology, and vertical alignment of the ZnO nanorods grown by electrochemical deposition.

### 2.3.3 Optical Properties

Aside from the difference in the nanostructures, the ZnO films deposited on bare ITO substrates and on seeded ITO substrates also differed in their optical transmittance. It is imperative for the ZnO film to have a high optical transmittance particularly in the inverted hybrid solar cell structure.

The UV-Vis transmittance spectra of the deposited ZnO films are show in the figure below. The optical transmittance of the ZnO film deposited on the seeded ITO substrate is clearly larger compared to the ZnO film deposited on the bare ITO substrate. Although many factors such as morphology [22], filling ratio [23], and roughness [24] affect the transmittance, the higher optical transmittance of the film deposited on the seeded ITO substrates can be mainly attributed to the better vertical alignment of the nanorods and to the nanorod diameters that are homogeneous and shorter than the wavelengths of light in the visible region.

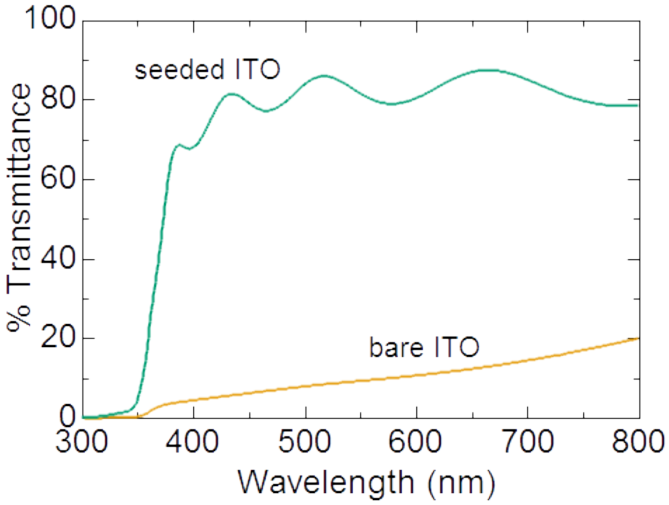

Figure 2.13 UV-vis transmittance spectra of the ZnO electrochemically deposited on bare ITO and on seeded ITO substrates at 500 rpm.

The low transmittance of the ZnO grown on the bare ITO substrates can be mainly attributed to light scattering caused by nanostructures with sizes similar to and exceeding the wavelengths of light in the visible region. Apart from the tapered nanostructures, ZnO also grew into micron-sized hexagonal flakes. These structures also contributed to the lower optical transmittance of the ZnO film. ZnO hexagonal flakes grown by electrochemical deposition have also been observed by other researchers. [6, 25]

The photoluminescence (PL) spectra of the films are analyzed to evaluate the quality of the ZnO films in terms of its defects. The visible luminescence from ZnO can be assigned to intrinsic and extrinsic defects. [26] The photoluminescence spectra of the samples are shown in the figure below. The spectra exhibit a broad PL band around 565 nm which may be due to zinc vacancies [27]. Another study also attributes other energies related to zinc vacancies [28]. A peak around 520 nm, attributed to oxygen vacancies [29], can be distinguished from the PL spectra of the ZnO film deposited on the seeded ITO substrates (500 rpm). These yellow and green PL bands are similar to the PL spectra of the ZnO nanorods in previous studies [30, 31].

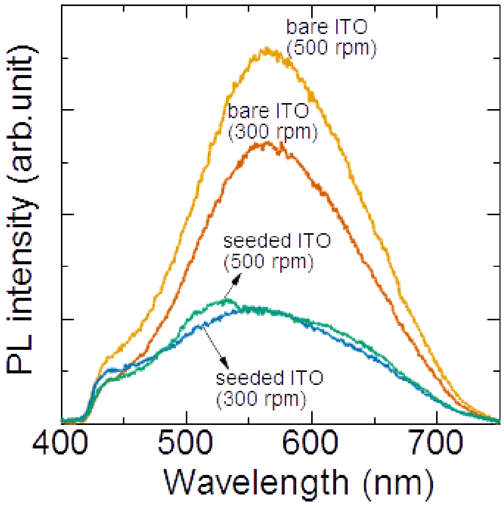

Figure 2.14 Photoluminescence spectra of the ZnO electrochemically deposited on bare ITO and on seeded ITO substrates at 300 rpm and 500 rpm.

Even though the defects are similar in all samples, there is a difference in the PL intensity depending on the substrate. The ZnO films deposited on the bare ITO substrates display a larger PL intensity compared to that of the ZnO films deposited on the seeded ITO substrates. It indicates that there is a larger concentration of defects on the ZnO grown on the bare ITO substrates. That is, during electrochemical deposition, fewer defects are incorporated into the ZnO grown on the seeded ITO substrates. It has been suggested that the $Cl^-$ ions from the supporting electrolyte, KCl, may be incorporated into the ZnO crystals during deposition as a result of poor nucleation on bare ITO and may contribute to the strong defect emission [11].

### 2.3.4 Hybrid solar cell characteristics

Hybrid solar cells were fabricated from the electrochemically deposited ZnO films following the inverted bulk heterojunction structure. The ZnO nanorod array serves as the ordered inorganic component and the active layer of P3HT and PCBM as the organic component of the hybrid solar cell. The specific conditions for fabrication of the devices are described. The active layer was deposited by spin-coating (700 rpm for 60 s) a 30 mg/mL solution of P3HT and PCBM at a 1:1 ratio in a mixture of chlorobenzene and trichlorobenzene at a 1:1 ratio. The samples were allowed to dry in individual sample cases placed in nitrogen atmosphere for about 2 h. A thin coating (~10 nm) of molybdenum oxide (MoO3) was deposited as an electron-blocking layer. Finally, a film of Au was deposited by vapor deposition through a shadow mask as a top electrode.

The figure below shows the *J-V* characteristics of the hybrid solar cells fabricated from the electrochemically deposited ZnO films. The overall performance of the seeded ITO solar cells is better compared to the bare ITO samples. The power conversion efficiencies (*PCE*) of the bare ITO samples are 0.003 and 0.006% for 300 and 500 rpm, respectively. For the seeded ITO samples, the *PCE* were 0.18 and 0.50% for 300 and 500 rpm, respectively.

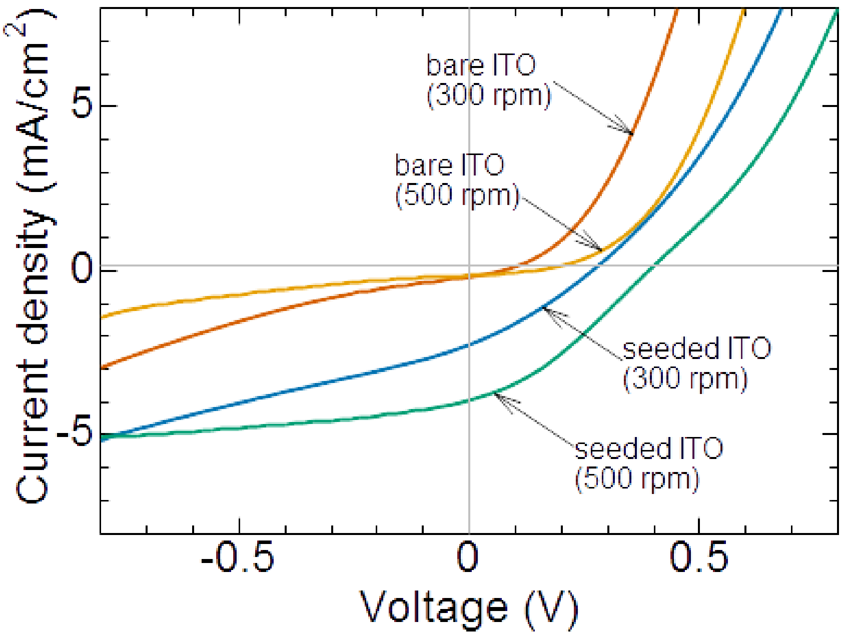

Figure 2.15 JV-characteristics of the hybrid solar cells fabricated from the electrochemically deposited ZnO.

Aside from the poor optical transmittance, the low performance from the bare ITO samples can also originate from short circuited paths formed when the ITO is in direct contact with the active layer. This translates to a device having low shunt resistance. The photovoltage from the solar cell is consequently reduced, as shown by the *J-V* curves for the devices fabricated on the bare ITO. These short circuited paths are formed because the ITO is not completely covered by the electrodeposited ZnO due to the low density of nuclei, allowing the active layer to contact the ITO. For the seeded ITO samples, the seed layer not only aids in nucleation, it also acts as a hole-blocking layer by preventing direct contact between the active layer and the ITO.

## 2.4 Inhibiting the growth of hexagonal flakes

It was observed that during electrodeposition of ZnO films that aside from nanorod structures, hexagonal flake structures were also grown. Compared to the nanorod structures, the sizes of the hexagonal flakes are much larger and range in the micron scale. Due to their large size and size difference with the nanorods, micron-sized hexagonal flakes are incompatible with the nanorod structure for hybrid solar cell applications.

The presence of the micron-sized hexagonal flakes poses drawbacks on the optical properties of the ZnO film and on the structure of the hybrid solar cell device. As discussed in the previous section, nanostructures with sizes close to or beyond the wavelength of visible light will cause scattering and lower the optical transmittance of the film. Furthermore, hexagonal flakes in the micron size are incompatible with the design of the inverted bulk heterojunction hybrid solar cells fabricated in this research. The thickness of organic active layers is usually a few hundred nanometers thick. It is limited by the short diffusion range or excitons in organic materials. Hence, micron-sized hexagonal flakes in hybrid solar cells will not be fully covered by the organic active layer - their tips will be sticking out of the organic layer. When the electrodes are deposited, the uncovered tips will become short circuit paths. The uneven surface is not favorable for depositing a continuous layer of gold film for the electrode. The tips that stick out of the organic layer even act as shadow masks that prevent the deposition of gold on the areas behind it.

Due to the incompatibility of the hexagonal flakes to the hybrid solar cell devices fabricated in this study, the elimination of these structures when growing ZnO nanostructured films by electrodeposition is of interest. The ideal nanostructure of the electrodeposited ZnO film is that of ordered nanorod arrays.

ZnO has a wurtzite crystal structure that is made up of alternating planes composed of coordinated $O^{2-}$ and $Zn^{2+}$ ions, stacked one after the other along the c-axis [32]. Because of its crystal structure, growth along the <0001> direction (c-axis) for ZnO is energetically favorable due to the higher surface energy of the polar plane. In the aqueous solution, the anisotropic growth of the ZnO crystals along the c-axis proceeds through the adsorption of $Zn(OH)_4^{2-}$ growth units onto the (0001) plane, resulting in the fast growth along the c-axis. The intrinsic habit of a single crystal is, therefore, prism-like.

It has been suggested by Xu et al. that the growth of hexagonal flakes in chloride electrolytes arises from the preferential adsorption of the $Cl^-$ ions on the (0001) planes [33]. As a result, the expected preferential growth along the c-axis, which results into nanorods is inhibited. So the crystal then preferentially grows along the $(10\bar{1}0)$ plane, which give rise to the hexagonal flake structure. It is further suggested that the Coulombic interaction between the large charge density that accumulated at the plate edges during electrochemical deposition and the cathode lead to the out-of-plane growth, i.e. vertical to the substrate, of the hexagonal flakes.

The strategy adopted in this research, therefore, is to look into the effect of decreasing the $Cl^-$ ions in the electrolyte on the inhibition of the growth of the ZnO hexagonal flakes. The concentration of the supporting electrolyte, KCl, is decreased in order to decrease the $Cl^-$ ions in the solution. In addition, samples will be grown at extended deposition times to observe the evolution of the nanostructure.

This section discusses the effects of decreased KCl concentration and deposition time on the growth of the nanostructures and on the inhibition of the growth of hexagonal flakes.

### 2.4.1 Nanostructure

ZnO nanostructured films were grown by electrochemical deposition on seeded ITO substrates. The deposition of the seed layer is discussed in previous sections. The specific conditions for electrochemical deposition of these set of samples are described. Electrochemical deposition of ZnO on ZnO-seeded ITO substrates were carried out on an RDE setup with a Zn wire counter electrode and saturated calomel electrode (SCE) reference. Deposition was performed for 10 min, 30 min, and 60 min with a rotation speed of 300 rpm and at a fixed potential of −1.0 V versus SCE with a Hokuto Denko HSV-110 potentiostat. Six electrolyte solutions were prepared, all contained and 5 mM $ZnCl_2$. For three of these solutions, the concentration of the supporting electrolyte KCl was 0.1 M, the other three, and 0.05 M. The electrolyte solutions were kept at 70 °C during deposition. The solution was bubbled with $O_2$ through a glass frit prior to and during the deposition process.

The figure below shows the top view SEM images of the deposited ZnO films on seeded ITO substrates. The images in the top row (a), (b), and (c) were deposited in electrolytes with a decreased KCl concentration of 0.05 M KCl. The images in the bottom row (c), (d), and (e) were deposited in electrolytes with 0.1 M KCl.

The effect of decreasing the concentration of the electrolyte from 0.1 M to 0.05 M on the growth of the hexagonal flakes is evident. The number of the hexagonal flakes that grew in the lower KCl concentration is fewer. Moreover, the sizes of these hexagonal flakes are distinctly smaller; the width of the flakes are at about 5 μm. The width of the hexagonal flakes grown in 0.1 M KCl concentration grow up to about 30 μm.

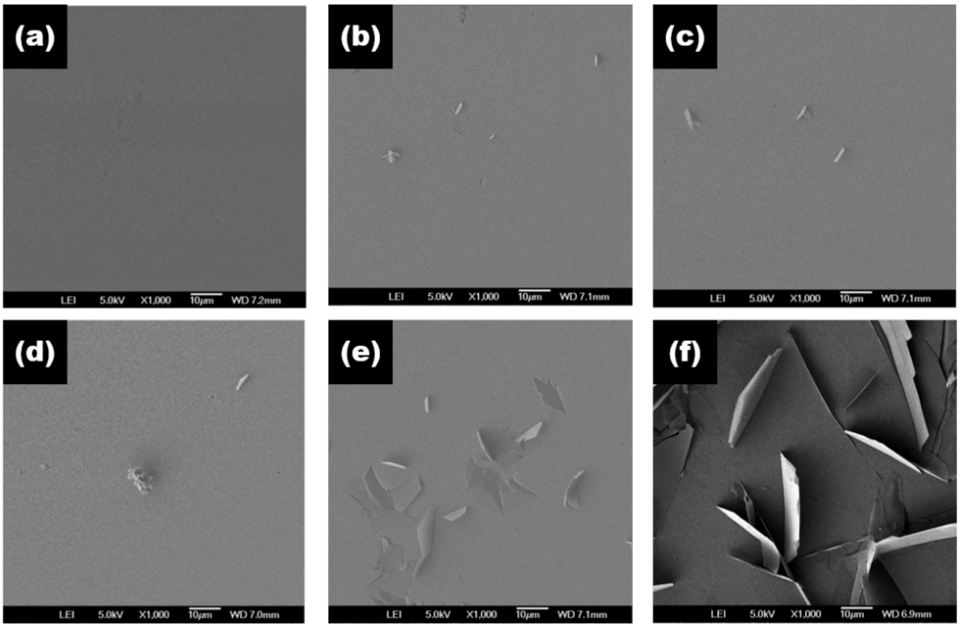

Figure 2.16 SEM images of the ZnO films deposited on seeded ITO substrates in 0.05 M KCl (a) 10 min, (b) 30 min, and (c) 60 min; and in 0.1 M KCl (d) 10 min, (e) 30 min, and (f) 60 min.

The growth of the hexagonal flakes with deposition time can also be seen in this figure. The deposition time is 10 min for the films shown in Figure 2.16 (a) and (d), 30 min for (b) and (e), and 60 min for (c) and (f). For both KCl concentrations, growth in the sizes of the hexagonal flakes is observed. At 0.05 M KCl, the growth in the size of the hexagonal flakes is very small. At a deposition time of 10 min, no hexagonal flakes were observed to be growing on the film. At longer deposition times, however, the hexagonal flakes grew. Comparing (b) and (c), the width of the hexagonal flake increased from about 3 μm to about 5 μm. On the other hand at 0.1 M KCl, the growth in the sizes of the hexagonal flakes are is easily observed. At 10 min deposition time, the width of the flake is about 5 μm, increasing to about 15 μm at 30 min, to about 30 μm at 60 min.

According to the study by Xu et al. [33], the hexagonal flake structure arises from the preferential adsorption of $Cl^-$ ions on the (0001) planes. This experiment demonstrates that the KCl concentration has an effect on the growth mechanism of the ZnO hexagonal flakes.

Decreasing the Cl$^-$ ion concentration by cutting the KCl concentration in half, from 0.1 M to 0.05M, decreases the number of hexagonal flakes as well as inhibits the growth in size of the said hexagonal flakes. Xu et al., however, notes in their study that different Cl$^-$ ion sources (NaCl and KCl) have different effects on the array manner of the ZnO plates.

While the film looks smooth and featureless, Figure 2.16 (a) is an image of a nanorod array. The magnification is just too low to observe the features of the nanostructure. Likewise, the smooth areas surrounding the flakes in the rest of the images are made up of nanorod arrays.

To observe the nanorod array structures, the same samples were imaged at a higher magnification in the SEM. These are shown in Figure 2.17. The same letters in this set of images correspond to the same samples shown in Figure 2.16. The top row of images are grown in 0.05 M KCl and the bottom row at 0.1 M KCl. The deposition time for left column, (a) and (d), is 10 min; for the middle column, (b) and (e), 30 min; and the right column, (c) and (f), 60 min.

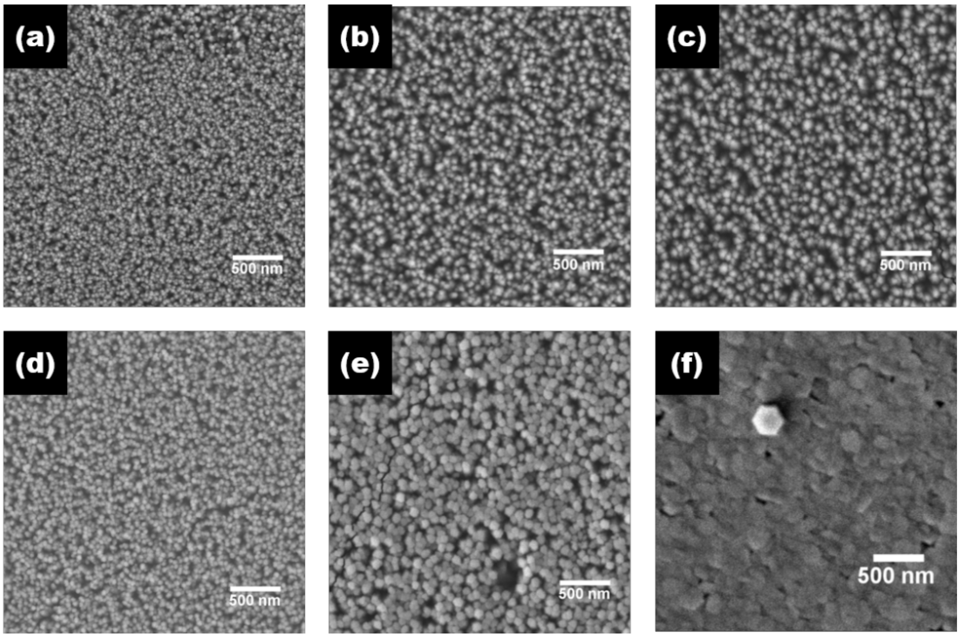

Figure 2.17 Higher magnification SEM images of the ZnO films deposited on seeded ITO substrates in 0.05 M KCl (a) 10 min, (b) 30 min, and (c) 60 min; and in 0.1 M KCl (d) 10 min, (e) 30 min, and (f) 60 min.

It can be seen from this figure that the concentration of KCl also has an impact on the morphology of the nanorods. The nanorod arrays grown at a lower KCl concentration, 0.05 M, had a more open array structure, whereas the nanorod arrays grown at a higher KCl concentration, 0.01 M, had a more compact structure. The difference in the shape of the single crystals are more evident at longer deposition times. Figure 2.17 (b) 0.05 M KCl and (e) 0.1 M KCl, both 30 min deposition time, show the tips of the single crystal nanorods are different. The nanorod tips are tapered in (b) while the tips are flat in (c).

Figure 2.17 also shows that at the deposition time affects the diameter of the nanorods. At longer deposition times, the diameter of the nanorods increases for both KCl concentrations. This suggests that although the growth of the crystal is preferentially along the c-axis, there is still growth along the $(10\bar{1}0)$ planes.

The deposition time also affects the density of the nanorod array. At longer deposition times, the nanorod array becomes more compact. This is more clearly demonstrated in the case of 0.1 M KCl. Figure 2.17 (f), at 60 min deposition time, shows a compact film structure where it is difficult to distinguish individual nanorod single crystals as the spaces in between have become nonexistent.

Because of its crystal structure, growth along the <0001> direction (c-axis) for ZnO is energetically favorable due to the higher surface energy of the polar plane. The difference in the shape of the tips of the nanorods in this experiment indicate that presence of $Cl^-$ ions in the solution act as a capping agent on the electrodeposition of ZnO nanorods. The preferential adsorption of the $Cl^-$ ions on the (0001) planes favors the stabilization of this plane and promotes the lateral growth of the nanorod. As a result nanorods with flat tips are grown.

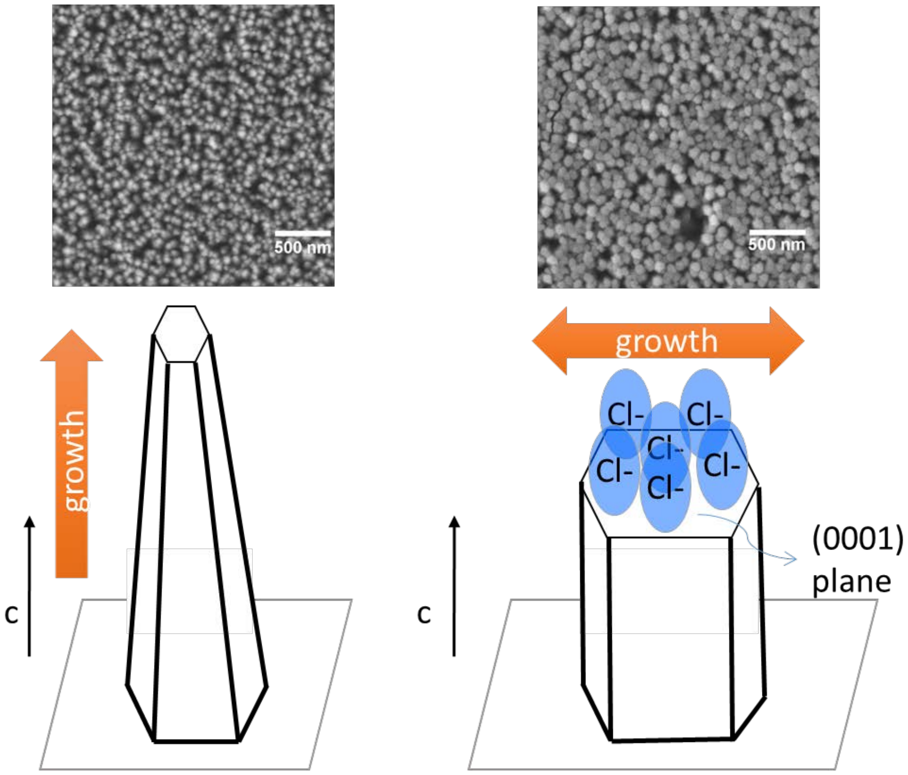

Figure 2.18 Illustration of the role of $Cl^-$ ions as capping agents on the growth of ZnO nanorod structures.

A recent study has shown that the diameter of the ZnO nanorods increases with increasing KCl concentration, indicating that the lateral growth of nanorods is favored at higher chloride content (>1.0M) [34]. On the other hand, at a lower KCl concentration the effect of the $Cl^-$ ions as capping agents are less pronounced. Growth along the c-axis (vertical) is faster compared to lateral growth, resulting in a tapered tip.

The cross-section of the deposited ZnO films are imaged with SEM to know more about the nanostructure. These images are shown in Figure 2.19. Because these images are taken after the samples have been fabricated into hybrid solar cells, the organic active layer and the metallic electrode layers can also be seen. The same letters in this set of images correspond to the same samples shown in Figure 2.16. The top row of images are grown in 0.05 M KCl and the bottom row at 0.1 M KCl. The deposition time for left column, (a) and (d), is 10 min; for the middle column, (b) and (e), 30 min; and the right column, (c) and (f), 60 min.

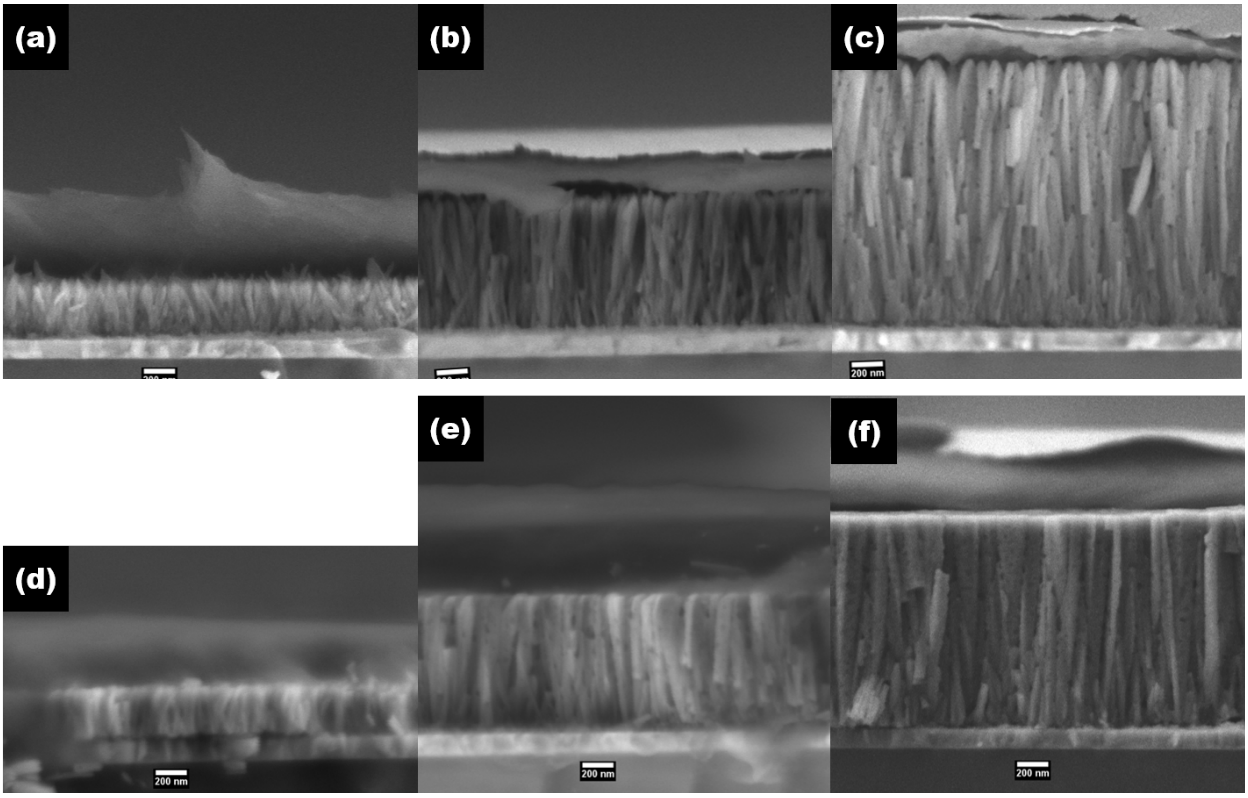

Figure 2.19 Cross-section SEM images of the ZnO films deposited on seeded ITO substrates in 0.05 M KCl (a) 10 min, (b) 30 min, and (c) 60 min; and in 0.1 M KCl (d) 10 min, (e) 30 min, and (f) 60 min. The scale bars are 200 nm.

All of the images are taken at the same magnification. The scale bars are 200 nm. To aid in comparing the structures, the images are placed side by side and are aligned using the 150 nm ITO layer as a guide. The thickness of the ZnO film increases with longer deposition time. The difference in the single crystal nanostructures can also be observed in these cross-section images. The tapered tips of the nanorods grown in 0.05 M KCl can be seen as well as the flat tips of the nanorods grown in 0.1 M KCl.

These images show how the density of the array decreases with deposition time. In Figure 2.19 (a), it can be seen that there are spaces in between the individual nanorods in the top half of the nanorod. The organic active layer can be seen to be filling up these spaces. The bottom half of the nanorods seem to be a compact ZnO layer. In Figure 2.19 (b), it can be seen that the spaces between the nanorods observed in the top view image, Figure 2.17 (b), is limited only to the tips of the tapered tips of the nanorods. Below the tapered tips, the single crystal nanorods already form a compact structure with no spaces. It can also be observed that there are more nanorods in the bottom than there are at the top. This indicates that the growth in the diameter of the nanorods causes overcrowding. Eventually the lack of space prevents other nanorods to grow in length. As a result, with increasing deposition time, there are fewer nanorods per area, i.e. lower density of the nanorod array. The same description can also be said of Figure 2.19 (c).

For the samples grown in 0.1 M KCl, it can be seen that the nanorod array has a more compact nanorod array. In addition to the flat tips, it is more difficult to distinguish the single crystal nanorods apart from one another.

### 2.4.2 Optical properties

The optical properties of deposited ZnO films are evaluated my measuring the optical transmittance with UV-Vis spectrometry. From this data, the band gap of the ZnO films can be estimated by the Tauc plot analysis.

Figure 2.20 shows the optical transmittance of the deposited ZnO films. The samples grown at 10 min deposition times both display high optical transmittance, up to 90%. The samples grown at 60 min deposition times both display low optical transmittance, about 60 to 70%. The sample grown for 30 min in 0.1 M KCl also showed similar low optical transmittance, about 60%. The sample grown for 30 min in 0.05 M KCl, however, also displays a high optical transmittance similar to the samples grown for 10 min.

The high transmittance of the 10 min samples can be attributed to the size of the nanostructures and the high order of vertical orientation. The low optical transmittance of the

30 min sample grown in 0.1 M KCl can be attributed to the presence of hexagonal flakes. Conversely, the high optical transmittance of the 30 min sample grown in 0.05 M KCl can be attributed to the low number and small size of these hexagonal flakes. The high optical transmittance of the 30 min sample grown in 0.05 M KCl can be attributed to the low transmittance of the 60 min samples, on the other hand, can be attributed to the hexagonal flakes and on the thickness of the film.

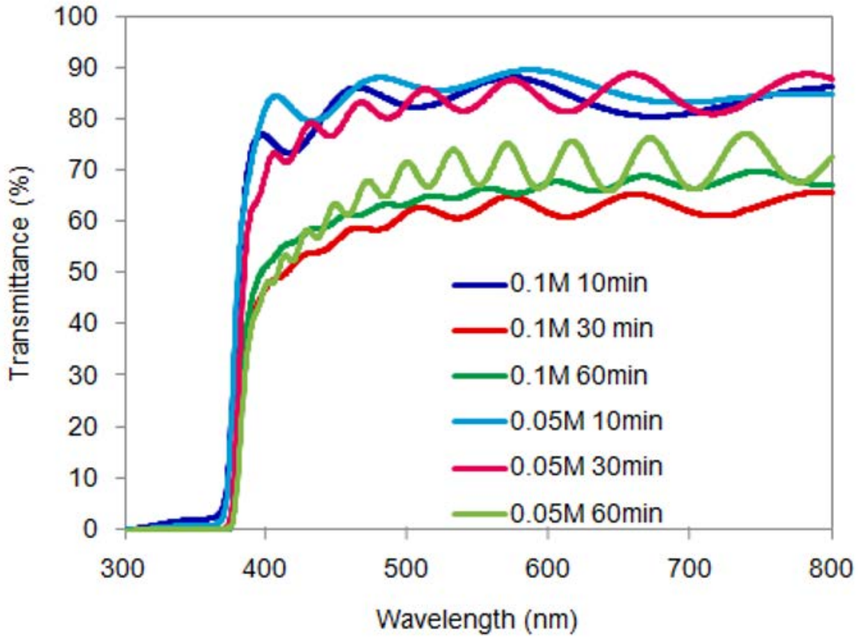

Figure 2.20 Optical transmittance spectra of the ZnO films deposited in 0.05 M and 0.1 M KCl concentrations; and in deposition times of 10, 30, and 60 min.

The optical bandgaps of the deposited ZnO films are estimated from the Tauc plot derived from the optical transmittance data. The Tauc plot for the deposited ZnO samples are shown in Figure 2.21. The estimated optical band gaps for the 10 min samples are similar at 3.31 eV. This value is consistent with the optical band gap of intrinsic ZnO in literature, $E_g$ = 3.3 eV [35]. The estimated optical band gaps for the samples deposited at longer deposition times, 30 and 60 min, are interestingly lower at about 3.27 eV.

The change in the band gap of the electrodeposited ZnO film can be attributed to high $Cl^-$ ion doping of the ZnO film. Recent studies have reported Cl doping in ZnO grown by electrochemical deposition in a chloride electrolyte [36]. Cl doping in ZnO is reported to result in optical band gap widening, referred to as the Burstein-Moss effect. On the other hand, band gap narrowing was observed for semiconductors at increasing carrier concentration [37]. At a doping concentration above the critical carrier concentration called the Mott density, the merging of the donor level and the conduction band cause band gap narrowing. Longer deposition times 30 min and 60 min might result in higher $Cl^-$ ion doping in ZnO to cause band gap narrowing.

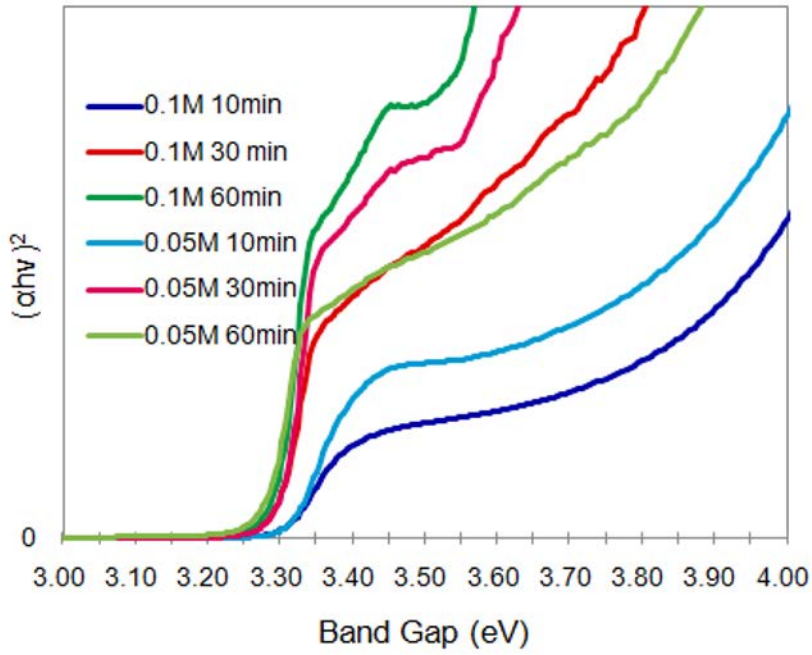

Figure 2.21 Tauc plot of the ZnO films deposited in 0.05 M and 0.1 M KCl concentrations; and in deposition times of 10, 30, and 60 min.

The space in between the nanorods is an important aspect in ordered bulk heterojunction hybrid solar cells. These spaces affect the overall available interfacial area and they also act as a nanostructure pattern for the organic active layer. Hence, ZnO films grown at longer deposition times at 30 min and 60 min are not suitable for hybrid solar cell applications.

While the density of the nanorods decreased with increasing deposition time, the space between the nanorods are only limited to the tips. Below these tips, the nanorods have already formed a compact structure that cannot be infiltrated by the organic active layer.

### 2.4.3 Hybrid solar cell characteristics

Hybrid solar cells were fabricated from the electrochemically deposited ZnO films following the inverted bulk heterojunction structure. The current density-voltage plots for the samples grown in 0.05 M KCl (10, 30, 60 min) are shown in Figure 2.22 while those grown in 0.1 M KCl (10, 30, 60 min) are shown in Figure 2.23.

The highest *PCE*, 0.27%, is obtained from the 0.05 M KCl (10 min) sample. This can be attributed to the larger interfacial area available in the device. The cross-section images showed that this sample had spaces in between the nanorods that the active layer was able to fill.

For both sets of samples, 0.05 M and 0.1 M, the fill factor decreases with increasing deposition time. The decrease in the fill factor can be attributed to the increase in series resistance as well as a decrease in the shunt resistance. The increase in series resistance comes from the increased thickness of the ZnO film at longer deposition times. The decrease in the shunt resistance comes from the hexagonal flakes that grow larger in number and in size at longer deposition times. Because the hexagonal flakes are much larger than the thickness of the active layer, they create protrusions and could act as short circuit paths.

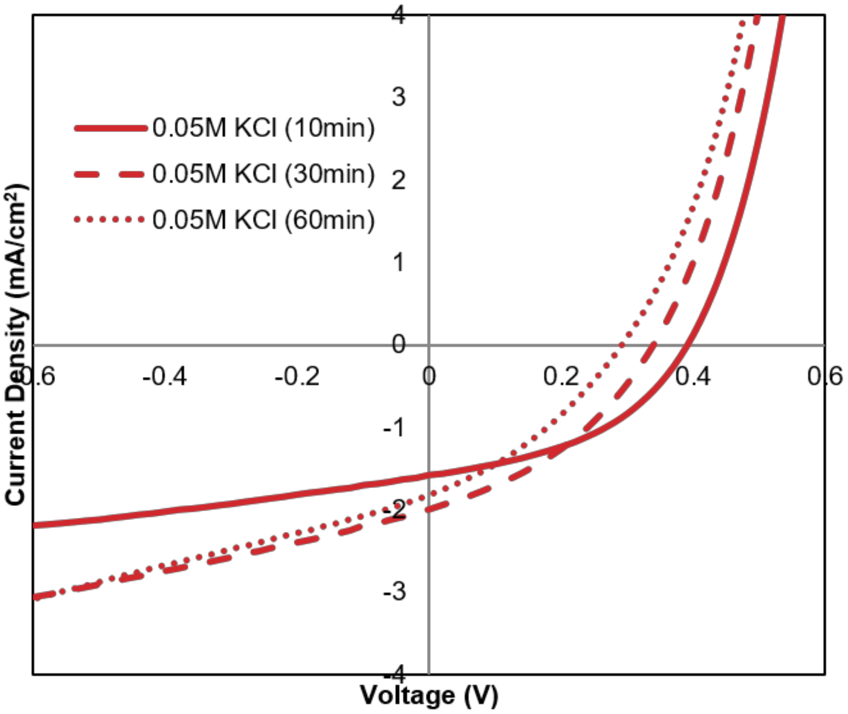

Figure 2.22 *JV*-curve for hybrid solar cells with ZnO grown in 0.05 M KCl.

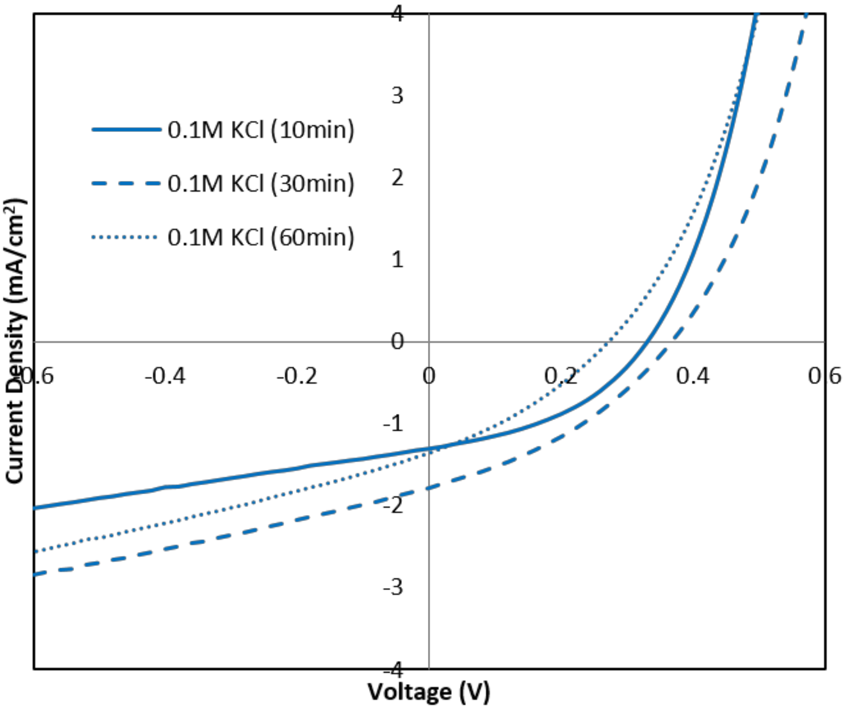

Figure 2.23 JV-curve for hybrid solar cells with ZnO grown in 0.1 M KCl.

Table 1 Summary of device performance

| | | *Voc* (V) | *Jsc* (mA/cm$^2$) | *FF* | *PCE* (%) |
|---|---|---|---|---|---|
| 0.05 M KCl | 10 min | 0.4 | 1.58 | 42.59 | 0.27 |
| | 30 min | 0.34 | 1.99 | 37.11 | 0.25 |
| | 60 min | 0.3 | 1.81 | 32.77 | 0.18 |
| 0.1 M KCl | 10 min | 0.34 | 1.31 | 39.98 | 0.18 |
| | 30 min | 0.36 | 1.78 | 36.60 | 0.23 |
| | 60 min | 0.28 | 1.37 | 31.67 | 0.12 |

## 2.5 ZnO nanostructure film as a cathode buffer layer

The results of the experiments from the previous subsections served as guidelines in growing a more optimized ZnO nanostructure film for inverted hybrid solar cell applications. Depositing a ZnO seed layer is necessary for growing ordered nanorod arrays. In addition, decreasing the concentration of KCl in the electrolyte from 0.1 M to 0.05 M inhibits the growth of micron-sized hexagonal flakes that are detrimental to the hybrid solar cell device structure. Finally, longer deposition times, i.e. 30 min or 60 min, are not necessary since a very thick (>1 μm) degrades the fill factor of the hybrid solar cell.

The specific conditions for electrochemical deposition of a more optimized ZnO nanostructured film is described. Electrochemical deposition of ZnO on ZnO-seeded ITO substrate was carried out on an RDE setup with a Zn wire counter electrode and saturated calomel electrode (SCE) reference. Deposition was performed 95 s with a rotation speed of 300 rpm and at a fixed potential of −1.0 V versus SCE. The electrolyte solutions contained and 3 mM $ZnCl_2$ and 0.025 M KCl. The electrolyte solution was kept at 70 °C during deposition. The solution was bubbled with $O_2$ through a glass frit prior to and during the deposition process.

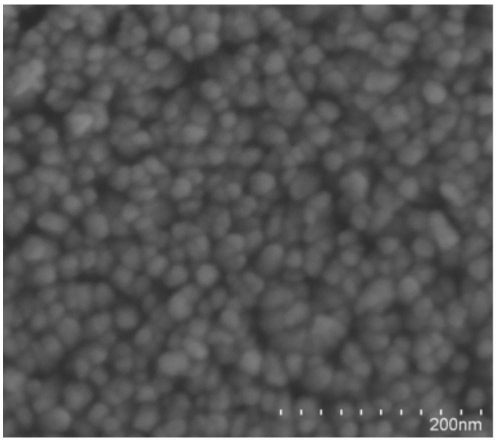

Figure 2.24 SEM image of ZnO nanostructured film (0.025 M KCl, 95 s).

The SEM image of the deposited ZnO nanostructured film is shown in **Error! Reference source not found.**. The nanorods have a diameter of about 20 nm and length of about 60 nm. The nanorods are highly ordered. The lengths of the nanorods are uneven, creating a larger surface area.

A hybrid solar cell was fabricated from this ZnO film. For comparison, hybrid solar cells using ZnO seed layer and bare ITO are fabricated. The ZnO seed layer used here is deposited by spin-coating the precursor solution three times. It is thicker (~50 nm) compared to the seed layers used in electrodeposition (~30 nm). This particular seed layer, therefore, is very similar to the electrodeposited ZnO nanorod film in thickness but different in nanostructure. Figure 2.25 shows a diagram of the devices fabricated.

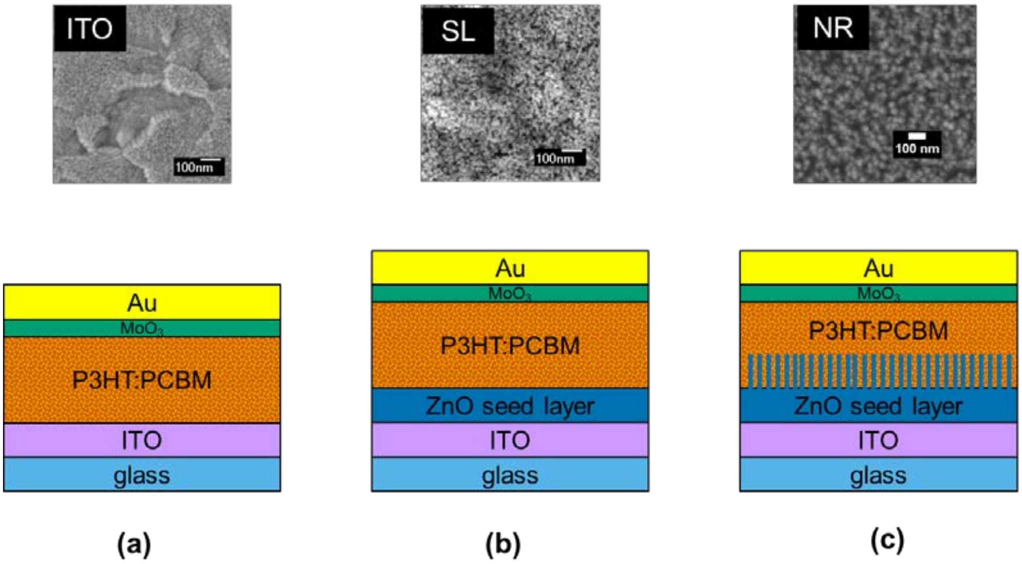

Figure 2.25 Diagrams of hybrid solar cells fabricated on (a) bare ITO, (b) ZnO seed layer (SL), and (c) ZnO nanorod (NR).

The *JV*-curves are shown in Figure 2.26. The parameters are summarized in Table 1. The device fabricated using bare ITO had the lowest *PCE* at 0.27%. It has a very low $V_{OC}$ arising from the direct contact of the active layer and the ITO surface, resulting in recombination losses. The *JV*-curve has an S shape that is indicative of energetic mismatch between the work function of the ITO and PCBM which leads to barriers towards charge carrier injection.

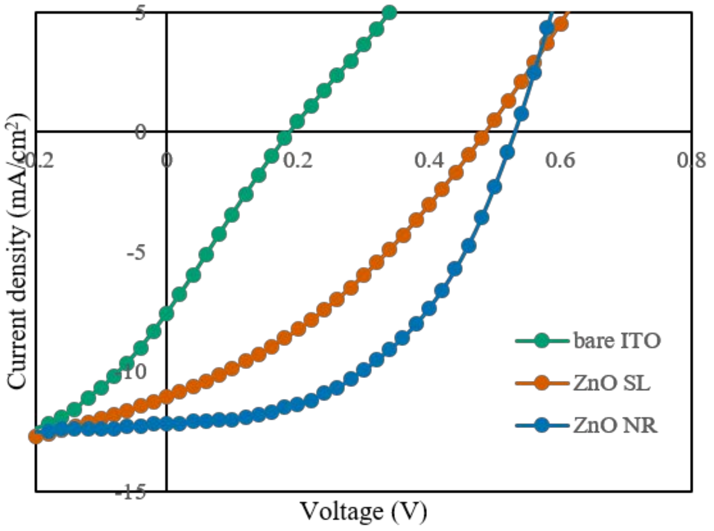

Figure 2.26 Current density-voltage characteristics of hybrid solar cells fabricated using bare ITO, ZnO seed layer (SL), and ZnO nanrod film (NR).

Table 2 Summary of device performance, average and standard deviation in brackets

| | *Voc* (V) | *Jsc* (mA/cm$^2$) | *FF* | *PCE* (%) |
|---|---|---|---|---|
| bare ITO | 0.17<br>[0.15±0.05] | 6.79<br>[5.29±2.04] | 24.09<br>[23.28±0.71] | 0.275<br>[0.20±0.12] |
| ZnO SL | 0.48<br>[0.46±0.02] | 11.08<br>[7.38±2.78] | 34.27<br>[37.82±6.36] | 1.82<br>[1.25±0.38] |
| ZnO NR | 0.51<br>[0.51±0.01] | 12.19<br>[11.69±0.70] | 46.92<br>[45.09±2.36] | 2.92<br>[2.70±0.35] |

Figure 2.27 shows the energy diagram of the hybrid solar cell fabricated on bare ITO, without ZnO. Because the work function of ITO (4.8 eV) is close to the LUMO level of P3HT and the HOMO level of PCBM, ITO is widely used as an electrode for hybrid solar cells in both the conventional and inverted geometries. In both geometries, however, the significant energy level difference between ITO and the active layer material leads to a non-Ohmic contact that degrades the $V_{OC}$ [38]. For the inverted device in this study, the energy level difference between ITO and the HOMO level of PCBM is of interest.

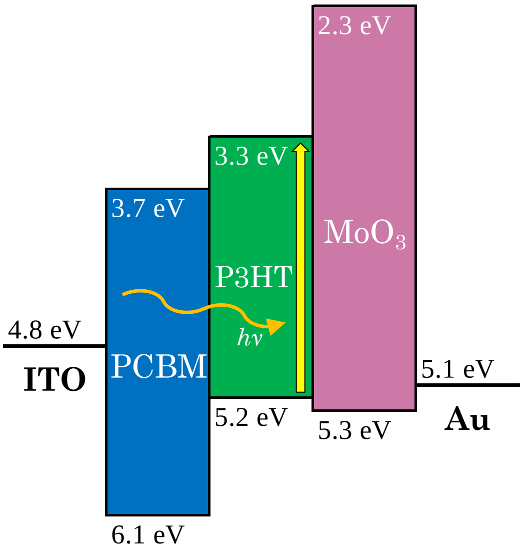

Figure 2.27 Energy diagram of the hybrid solar cell fabricated on bare ITO, without ZnO.

In addition, because of the work function of ITO, it can collect both electrons and holes, ITO does not have strong charge selectivity. This is a problem in bulk heterojunction solar cells where the donor and acceptor phases are in direct contact with the ITO electrode, making exciton quenching at this interface is unavoidable.

Compared to the device fabricated on bare ITO, the devices with ZnO seed layer and ZnO nanorods exhibited an improvement in the solar cell characteristics. In particular, a large improvement on the $V_{OC}$ and $J_{SC}$ is observed with the addition of ZnO.

Figure 2.5 shows the energy diagram of the hybrid solar cell fabricated on ZnO covered ITO. The energy levels of ZnO make the layer appropriate to act as an electron-selective interlayer, preventing the collection of holes. $MoO_3$, similarly, acts as a hole-selective layer. These layers allow the selective transport of electrons to the ITO electrode and holes to the Au electrode, eliminating exciton quenching at the interfaces.

The intermediate work function of ZnO between ITO and PCBM establishes an Ohmic contact which reduces electron accumulation at the interface. Note that the curve does not exhibit an S shape. Recombination at the interface is reduced as a result. The lower work function of ZnO compared to ITO also serves to increase the built in potential in the device, which increases extraction efficiency. While $V_{OC}$ in excitonic devices is not yet fully understood, the built in potential is theorized to be the upper limit for $V_{OC}$. The addition of ZnO between ITO and active layer, therefore, reduces recombination and increases the built in potential leading to a large improvement in the $V_{OC}$ of the device.

Between the two devices fabricated with ZnO, the device with ZnO nanorod film had a better solar cell characteristic, with a *PCE* of 2.9%. The improved *PCE* can be attributed to the increase in FF from 34.27 in the device with ZnO seed layer to 46.92 in the device with ZnO nanorods.

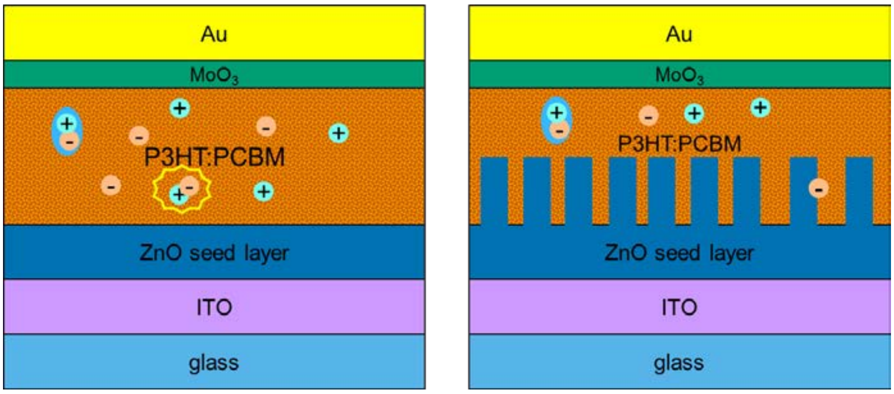

Figure 2.28 Comparing charge extraction in device with ZnO SL and ZnO NR.

The increased *FF* arises from a decreased series resistance and an increased the shunt resistance. The decreased series resistance can be attributed to the better mobility of the single crystal nanorods compared to that of the multiple nanocrystals that make up the seed layer. Because the seed layer is made up of multiple nanocrystals, there are many grain boundaries encountered as the electron is transported to the ITO electrode. In comparison, a nanorod is a single crystal provides a direct charge transport path. The improvement in shunt resistance can be attributed to reduced recombination at the ZnO interface as a result of the larger surface area of the nanorods.

There is a small improvement in $V_{OC}$ and also in $J_{SC}$. The improvement in $J_{SC}$ can be attributed to the larger interfacial area of the nanorod film compared to the seed layer film, which aids the charge extraction. Recombination is more likely in a planar structure because of longer diffusion distances separated charges have to travel to reach the electrodes. With a nanorod array structure, separated charges can be collected more efficiently due to its large surface area and interpenetrating network with the organic layer.

## 2.6 Summary

ZnO nanostructured films were electrochemically deposited on bare ITO and seeded ITO substrates. The nanorod arrays deposited on the seeded ITO substrates were composed of densely packed nanorods about 100 nm in diameter, having a high degree of orientation perpendicular to the substrate.

The optical transmittance is higher and the crystal defect concentration is lower for the ZnO grown on the seeded ITO substrates compared to the ZnO deposited on bare ITO substrates. Chronoamperometric transient curves reveal that nucleation and coalescence takes a longer time on the bare ITO substrates, thus giving rise to larger nanorods with a lower degree of orientation.

Due to better morphology and optical transmittance, the hybrid solar cells fabricated on the seeded ITO substrates had higher power conversion efficiencies. The ZnO seed layer, aside from providing nucleation sites also acts as a hole-blocking layer, promoting charge carrier separation.

The growth of micron-sized hexagonal flakes were successfully inhibited by decreasing the KCl concentration in the electrolyte from 0.1 M to 0.05 M. The result of the experiment supports the growth mechanism model proposed by Xu et al., where preferentially adsorbed $Cl^-$ stabilizes the ZnO (0001) plane thereby favoring lateral growth resulting to hexagonal flakes.

In addition, the concentration of KCl in the electrolyte also affects the morphology of the nanorods, the tips of the nanorods in particular. At 0.1 M KCl, the nanorods had flat tips while at 0.05 M KCl, the nanorods had tapered tips. This suggests the role of $Cl^-$ ions acting as capping agents in the growth of nanorods. While the growth of nanorods is energetically favorable due to the crystal structure of ZnO, the nanorods also undergo lateral growth, i.e. increased diameters. At the higher concentration, the $Cl^-$ ions are similarly preferentially adsorbed on the ZnO (0001) plane favoring the growth of flat tips. The tapered tips grown at a lower KCl concentration is a result of a faster rate of growth in the c-axis compared to lateral growth due to the fewer $Cl^-$ ion capping agents.

Regardless of KCl concentration, long deposition times (30 and 60 min) result in thick and compact ZnO films that are not suitable for hybrid solar cell applications due to lower optical transmittance and higher series resistance. The result of the experiment, however, demonstrated that a thick and compact film can be grown by electrochemical deposition. The experiment was able to show the evolution of this film from a nanorod array structure to a compact film structure and may be useful for studies that may require thicker ZnO films.

In comparing hybrid solar cell devices fabricated on ZnO seeded ITO substrate and bare ITO substrate, i.e. without any ZnO layer, it was shown that ZnO is an effective cathode buffer layer. With a ZnO layer, recombination losses were reduced and charge collection was improved, resulting in higher $V_{OC}$ and $J_{SC}$.

A more optimized ZnO nanorod film was deposited in an electrolyte with lower KCl concentration (0.025 M) and short deposition time (95 s). The hybrid solar cell fabricated from this film had a *PCE* of 2.9%. Compared to the ZnO seed layer, the ZnO nanorod layer had better charge mobility and larger interfacial area. As a result, *FF* is improved as well as $J_{SC}$.

In summary, this chapter demonstrated the controlled growth of ZnO nanorod films achieved by deposition of a seed layer, controlling the KCl concentration, and deposition time. With careful selection of parameters, ZnO nanorod films appropriate for hybrid solar cell applications were grown.

# References

[1] K. Takahashi, A. Yoshikawa and A. Sanhu, Wide bandgap semiconductors: fundamental properties of modern photonic and electronic devices, Heidelberg: Springer, 2007.

[2] M. Wright and A. Uddin, *Solar Energ. Mater. and Solar Cells,* vol. 107, p. 87, 2012.

[3] E. Meulenkamp, *J. Phys. Chem. B,* vol. 102, p. 5566, 1998.

[4] L. Vayssieres, *Adv. Mater.* , vol. 13, p. 464, 2003.

[5] J. Elias, R. Tena-Zaera and C. Levy-Clement, *J. Electroanal. Chem.,* vol. 621, p. 171, 2008.

[6] D. Pradhan and K. T. Leung, *Phys. Chem. C,* vol. 112, p. 1357, 2008.

[7] T. Yoshida, M. Iwaya, H. Ando, T. Oekermann, K. Nonomura, D. Schlettwein, D. Wohrle and H. Minoura, *Chem. Commun.,* p. 400, 2004.

[8] D. C. Olson, J. Piris, R. T. Collins, S. E. Shaheen and D. S. Ginley, *Thin Solid Films,* vol. 496, p. 26, 2006.

[9] K. Takanezawa, K. Hirota, Q. S. Wei, K. Tajima and K. Hashimoto, *J. Phys. Chem. C,* vol. 111, p. 7218, 2007.

[10] X. D. Gao, F. Peng, X. M. Li, W. D. Yu and J. J. Qiu, *J. Mater. Sci.,* vol. 42, p. 9638, 2007.

[11] S. Sun, S. Jiao, K. Zhang, D. Wang, H. Li, S. Gao, J. Wang, Q. Yu, F. Guo, L. Zhao and S. Su, *J. Mater. Sci.: Mater. Electron.,* vol. 24, p. 85, 2013.

[12] S. P. Anthony, J. I. Lee and J. K. Kim, *Appl. Phys. Lett.,* vol. 90, p. 103107, 2007.

[13] Y. Natsume and H. Sakata, *Thin Solid Films,* vol. 372, p. 30, 2000.

[14] M. Ohyama, H. Kozuka and T. Yoko, *Thin Solid Films,* vol. 306, p. 78, 1997.

[15] A. E. J. Gonzáles, J. A. S. Ureta and R. S. Parra, *J. Cryst. Growth,* vol. 192, p. 430, 1998.

[16] R. Brenier and L. Ortega, *J. Sol-gel Sci. Technol.* , vol. 29, p. 137, 2004.

[17] L. Znaidi, *Mater. Sci. Eng. B,* vol. 174, p. 18, 2010.

[18] A. Goux, T. Pauporte and D. Lincot, *Electrochim. Acta,* vol. 50, p. 2239, 2005.

[19] T. Pauporte and D. Lincot, *Electrochim. Acta,* vol. 45, p. 3345, 2000.

[20] L. E. Greene, M. Law, D. H. Tan, M. Montano, J. Goldberger, G. Somorjai and P. Yang, *Nano Lett.*, vol. 5, p. 1231, 2005.

[21] Z. Zheng, Z. S. Lim, Y. Peng, L. You, L. Chen and J. Wang, *Sci. Rep.* , vol. 3, p. 2434, 2013.

[22] Y. J. Lee, D. S. Ruby, D. W. Peters, B. B. McKenzie and J. W. P. Hsu, *Nano Lett.*, vol. 8, p. 1501, 2008.

[23] L. Hu and G. Chen, *Nano Lett.*, vol. 7, p. 3240, 2007.

[24] M. Izaki and T. Omi, *Appl. Phys. Lett.*, vol. 68, p. 2439, 1996.

[25] B. Illy, B. A. Shollock, J. L. MacManus-Driscoll and M. P. Ryan, *Nanotechnology*, vol. 16, p. 320, 2005.

[26] A. B. Djurišić, W. C. H. Choy, V. A. L. Roy, Y. H. Leung, C. Y. Kwong , K. W. Cheah, T. K. Gundu Rao, W. K. Chan, H. F. Liu and C. Surya, *Adv. Func. Mater.* , vol. 14, p. 856, 2004.

[27] M. A. Reshchikov, J. Q. Xie, B. Hertog and A. Osinsky, *J. Appl. Phys.* , vol. 103, p. 103514, 2008.

[28] D. C. Iza, D. Munoz-Rojas, Q. Jia, B. Swartzentruber and J. L. MacManus-Driscoll, *Nanoscale Res. Lett.*, vol. 7, p. 655, 2012 .

[29] K. Vanheudsen, W. L. Warren, C. H. Seager, D. R. Tallant, J. A. Voight and B. E. Grande, *J. Appl. Phys.* , vol. 79, p. 7983, 1996.

[30] A. B. Djurišić, Y. H. Leung, K. H. Tam, L. Ding, W. K. Ge, H. Y. Chen and S. Gwo, *Appl. Phys. Lett.* , vol. 88, p. 103107, 2006.

[31] K. H. Tam, C. K. Cheung, Y. H. Leung, A. B. Djurišić, C. C. Ling, C. D. Beling, S. Fung, W. M. Kwok, W. K. Chan, D. L. Phillips, L. Ding and W. K. Ge, *Phys. Chem. B.,* vol. 110, p. 20865, 2006.

[32] X. Y. Kong and Z. L. Wang, *Nano Lett.,* vol. 3, p. 1625, 2003.

[33] F. Xu, Y. Lu, Y. Xie and Y. Lu, *Mater. Des.,* vol. 30, p. 1704, 2009.

[34] H. Y. Yang, Y. S. No, J. Y. Kim and T. W. Kim, *Jpn. J. Appl. Phys.,* vol. 51, p. 06FG13, 2012.

[35] Ü. Özgür, Y. I. Alivov., A. Teke, M. A. Reshchikov, S. Doğan, V. Avrutin, S. -J. Cho and H. Morkoç, *Appl. Phys. Lett.*, vol. 98, p. 041301, 2005.

[36] S. Hori, T. Suzuki, T. Suzuki, S. Miura and S. Nonomura, *Mater. Tran.,* vol. 55, p. 728, 2014.

[37] J. Kumar and A. K. Srivastava, *J. Appl. Phys.,* vol. 115, p. 134904, 2014.

[38] T. Tromholt and F. C. Krebs, "Polymers, Nanomaterials, and Organic Photovoltaic Devices," in *Nanomaterials, Polymers, and Devices: Materials Functionalization and Device Fabrication,* E. S. W. Kong, Ed., Hoboken, New Jersey: John Wiley and Sons, Inc., 2015, p. 319.

# 3 Electrochemical deposition of aluminum-doped ZnO

## 3.1 Introduction

Combining the low cost processing of polymer thin films and the stability of inorganic films to produce energy from light, hybrid organic-inorganic solar cells are promising next generation photovoltaic technology [1,2]. To date, inverted hybrid solar cell structures with high work function electrodes and metal oxide cathode buffer layers have been widely studied because of better ambient device stability compared with the conventional structure [3,4]. In addition, using a nanostructured metal oxide layer such as ZnO nanorod arrays are predicted to improve device performance because it provides carrier transport paths with increased interface areas and the added benefit of shaping the morphology of the film [5].

Aluminum-doped ZnO (AZO) films have recently been demonstrated as inorganic layers for hybrid solar cells [6] and used applications such as organic light emitting diodes [7] and thin film transistors [8]. Aluminum doping of ZnO can further improve its conductivity and modify its band gap [9, 10]. Electron transport resistance improvement was reported for bulk heterojunction solar cells [11, 12] and dye-sensitized solar cells [13] where AZO was used as cathode buffer layers and photoanodes, respectively.

In this study, AZO films were grown on ITO substrates by electrochemical deposition. It is a versatile method to grow AZO nanostructures because it is quick, low-cost, and performed at low temperatures. Furthermore, it facilitates in-situ doping of the dopant into the host lattice [14, 15]. Past works on the electrochemical deposition of AZO used a nitrate electrolyte for the source of zinc and aluminum; here, the growth of AZO from a chloride electrolyte is demonstrated. Recent studies showed that preparation of ZnO from chloride-containing electrolytes leads to doping and a Burstein-Moss shift, that is, apparent shift of the band gap energy by filling of states at the bottom of the conduction band [16, 17]. The present work, therefore, adds valuable information on the subject.

These Al-doped ZnO samples are then used to fabricate inverted hybrid solar cells with Au/MoO3/P3HT:PCBM/AZO/seed-layer/ITO/glass structures.

## 3.2 Experimental

This section describes the methods in preparing aluminum-doped ZnO films by electrochemical deposition on ZnO-seeded ITO substrates. Aluminum doping is achieved by adding a relatively small amount of aluminum chloride hexahydrate to the electrolyte. These films were then used to fabricate hybrid solar cells to evaluate their performance as cathode buffer layers.

### 3.2.1 Electrodeposition

AZO films were electrodeposited on seeded ITO/glass substrates in a chloride electrolyte with a rotating disk electrode set-up. The electrolyte contained 0.05 M KCl and 3 mM $ZnCl_2$; small amounts of aluminum chloride hexahydrate ($AlCl_3 \cdot 6H_2O$) were added to obtain solutions with Al/Zn molar ratios of 0.5%, 2.5%, and 5.0%. The electrolyte was kept at 70°C and saturated with oxygen prior to and during deposition. Potentiostatic electrodeposition proceeded on the working electrode rotating at 300 rpm for 300 s at -1.0V vs. a saturated calomel electrode (SCE), using zinc wire as a counter electrode.

Before deposition, the ITO substrates were cleaned by ultrasonication in water, acetone, and ethanol. Then either a ZnO seed layer or an AZO seed layer was deposited on the ITO substrate by modified techniques outlined in previous studies [18, 19]. The seed layers were deposited by spin-coating methanolic precursors followed by annealing for 30 min at 350 °C.

The precursor for the undoped ZnO seed layer was prepared by mixing a 0.1 g/mL solution of zinc acetate dihydrate and methanol. The AZO seed layer precursor was made by adding $AlCl_3 \cdot 6H_2O$ to the ZnO seed layer precursor to obtain Al/Zn molar ratios of 1% and 2%. The precursor solutions were filtered through a 0.22 μm pore diameter filter before spin-coating to remove any undissolved solids.

### 3.2.2 Hybrid solar cell fabrication and characterization

The hybrid solar cells were fabricated by first spin-coating an active layer of poly(3-hexylthiophene) (P3HT) and phenyl-C61-butyric acid methyl ester (PCBM) on the electrodeposited AZO film. The solution was prepared with a 30 mg/mL of 1:1 P3HT:PCBM in 1:1 chlorobenzene:trichlorobenzene. The spin-coated samples were kept in a container purged with nitrogen and allowed to dry slowly. After the active layer had dried, a molybdenum oxide ($MoO_3$) film as hole transport layer and a gold film as high work-function electrode were subsequently deposited by vacuum deposition through a shadow mask.

## 3.3 Electrochemical deposition of Al-doped ZnO

### 3.3.1 Al-doped ZnO film nanostructure

Figure 3.1 shows the top-view SEM images of AZO films electrodeposited on ZnO-seeded ITO substrates, (a), (b), and (c), and on AZO-seeded ITO substrates, (d), (e), and (f), in electrolyte solutions at 5.0%, 2.5%, and 0.5% Al/Zn ratios, respectively.

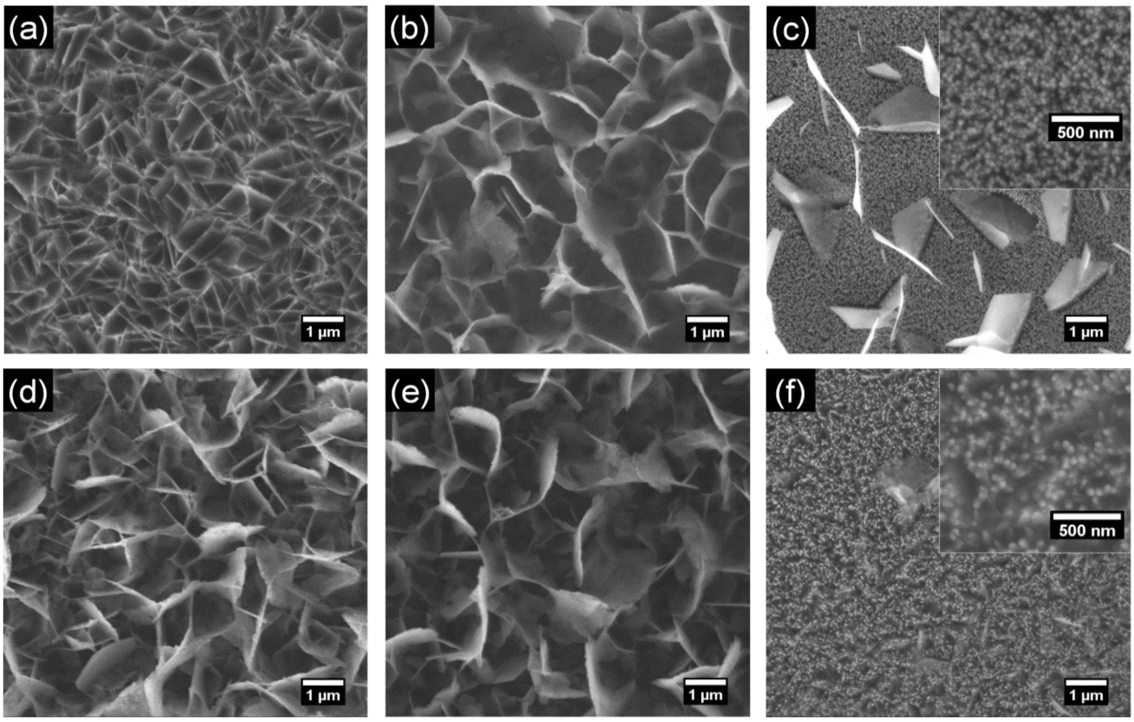

Figure 3.1 SEM images of electrodeposited AZO films on undoped ZnO-seeded ITO substrates at Al/Zn ratios of 5.0%(a), 2.5%(b), and 0.5%(c) and on AZO-seeded ITO substrates at Al/Zn ratios of 5.0%(d), 2.5%(e), and 0.5%(f). Insets show enlarged images of nanorod structures.

Interconnected micron-sized flakes that form a honeycomb-like structure are seen in Figure 3.1 (a), (b), and (d), (e), corresponding to Al/Zn ratios of 5.0% and 2.5%, respectively. This morphology has been previously reported for electrodeposited AZO in nitrate electrolyte solutions [15, 20]. In comparison, nanorod structures with isolated hexagonal flakes are seen in Figure 3.1 (c) and (f) for Al/Zn ratio of 0.5%. Because the hexagonal flakes in Figure 3.1 (f) are thinner, they look transparent and are harder to see. The nanorods are about 40-60 nm in diameter and mainly grow in the same direction perpendicular to the substrate. The flakes decrease in number and are less interconnected at lower Al/Zn ratios regardless of the seed layer.

Chen et al. [14] deposited AZO nanorods on ZnO-seeded fluorine-doped tin oxide (FTO) substrates by electrochemical deposition using a nitrate-based electrolyte. In their experiment, the Al/Zn ratio is higher at about 2.1% and 3.3%. The structures are similar to nanorods and are disordered, growing in different directions. In comparison, the nanorods grown in this study, using a chloride electrolyte, have a high degree of orientation and have a regular diameter size.

### 3.3.2 Composition analysis

Energy dispersive X-ray (EDX) spectroscopy was performed on the samples grown on ZnO-seeded ITO substrates to estimate the Al content in the electrodeposited AZO films. The results of the EDX measurements are displayed in Table 1. Molar Al contents in the AZO films increased with increasing Al/Zn ratios in the electrolyte solution. Molar Al contents in the AZO films at 2.5% and 5.0% Al/Zn ratios are much higher than expected from the ratio in the electrolyte solution. Previous work suggests that some of the aluminum detected in the films could exist as amorphous alumina or AlO(OH) [20].

EDX spectroscopy was also able to detect chlorine in all of the samples. Even though the $Cl^-$ ion is not a participant in the ZnO electrodeposition process, chlorine incorporation in ZnO films was previously reported for electrochemical deposition of ZnO in a chloride medium [16, 17, 21].

Table 1. Al/Zn ratio present in the electrolyte and molar Al content in the AZO grown on undoped ZnO-seeded ITO substrates as measured by EDX.

| Al/Zn molar ratio in electrolyte (%) | Molar Al content in AZO film [a] |
|---|---|
| 0.5 | 0.01 |
| 2.5 | 0.10 |
| 5.0 | 0.36 |

[a] Defined as the ratio [Al]/[Al+Zn]

The reactions involved in ZnO electrodeposition are described in Chapter 1. The reaction begins with the reduction of molecular oxygen to form hydroxide ions. The zinc ions and hydroxide ions then react and undergo dehydration leading to the precipitation of ZnO on the electrode [22]. Because the electrolyte solution in this experiment also contains aluminum ions, the hydroxide ion may also yield the corresponding oxide during deposition (Eq. 3.1) [14].

$$Al^{3+} + 3OH^{-} \rightarrow Al(OH)_3 \rightarrow Al_2O_3 + H_2O \qquad (3.1)$$

Considering that aluminum hydroxide formation is thermodynamically more favorable than zinc hydroxide formation during electrochemical deposition [23], it is probable that the deposited film may contain aluminum oxide phases. In particular, the high Al/Zn ratios in the 2.5% and 5.0% samples may be attributed to the formation of the aluminum oxide phases.

### 3.3.3 Optical properties

Because light first passes through the electron transport layers before reaching the active layer, high optical transmittance is an important quality for AZO films in inverted hybrid solar cells. The optical transmittance of the electrodeposited AZO are measured by UV-Vis spectroscopy and the optical transmittance curves are shown in Figure 3.3. Samples grown in the 0.5% solution had the highest transmittance, over 90% in the visible region. The optical transmittances of the 5.0% samples are around 80% in the visible region. The 2.5% samples had the lowest optical transmittance.

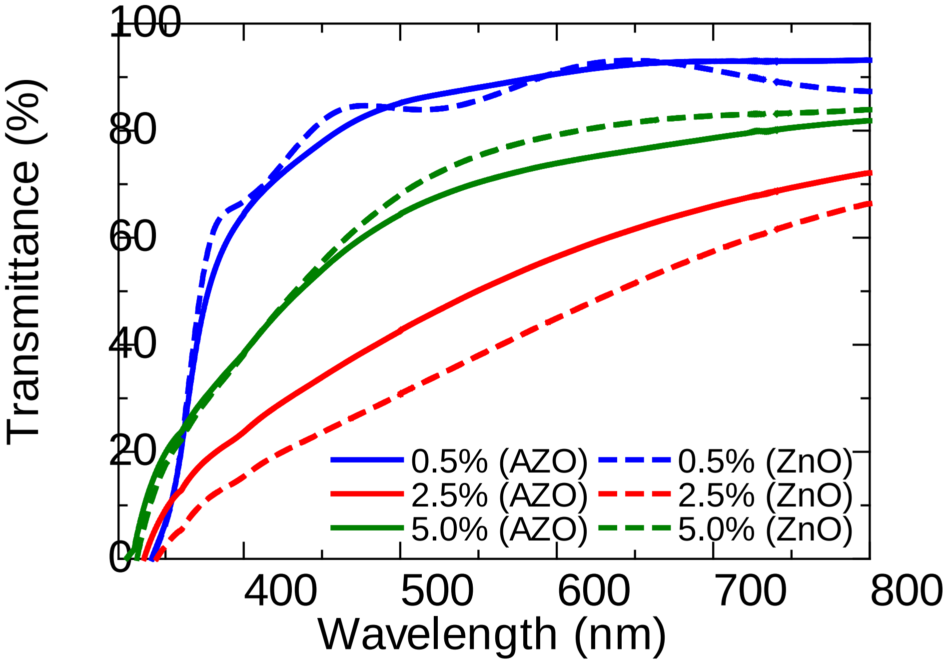

Figure 3.2 Optical transmission spectra of the electrodeposited AZO films on ZnO- (dashed lines) and AZO-seeded (solid lines) ITO substrates in electrolyte solutions with 5.0% (green), 2.5% (red), and 0.5% (blue) Al/Zn ratios.

While many factors contribute to the optical transmittance of materials, the low optical transmittance of the 2.5% and 5.0% samples can be mainly attributed to light scattering by the micron-sized flakes (Figure 3.1 (a), (b), (d), and (e)). The 2.5% samples have the lowest optical transmittance; it can be attributed to the larger size of the flakes. The SEM images in Figure 3.1 show the flake sizes of the 2.5% sample are slightly larger than the 5.0% samples, most notably in Figure 3.1 (a) and (b).

Lower optical transmittance in the shorter wavelength region of the 5.0% and 2.5% samples are consistent with Rayleigh scattering behavior where scattering of blue light is stronger than red light. On the other hand, the smaller size of the nanorods compared to the flakes and their ordered alignment contribute to the high optical transmittance of the 0.5% samples [24, 25].

Table 2. Estimated band gap of the AZO samples

| Seed layer | Al/Zn ratio (%) | Estimated band gap (eV) |
|---|---|---|
| ZnO | 0.5 | 3.60 |
|  | 2.5 | 3.58 |
|  | 5.0 | 3.71 |
| AZO | 0.5 | 3.61 |
|  | 2.5 | 3.67 |
|  | 5.0 | 3.78 |

Band gap energies estimated by applying Tauc plot analysis to the UV-Vis spectra [26] are presented in Table 2. The estimated band gap energies of all the AZO samples are larger than 3.3 eV – the literature value of the optical bandgap of intrinsic ZnO. In general, the table shows that the band gap widens with increasing Al/Zn ratio in the electrolyte and accordingly, with increasing Al content in the AZO films. This effect, called the Burstein-Moss shift, has been observed for AZO thin films fabricated by various methods [27, 28, 29]. The same effect was also observed for ZnO deposited from chloride-containing electrolytes [16, 17, 30].

### 3.3.4 Hybrid solar cell characteristics

The best current density-voltage characteristics of the devices fabricated from the electrodeposited AZO samples are shown in Figure 3.5. Device parameters deduced from the *J-V* characteristics are presented in Table 3. For both the ZnO- and AZO-seeded samples, the $J_{SC}$, $V_{OC}$, *FF*, and *PCE* improve as the Al/Zn ratio decreases.

Table 3. Summary of device parameters, average and standard deviation in brackets.

| Seed layer | Al/Zn ratio (%) | $J_{SC}$ (mA/cm$^2$) | $V_{OC}$ (V) | *FF* (%) | *PCE* (%) |
|---|---|---|---|---|---|
| ZnO | 0.5 | 8.94<br>[7.99±1.12] | 0.440<br>[0.427±0.023] | 43.4<br>[43.5±1.62] | 1.71<br>[1.49±0.247] |
|  | 2.5 | 3.63<br>[1.94±1.47] | 0.420<br>[0.267±0.133] | 42.5<br>[32.2±9.12] | 0.648<br>[0.253±0.342] |
|  | 5 | 1.65<br>[1.68±0.076] | 0.180<br>[0.167±0.023] | 27.4<br>[26.8±0.623] | 0.081<br>[0.075±0.009] |
| AZO | 0.5 | 7.27<br>[5.91±1.97] | 0.380<br>[0.313±0.070] | 40.3<br>[41.5±1.23] | 1.11<br>[0.797±0.380] |
|  | 2.5 | 2.50<br>[1.44±1.05] | 0.340<br>[0.167±0.151] | 35.8<br>[27.6±7.8] | 0.305<br>[0.116±0.164] |
|  | 5 | 1.11<br>[0.982±0.175] | 0.040<br>[0.030±0.014] | 19.9<br>[24.8±6.90] | 0.009<br>[0.007±0.003] |

The highest *PCE*, 1.71%, is obtained from the 0.5% samples with the ZnO seed layer followed by 1.11% from the 0.5% samples with the AZO seed layers. Both AZO films had high optical transmittances and their estimated band gaps were similar. However, while both films had nanorod morphologies, the nanorods grown on the ZnO seed layer have smaller diameters and are greater in number compared to the nanorods grown on the AZO seed layer, as seen in the insets of Figure 3.1 (c) and (d). The higher $J_{SC}$ can be attributed to the larger interfacial area that is available. This, in turn, results to a higher PCE.

For both ZnO-seeded and AZO-seeded samples, enhancement of $J_{SC}$ from 5.0% to 2.5% is smaller in comparison to the larger improvement from 2.5% to 0.5%. This can be attributed to the higher optical transmittance and the presence of the nanorods in the 0.5% samples. The larger interfacial area between the nanorod surface and the active layer increases carrier extraction rate and carrier collection probability [31].

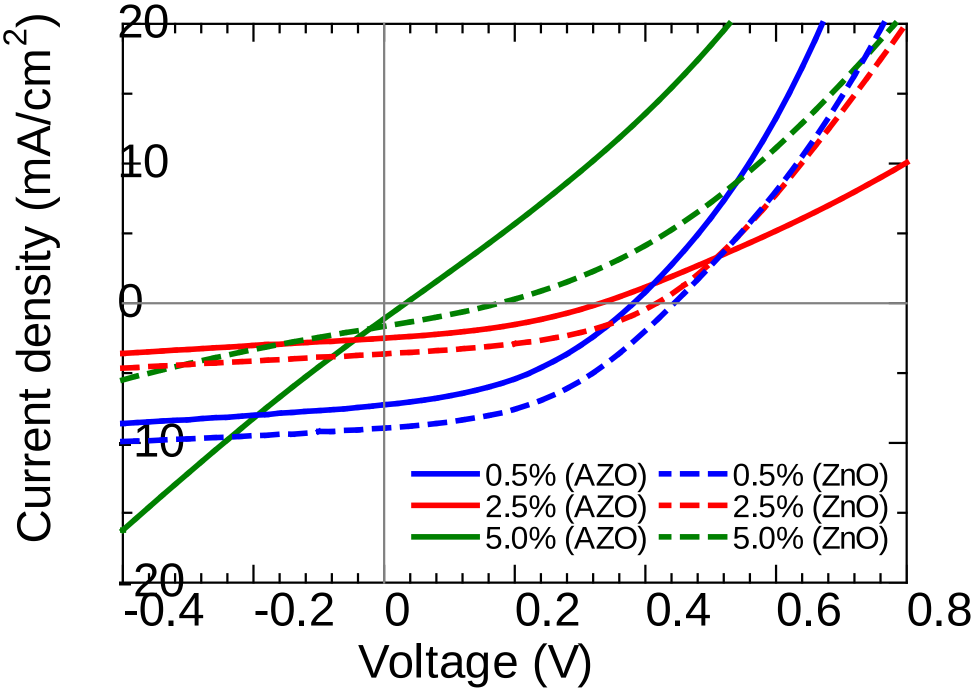

Figure 3.3 J-V characteristics under illumination for the electrodeposited AZO films on ZnO- (dashed lines) and AZO-seeded (solid lines) ITO substrates in electrolyte solutions with 5.0% (green), 2.5% (red), and 0.5% (blue) Al/Zn ratios.

On the other hand, $V_{OC}$ enhancement is larger from 5.0% to 2.5%, that is, the $V_{OC}$ of the 0.5% and the 2.5% samples are closer in value even though the morphologies are different. One reason could be a higher cell resistance in the device resulting from high Al dopant concentration [12]. Although $V_{OC}$ is predicted to increase at higher doping concentration due to the widening of the band gap attributed to the Burstein-Moss effect, the higher dopant concentration in the electrolyte solution may have led to the formation of insulating phases of aluminum oxide which reduces conductivity. The high molar Al content of 0.36 for the 5.0% sample (Table 1) may indicate the presence of these phases in the sample.

## 3.4 Growth of hexagonal flakes

### 3.4.1 Effect of decreasing KCl concentration

In the electrochemical deposition of aluminum-doped zinc oxide, the growth of micron-sized hexagonal flakes is problematic. As described in Chapter 2, decreasing the concentration of the supporting electrolyte, KCl, is an effective way to inhibit the growth of hexagonal flakes. Note, however, that the deposited AZO samples discussed in Section 3.3 were grown at the lower KCl concentration of 0.05M.

This subsection discusses the effect of further cutting the concentration of KCl in half to 0.025 M on the growth of hexagonal flakes.

Al-doped ZnO films were deposited on ZnO-seeded ITO substrates. The specific conditions for electrochemical deposition of these set of samples are described. Electrochemical deposition of AZO on bare ITO substrates were carried out on an RDE setup with a Zn wire counter electrode and saturated calomel electrode (SCE) reference. Deposition was performed for 300 s at RDE rotation speed of 300 rpm and at a fixed potential of −1.0 V versus SCE with a Hokuto Denko HSV-110 potentiostat. The electrolyte contained 3 mM $ZnCl_2$ and $AlCl_3 \cdot 6H_2O$ was added to obtain solutions with Al/Zn molar ratios of 0.5%. The concentration of KCl is 0.025M and 0.05 M KCl. The electrolyte solution was kept at 70 °C during deposition. The solution was bubbled with $O_2$ through a glass frit prior to and during the deposition process.

An undoped ZnO film was also deposited on ZnO-seeded ITO substrate. Deposition was performed for 300 s at RDE rotation speed of 300 rpm and at a fixed potential of −1.0 V versus SCE. The electrolyte contained 3 mM $ZnCl_2$ and 0.05 M KCl.

Figure 3.6 shows the SEM images of the deposited AZO films in (a) 0.025 M KCl and in (b) 0.05 M KCl. Both conditions yield similarly nanostructured film composed of nanorods and isolated hexagonal flakes. The width of the hexagonal flakes are about 2 μm.

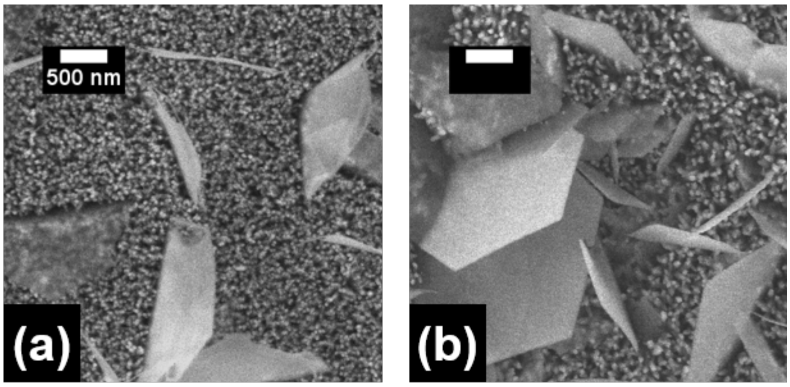

Figure 3.4 SEM images of AZO films grown in electrolytes containing Al/Zn ratio of 0.5% and with KCl concentration of (a) 0.025 M and (b) 0.05 M.

In the case of growing Al-doped ZnO films, decreasing the KCl concentration in the electrolyte did not inhibit the growth of hexagonal flakes. Even after decreasing the KCl concentration down to 0.025 M, hexagonal flakes still grew. There are, however, fewer flakes in the AZO film grown in electrolyte with 0.025 M KCl than there are in the AZO film grown in 0.05 M KCl. The sizes of the hexagonal flakes are similar.

In Chapter 2, it was discussed that the $Cl^-$ ions in the solution preferentially adsorbed on the (0001) plane stabilize this plane and promote the growth of hexagonal flakes. Decreasing the KCl concentration from 0.1 M to 0.05 M was demonstrated to be an effective strategy to inhibit the growth of hexagonal flakes. Because this strategy did not fully inhibit the growth of hexagonal flakes in the AZO system, it indicates that the growth of hexagonal flakes may be governed by a different mechanism that includes the $Al^{3+}$ ion.

### 3.4.2 Hybrid solar cell characteristics

Inverted hybrid solar cells were fabricated from the deposited films and were characterized. Figure 3.7 shows the current density-voltage plot of the devices in light condition. The highest PCE of 2.32% is obtained from the undoped ZnO sample. The AZO samples, grown in different KCl concentrations, both had the same *PCE*s of 1.14%.

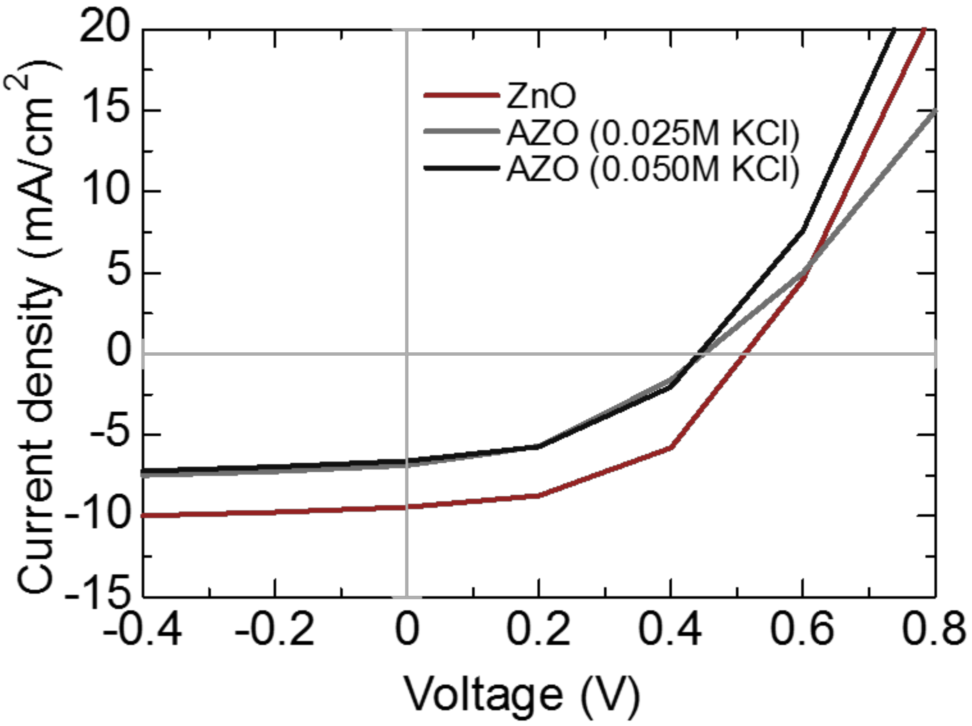

Figure 3.5 Current density-voltage characteristic for undoped ZnO and AZO samples

The $V_{OC}$, $J_{SC}$, *FF*, and *PCE* of both AZO samples are comparable owing to the similarity in microstructure. The performance of the undoped ZnO sample is better overall, with a PCE of 2.32%. The microstructures of the ZnO and AZO samples, though all containing nanorod arrays, are different due to the presence of the hexagonal flakes on the AZO samples. Because the flakes cannot be fully covered by the organic layer, it may act as short circuit paths where recombination occurs causing a drop in *Voc* and *Jsc*.

Table 4 Summary of device parameters, average and standard deviation in brackets.

| | *Voc* (V) | *Jsc* (mA/cm$^2$) | *FF* (%) | *PCE* (%) |
|---|---|---|---|---|
| ZnO | 0.51<br>[0.51±0.005] | 9.46<br>[9.13±0.40] | 0.48<br>[0.49±0.03] | 2.32<br>[2.28±0.06] |
| AZO (0.05M KCl) | 0.45<br>[0.39±0.07] | 6.87<br>[6.13±0.81] | 0.37<br>[0.37±0.015] | 1.14<br>[0.90±0.28] |
| AZO (0.025M KCl) | 0.44<br>[0.43±0.02] | 6.61<br>[6.19±0.60] | 0.39<br>[0.40±0.01] | 1.14<br>[1.05±0.12] |

The external quantum efficiencies (*EQE*) of the devices are shown in Figure 3.7. The external quantum efficiency is defined as the ratio of the number of charge carriers collected by the device to the number of incident photons. The EQE for the undoped ZnO and AZO (0.025M KCl) samples shows maximums at 550 nm of 25% and 20%, respectively.

The lower *EQE* for the AZO sample can be attributed to the shunt paths formed by the presence of the micron-sized hexagonal flakes. A change in transport properties will affect the EQE of devices across the entire wavelength. However, the *EQE* of the AZO and undoped ZnO samples from 420 nm and below are similar. This could likely indicate an increase in the *EQE* of the AZO sample due to an optical effect, in particular, band gap widening.

Due to the band gap widening in the AZO films, the transmittance edge shifts to a lower wavelength allowing more light in the shorter wavelengths to be absorbed in the active layer. As a result, more charge carriers could be collected at shorter wavelengths and compensates for the overall decrease of EQE caused by the presence of the micron-sized hexagonal flakes.

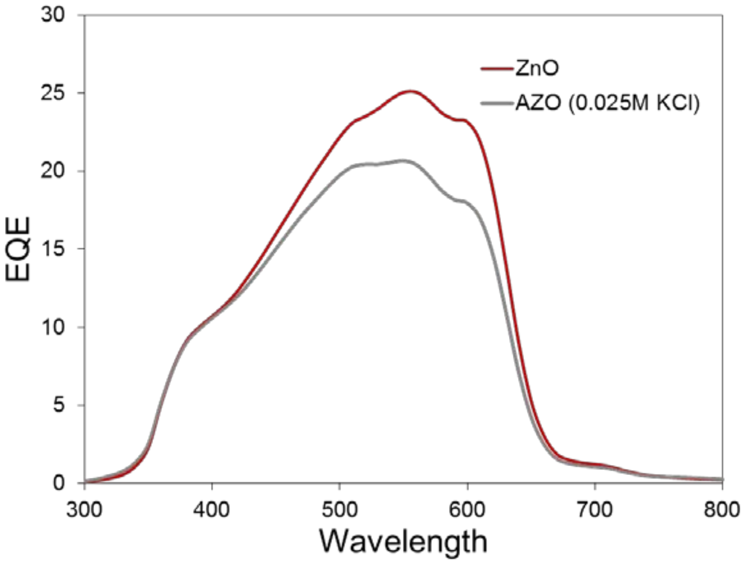

Figure 3.6 External quantum efficiencies of the undoped ZnO and AZO samples

## 3.5 Morphological evolution of hexagonal flakes

To understand the evolution of the morphology of the film, i.e. how the hexagonal flakes grow, aluminum-doped ZnO films are grown for deposition times 12 s, 40 s, 120 s, and 300 s. By ending the growth process at different stages during film formation, the evolution of the nanostructure can be observed. The electrolyte used for these set of samples has Al/Zn ratio of 2.5%. The SEM images of the films in Figure 3.8 show the progression of film formation.

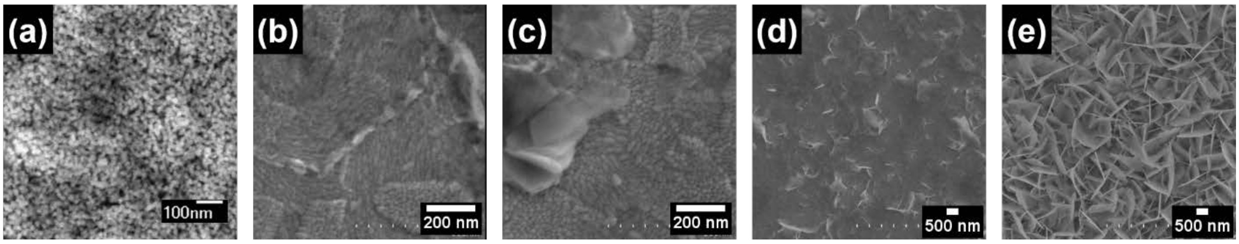

Figure 3.7 Morphologies of the film (a) before deposition and after different deposition times: (b) 12 s, (c) 40 s, (d) 120 s, and (e) 300 s.

The first image in the series is that of the ZnO seed layer. It is a film made up of nanocrystals, about 30 nm in diameter, which fully covers the ITO. The next images, Figure 3.8(b) and (c), however, clearly shows the ITO surface. This indicates that the ZnO seed layer is removed in the early stages of deposition, even as soon as 12 s from starting.

Hexagonal flakes then proceed to grow, as seen in Figure 3.8 (c), (d), and (e). With a deposition time of 120 s, a film entirely covering the ITO surface is obtained. A few flakes growing perpendicularly with respect to the substrate can also be seen. The growth of hexagonal flakes continue; with a deposition time of 300 s, a film made up of interconnected hexagonal flakes is grown.

This series of images show that the removal of the ZnO seed layer is a contributing factor to the growth of hexagonal flakes. In Chapter 2, it was shown that the ZnO seed layer was conducive for high density nucleation. Without the nanocrystals in the seed layer serving as nucleation sites, nanorods were not developed and hexagonal flakes are grown instead. This could explain why decreasing the KCl concentration in the electrolyte for aluminum-doped ZnO still resulted in the growth of hexagonal flakes, whereas in the electrochemical deposition of undoped ZnO, the decrease in concentration of KCl in the electrolyte inhibited the growth of hexagonal flakes.

The removal of the ZnO seed layer can be explained by the effect of adding $AlCl_3 \cdot 6H_2O$ on the pH of the electrolyte. Anhydrous aluminum chloride is considered as a strong Lewis acid that is used as a catalyst in many industrial processes. Its hydrated counterpart, $AlCl_3 \cdot 6H_2O$, on the other hand, has different mechanics and utilities. Although not as strong an acid as anhydrous aluminum chloride, $AlCl_3 \cdot 6H_2O$ and its aqueous solution are acidic due to the ability of the hydrated cation $[Al(H_2O)_6]^{+3}$ to act as a proton donor [32].

The addition of $AlCl_3 \cdot 6H_2O$ to the electrolyte decreases the pH of the solution. Consulting the Pourbaix diagram [33] of zinc in aqueous solution in Figure 3.9, we see that the decrease in pH drives the system towards the region where $Zn^{2+}$ is the thermodynamically stable species. As $Zn^{2+}$ ions are soluble in water, the ZnO film thereby undergoes corrosion.

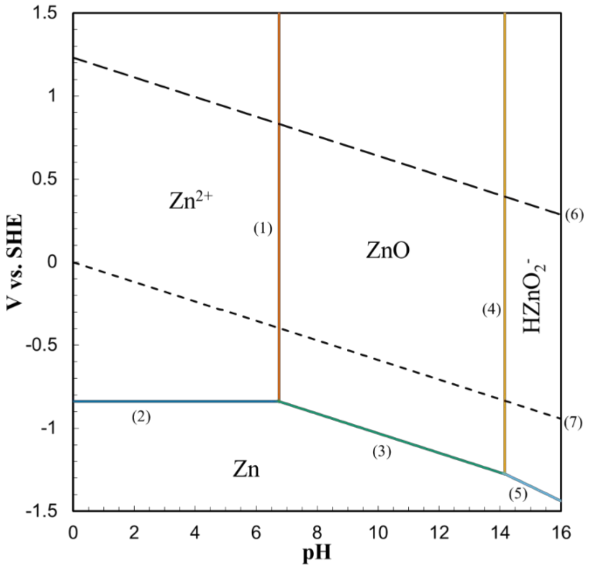

Figure 3.8 Pourbaix diagram for Zn in water (3 mM). The lines represent equilibrium between (1) $Zn^{2+}$ and ZnO, (2) $Zn^{2+}$ and Zn, (3) ZnO and Zn, (4) ZnO and $HZnO^-_2$, (5) $HZnO^-_2$ and Zn, (6) $O_2$ and $H_2O$, and (7) $H^+$ and $H_2$.

Although ZnO seed layer undergoes corrosion in the early stages of deposition, the series of images in Figure 3.8 shows that electrodeposition of ZnO film proceeds eventually. This means that the system moves towards the region where ZnO is thermodynamically stable after the seed layer is dissolved. As the concentration of zinc in the system increases, due to the corrosion of the ZnO seed layer and the zinc wire counter electrode, the system moves towards the region where ZnO is stable. At the same time, the reduction of water, which proceeds to increase the local concentration of $OH^-$ ions near the electrode, also drives the system towards the same region where ZnO is stable. Deposition of ZnO on the working electrode then becomes possible.

### 3.5.1 Addition of buffer layer

The result of the previous experiment showed that the ZnO seed layer undergoes corrosion at the start of deposition due to the acidic nature of the dopant source, $AlCl_3 \cdot 6H_2O$. In order to prevent directly depositing AZO on bare ITO substrate, a buffer layer of ZnO nanorods is deposited prior to AZO deposition.

The ZnO buffer layer is deposited using the same method described in Chapter 2, with a KCl concentration of 0.025 M. The deposition time is 150 s. Without stopping the application of potential (-1.0V), a solution containing the dopant $AlCl_3 \cdot 6H_2O$ is immediately added to the electrolyte (Al/Zn ration 2.5%). The deposition proceeds for another 150 s. The total deposition time is 300 s.

With this method, a ZnO nanorod layer is deposited first on seeded ITO substrates. This layer will act as a buffer such that AZO deposition on a bare ITO substrate is prevented. Upon the addition of the dopant to the electrolyte, AZO deposition then occurs on top of the ZnO nanorod layer.

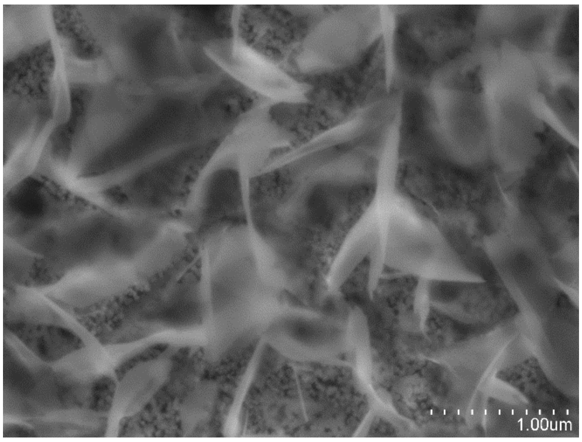

Figure 3.9 SEM image of AZO film deposited on ZnO nanorod buffer layer.

The SEM image in Figure 3.10 shows the nanostructure of the film deposited with this method. The film is composed highly oriented nanorods with interconnected hexagonal flakes. Even with a ZnO nanorod buffer layer to prevent AZO deposition on bare ITO substrate, the growth of hexagonal flakes still persists. The result of these experiments suggest that the $Al^{3+}$ ion plays a larger role in the growth mechanism of hexagonal flakes during AZO electrochemical deposition. Just as $Cl^-$ ions are preferentially adsorbed on the positive polar plane of ZnO, the $Al^{3+}$ ions may also be preferentially adsorbed on the other side of the plane with the negative polarity. As a result, two species in the aqueous solution, $Al^{3+}$ ions and $Cl^-$ ions, stabilize the ZnO (0001) plane, thus favoring the growth of hexagonal flakes.

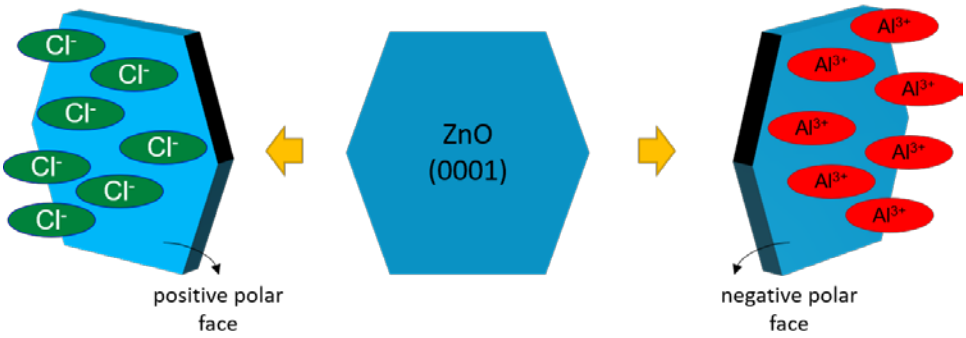

Figure 3.10 Illustration of the preferential adsorption of $Al^{3+}$ ions and $Cl^-$ ions on the negative and positive polar faces of ZnO, respectively.

## 3.6 Further characterization

XRD and XPS analysis are performed on the samples to better understand the nanostructure and composition of the films.

The following cross-section SEM images confirm the highly ordered nanorod structure of the sample. Both images are from the same AZO film grown in 0.05 M KCl with Al/Zn ratio of 0.5%. In Figure 3.12, the sample cross-section was prepared by focused ion beam. A tungsten layer was deposited on top of the gold layer, this is labeled by W in the image.

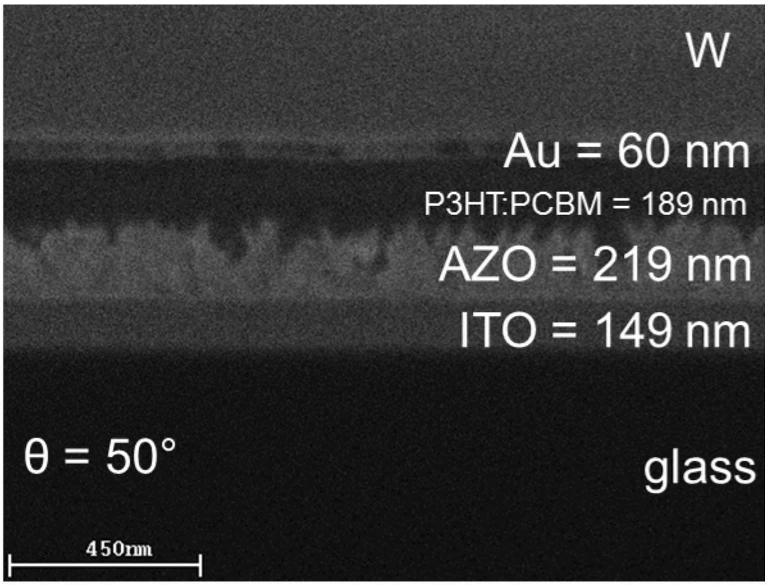

Figure 3.11 Cross-section SEM image of the AZO film (0.05M KCl) prepared by FIB.

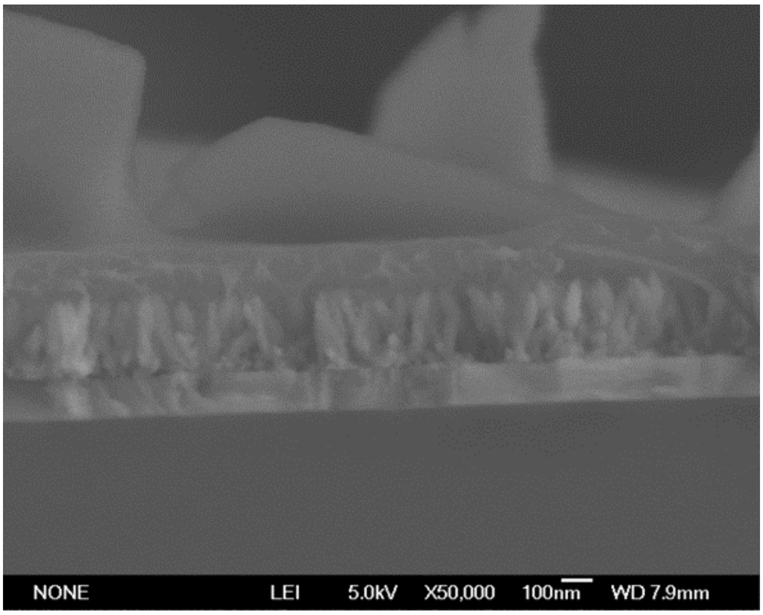

Figure 3.12 Cross-section SEM image of the AZO film (0.05M KCl) prepared by cleaving.

Preparing the cross-section by FIB creates a very clean cut without delamination of the layers. This way, the thickness of the AZO film, the active layer, and the Au electrode can be measured precisely. The sample was etched at an angle of $50^o$. This was taken into consideration when measuring the thickness of the layers. The thickness of the ITO is similar to previous measurements.  The AZO nanorod array was measured to be around 220 nm in thickness. The individual single crystal nanorods are difficult to distinguish. The structure of the active layer, however, is easy to see. It is usually difficult to observe due to delamination sometimes arising from preparing the cross-section by cleaving. Here, the complete coverage of the nanorod array by the active layer can be seen.

In Figure 3.13, the sample cross section was prepared by cleaving. The glass is scored by diamond and pressure is applied. A thin layer of Os is deposited by plasma deposition to diminish the effect of charging when imaging with the SEM. In this image, the vertical orientation of the nanorods is seen. Individual nanorod single crystals are also easy to distinguish. The active layer can be seen to be fully covering the nanorod array and infiltrating the spaces in between the nanorods. This image also shows the nanorods and hexagonal flakes together. The difference in sizes can be considered.  The size of the flakes exceed the thickness of the active layer and as a result create protrusions in the device.

The XRD spectra shown in Figure 3.14 was obtained by symmetrical reflection measurement. The symmetrical reflection measurement provides crystallographic information perpendicular to the sample surface (or the stacking) direction. It is particularly suited to studying films with a preferred orientation [34]. The strong peak corresponds to ZnO (0001). The two smaller peaks correspond to the ITO substrate – ITO (400) and ITO (222). This indicates that the ZnO and AZO films have a strong c-axis texture, i.e. preferred orientation along the c-axis.

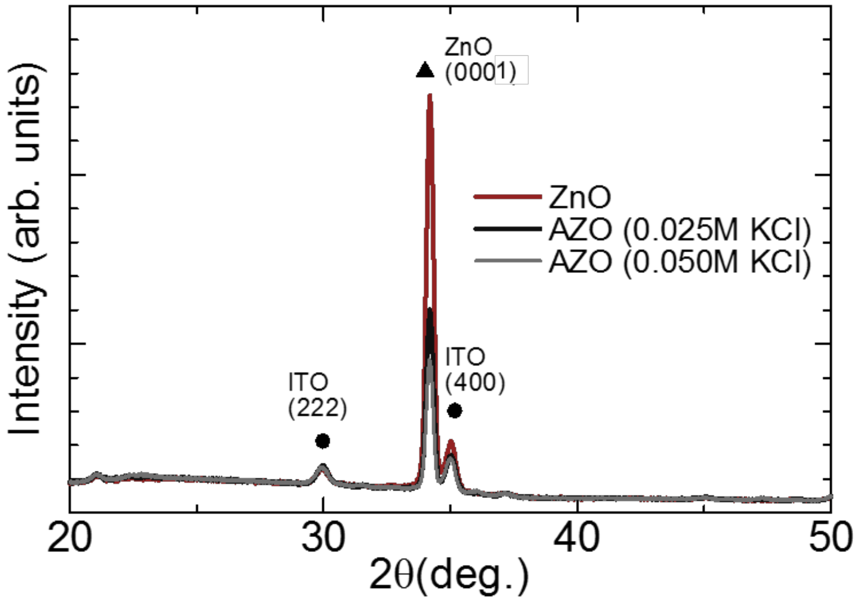

Figure 3.13 Symmetrical reflection XRD spectra of undoped ZnO and of AZO films deposited in 0.025 M and 0.05 M KCl.

The AZO and ZnO samples were characterized by XPS to study the composition and doping mechanism. The binding energy of Al2p ranges from 72.6 to 75.6 eV. The XPS spectra in Figure 3.15 shows Al2p peaks in the AZO samples; no Al2p peaks are observable for the undoped ZnO. The data confirms the incorporation of Al into the ZnO matrix.

The Al2p spectra of AZO film is shown in Figure 3.16 (a). The spectra is fitted to the binding energies of metallic aluminum (72.2 eV, blue) and $Al_2O_3$ (74.6 eV, orange). It can be seen that the main component of the spectra is coming from the $Al_2O_3$ peak with a small contribution from the metallic aluminum peak, meaning that Al exists in the ZnO matrix predominantly in the $Al^{3+}$ oxidation state. This indicates that Al atoms substitute of Zn atoms in AZO films which could act as Al donors.

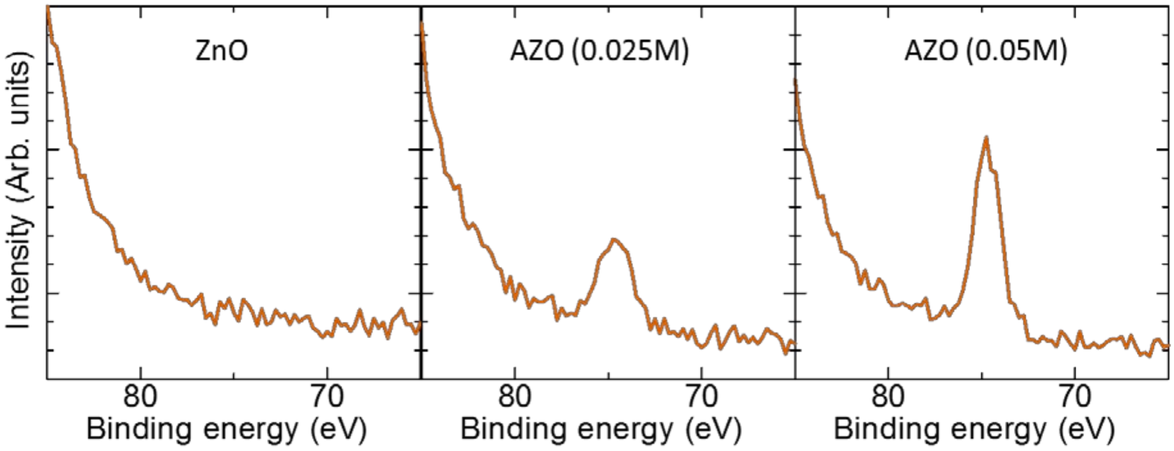

Figure 3.14 XPS spectra of undoped ZnO and AZO samples showing Al2p peaks.

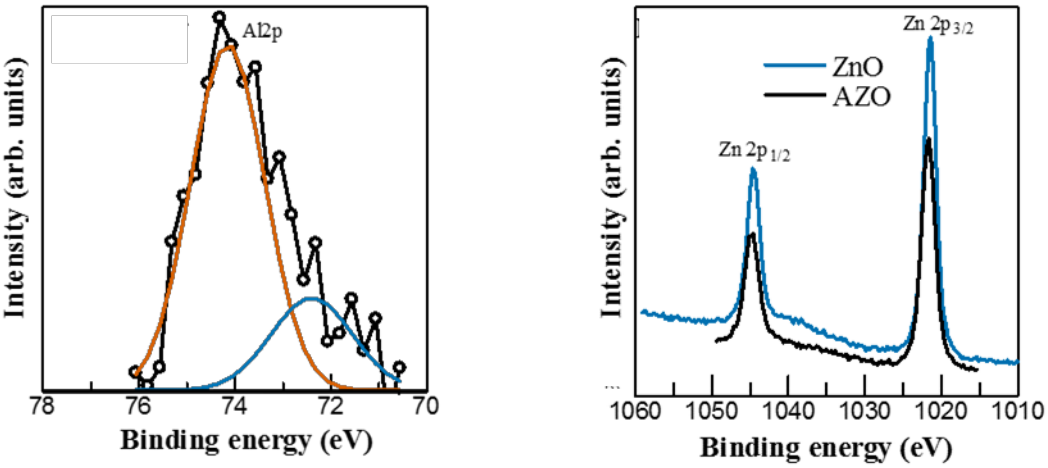

**(a)**

**(b)**

Figure 3.15 XPS Spectra: (a) Al2p spectra of AZO film, blue line corresponds to the 72.2 eV binding energy of metallic aluminum and orange line corresponds to the 74.6 eV binding energy of $Al_2O_3$; (b) Zn2p spectra of AZO and undoped ZnO.

The Zn2p spectra of AZO and ZnO films are compared in Figure 3.16 (b). The Zn2p doublet peaks of the Al-doped ZnO samples are shifted by about 0.2 eV to higher binding energies. A shift to higher binding energies indicate higher coulombic interaction between the photoemitted electron and the ion core brought about by the Al dopant. This further confirms the incorporation of Al into the ZnO matrix.

## 3.7 Summary

Electrodeposition of Al-doped thin films on ITO substrates from a chloride electrolyte solution was demonstrated. The growth of ordered nanorods, about 40-60 nm in diameter, was grown from the electrolyte solution with an Al/Zn ratio of 0.5%.

To the best of our knowledge, this study was the first to demonstrate the growth of ordered AZO nanorods by electrodeposition from a chloride electrolyte.

Micron-sized flakes present in all of the samples became less interconnected with decreasing Al/Zn ratios. Molar Al content in the AZO films detected by EDX increased with increasing Al/Zn ratios in the electrolyte solution. For the 5.0% sample, the Al/Zn molar ratio was higher than the expected ratio from the electrolyte solution, which suggests the presence of aluminum oxide or aluminum hydroxide phases in the film.

High optical transmittances over 90% were measured from the 0.5% samples. Band gap energies estimated from Tauc plot analysis increased at higher Al dopant content, showing the Burstein-Moss effect. Hybrid solar cells were fabricated from the electrodeposited AZO and the highest PCE, 1.71%, was obtained from the 0.5% sample with the ZnO seed layer.

In an effort to inhibit the growth of hexagonal flakes, the KCl concentration in the electrolyte was further decreased to 0.025 M. The SEM analysis showed a minimal decrease in the number and size of flakes. Unlike in the electrodeposition of undoped ZnO, decreasing the KCl concentration does not inhibit the growth of hexagonal flakes.

The evolution of the morphology of the hexagonal flakes was observed. It was revealed that the ZnO seed layer underwent corrosion due to the acidic nature of the Al dopant. As a result, AZO deposition occurred on bare ITO substrates – a condition not favorable to the growth of ordered nanorod arrays, as discussed in Chapter 2.

Yet, even with a buffer layer of ZnO nanorods to prevent AZO deposition on bare ITO, the growth of hexagonal flakes still persisted. This suggests that the $Al^{3+}$ ion may play a bigger role in the growth of hexagonal flakes.

# References

[1] K. D. G. I. Jayawardena, L. J. Rozanksi, C. A. Mills, M. J. Beliatis, N. A. Nismy and S. R. P. Silva , *Nanoscale,* vol. 5, p. 8411, 2013.

[2] M. Wright and A. Uddin, *Solar Energ. Mater. and Solar Cells*, vol. 107, p. 87, 2012.

[3] Z. He, C. Zhong, S. Su, M. Xu, H. Wu and Y. Cao, *Nature Photon.* , vol. 6, p. 591, 2012.

[4] Z. Yin, S. C. Chen and Q. Zheng, Organic and Hybrid Solar Cells, H. Huang and J. Huang, Eds., Springer International Publishing, 2014, p. 215.

[5] D. Olson, J. Piris, R. Collins, S. Shaheen and D. Ginley, *Thin Solid Films,* vol. 496, p. 26, 2006.

[6] X. Yu, X. Yu, J. Zhang, Z. Hu, G. Zhao and Y. Zhao, *Solar Energ. Mater. and Solar Cells,* vol. 121, p. 28, 2014.

[7] X. Jiang, F. Wong, M. Fung and S. Lee, *Appl. Phys. Lett.,* vol. 83, p. 1875, 2003.

[8] W. Wang, D. Han, J. Cai, Y. Geng, L. Wang, L. Wang, Y. Tian, X. Zhang, Y. Wang and S. Zhang, *Jpn. J. Appl. Phys.,* vol. 52, p. 04CF10, 2013.

[9] M. Suchea, S. Christoulakis, N. Katsarakis, T. Kitsipoulos and G. Kiriakidis, *Thin Solid Films,* vol. 515, p. 6562, 2007.

[10] Y. Ammaih, A. Lfakir, B. Hartitit, A. Riyadh, P. Thevenin and M. Siadat, *Opt. Quant. Electron.,* vol. 46, p. 229, 2014.

[11] A. Aprilia, P. Wulandari, V. Suendo, Herman, R. Hidayat, A. Fujii and M. Ozaki, *Solar Energ. Mater. and Solar Cells,* vol. 111, p. 181, 2013.

[12] T. Stubhan, H. Oh, L. Pinna, J. Krantz, I. Litzov and C. Brabec, *Org. Electron.,* vol. 12, p. 1539, 2011.

[13] R. Tao, T. Tomita, R. A. Wong and K. Waki, *J. Power Sources*, vol. 214, p. 159, 2012.

[14] J. Chen, J. Chen, D. Chen, Y. Zhou, W. Li, Y. Ren and L. Hu, *Mater. Lett.,* vol. 117, p. 162, 2014.

[15] A. C. Aragones, A. Palacios-Padros, F. Caballero-Briones and F. Sanz*, Electrochi. Acta,* vol. 109, p. 117, 2013.

[16] T. Pauporte, E. Jouanno, F. Pelle, B. Viana and P. Aschehoug, *J. Phys. Chem. C.,* vol. 113, p. 10422, 2009.

[17] C. Richter, M. Beu and D. Schlettwein, *Phys. Chem. Chem. Phys.,* vol. 17, p. 1883, 2015.

[18] S. P. Anthony, J. I. Lee and J. K. Kim, "Tuning optical bandgap of vertically aligned ZnO nanowire arrays grown by homoepitaxial electrodeposition," *Applied Physics Letters,* vol. 90, p. 103107, 2007.

[19] M. Ohyama, H. Kozuka and T. Yoko, *J. Am. Chem. Soc.*, vol. 81, p. 1622, 1998.

[20] Y. Liang, *Ceram. Int.*, vol. 38, p. 119, 2012.

[21] O. Lupan, T. Pauporte, L. Chow, B. Viana, F. Pelle, L. Ono, B. Roldan Cuenya and H. Heinrich, *Appl. Surf. Sci.,* vol. 256, p. 1895, 2010.

[22] T. Yoshida, D. Komatsu, N. Shimokawa and H. Minoura, *Thin Solid Films,* Vols. 451-452, p. 166, 2004.

[23] M. Kemell, F. Dartigues, M. Ritala and M. Leskela, *Thin Solid Films,* vol. 434, p. 20, 2003.

[24] M. Choi, D. Choi, M. Jin, I. Kim, J. Choi, S. Lee, J. Kim and S. Kim, *Adv. Mater.*, vol. 21, p. 2185, 2009.

[25] Z. Wang, B. Huang, X. Qin, X. Zhang, P. Wang, J. Wei, J. Zhan, X. Jing, H. Liu, Z. Xu, H. Cheng, X. Wang and Z. Zheng, *Mater. Lett.*, vol. 63, p. 130, 2008.

[26] J. Tauc, R. Grigorovici and A. Vancu, *Phys. Status Solidi B,* vol. 15, p. 627, 1966.

[27] P. Banerjee, W. Lee, K. Bae and G. Rubloff, *J. Appl. Phys.,* vol. 108, p. 043504, 2010.

[28] J. Lin and J. Wu, *Appl. Phys. Lett.*, vol. 92, p. 134193, 2008.

[29] O. Baka, A. Azizi, S. Velumani, G. Schmerber and A. Dinia, *J. Mater. Sci. Mater. Electron.,* vol. 25, p. 1761, 2014.

[30] F. Wang, J. H. Seo, Z. Li, A. V. Kvit, Z. Ma and X. Wang, *ACS Appl. Mater. Inter.* , vol. 6, p. 1288, 2014.

[31] H. Lee, H. Huang and C. Tee, *Appl. Phys. Express*, vol. 5, p. 122302, 2012.

[32] N. N. Greenwood and A. Earnshaw, Chemistry of the Elements, Oxford: Pergamon Press, 1984, p. 254.

[33] M. Pourbaix, Atlas of Electrochemical Equilibria in Aqueous Solutions, Houston: National Association of Corrosion Engineers, 1974, pp. 324-325, 408-409, 495.

[34] T. Mitsunaga, *The Rigaku Journal,* vol. 25, 2009.

# 4 Electrochemical deposition of fullerene-doped ZnO nanostructured films

## 4.1 Introduction

Third generation solar technologies are currently being developed to respond to the challenges of increasing global energy demands and environmental sustainability. These include hybrid solar cells that combine nanostructured inorganic semiconductors with organic materials. It has the advantages of solution processing, low-temperature processing, and capability of printing on flexible substrates.

One of the many factors contributing towards developing a device fit for commercialization is the interfacial layers. Found between the charge separation and charge collection interfaces, and they play a crucial role in determining the efficiency and lifetime of hybrid solar cells. The need for interfacial layers arises from the following issues: large exciton binding energies in organic semiconductors, tradeoff between short exciton diffusion distance and large absorption thickness of organic absorbers, demand for charge selectivity at electrode interfaces, low stability of organic semiconductors, and the role of Ohmic contact in determining open circuit voltages for hybrid solar cells [1]. As a result, the introduction of appropriate interfacial layers has become a significant approach in obtaining devices with high power conversion efficiencies and high stability.

The ZnO film is an effective interfacial layer by itself as it has proper energy levels for electron extraction and hole blocking, a wide band gap, and sufficient conductivity. And growing ZnO thin films on transparent conducting oxides by electrochemical deposition which is known to be a low temperature and low-cost technique. In Chapter 2, ZnO thin films grown by electrochemical deposition had a nanorod array morphology growing perpendicular to the substrate.

Because of the chemical compatibility with the common fullerene acceptor in the active layer, fullerene-based interfacial layers are interesting options. Improved device performance is realized by the fullerene interlayer modulating the electronic and orbital interactions at the upper and bottom interfaces [2]. Reports of the use of fullerene interlayers have been positive with observations such as enhancement of charge carrier separation [3], charge transfer, and reduction of series resistance [4, 5, 6]. Reduced surface defect states via passivation by fullerenes have also been reported [7].

Currently, there are limited reports on this topic as the solubility of fullerenes has proven to be challenging. In this study, the water-soluble fullerene derivative, $C_{60}$ pyrrolidine tris-acid (CPTA) is used as a dopant. As seen in Figure 4.1, CPTA has suitable band energy to aid the cascading band alignment in the hybrid solar cells fabricated in this study. The LUMO of CPTA is intermediate to the work function of ZnO and the LUMO of PCBM. Its position between the ZnO and the organic layer will aid in establishing an Ohmic contact between the layers. Compared with previous works, the method of incorporating the fullerene interlayer by electrochemical deposition is novel. Previous works have incorporated fullerene derivatives as interlayers by way of spin-coating or adding the fullerenes in the ZnO precursor [3] [4]. To the best of our knowledge, there has yet to be any publication on the topic of fullerene incorporation in ZnO by the electrochemical deposition process.

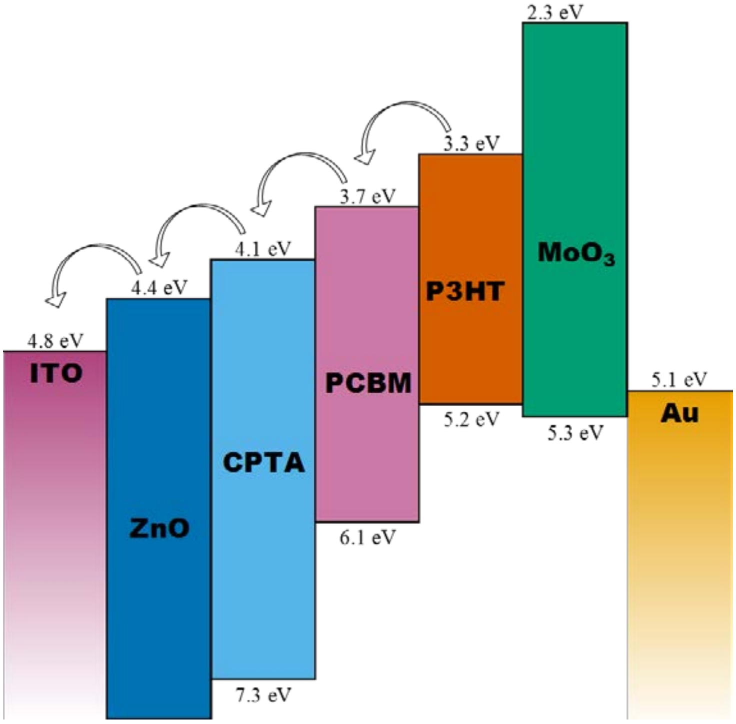

Figure 4.1 Energy diagram of the device

Here, the growth of fullerene-doped zinc oxide thin films by electrochemical deposition as interfacial layers for hybrid solar cells is investigated. By using the same technique to deposit the ZnO and the fullerene interlayer, the process of incorporating the fullerene derivative in the hybrid solar cell device is simplified. In the same step, ZnO and fullerene are deposited on the substrate. The simplification of steps during fabrication is appealing towards low-cost fabrication.

In this study, a water-soluble fullerene derivative, $C_{60}$ pyrrolidine tris-acid (CPTA) is added to the electrolyte as the dopant source. CPTA was used as purchased from Sigma-Aldrich. The fullerene derive has a pyrrolidine functional group to which three carboxylic functional groups are attached.

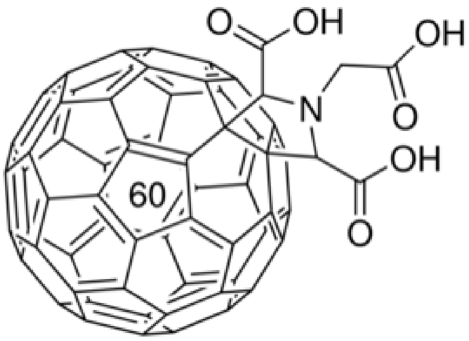

Figure 4.2 $C_{60}$ Pyrrolidine tris-acid (CPTA) [8]

## 4.2 Experimental

This section describes the methods in preparing fullerene-doped ZnO films by electrochemical deposition on ZnO-seeded ITO substrates. Fullerene doping is achieved by adding dissolved CPTA to the electrolyte. These films were then used to fabricate hybrid solar cells to evaluate their performance as cathode buffer layers.

### 4.2.1 Electrodeposition

Fullerene-doped films were electrodeposited on ZnO-seeded ITO/glass substrates in a chloride electrolyte with a rotating disk electrode set-up. The electrolyte contained 0.05 M KCl and 3 mM $ZnCl_2$. CPTA was first dissolved in water before adding it to the electrolyte solution. This will ensure proper mixing of the CPTA into the electrolyte. The CPTA solution is prepared by dissolving 2 mg of CPTA in 10 mL of water; it is then placed in the ultrasonicator for 10 min to aid in mixing and to break-up large clumps of powder. The solution has an orange-brown color. After the addition of the CPTA solution to the electrolyte, the total volume of the electrolyte is 310 mL.

The electrolyte was kept at 70°C and saturated with oxygen prior to and during deposition. Electrodeposition proceeded on the working electrode rotating at 300 rpm for 300 s using zinc wire as a counter electrode. A potential pulse, cycling between -1.0V and 1.0V was applied.

### 4.2.2 Hybrid solar cell fabrication and characterization

The hybrid solar cells were fabricated by first spin-coating an active layer of poly(3-hexylthiophene) (P3HT) and phenyl-C61-butyric acid methyl ester (PCBM) on the electrodeposited AZO film. The solution was prepared with a 30 mg/mL of 1:1 P3HT:PCBM in 1:1 chlorobenzene:trichlorobenzene. The spin-coated samples were kept in a container purged with nitrogen and allowed to dry slowly. After the active layer had dried, a molybdenum oxide ($MoO_3$) film as hole transport layer and a gold film as high work-function electrode were subsequently deposited by vacuum deposition through a shadow mask.

## 4.3 Fullerene-doped ZnO nanostructured films

The deposited fullerene-doped ZnO films were transparent to the naked eye, similar to that of undoped ZnO films. However, by observing the reflection of light off the films, the fullerene-doped films give off a yellowish reflection as compared to the greenish reflection given off by the undoped ZnO film. A similar color change was observed when CPTA solution was coated on ZnO nanorod arrays [6].

Two fullerene-doped ZnO nanostructured films were deposited following the method outlined in above. The difference in fabrication is the time when the CPTA was introduced to the system. For the first sample, referred to as “ZnO C60-1”, the CPTA solution was added right before starting the electrodeposition process. That is, at deposition time, $t_d = 0$ s. For the second film, referred to as “ZnO C60-2”, the CPTA solution was added in at $t_d = 150$ s. The rationale for this methods is that an initial layer of ZnO nanorods is first deposited on the seeded ITO substrates before the fullerene-doped ZnO is deposited. Just as in Chapter 3, the initial layer of ZnO will act as a buffer layer as well as a template to grow the fullerene-doped ZnO film.

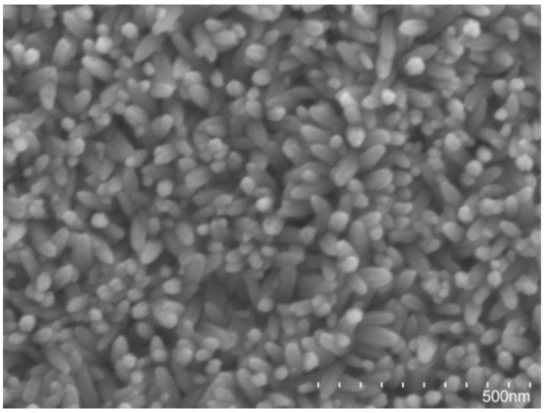

Figure 4.3 SEM image of ZnO C60-1 ($t_d = 0$ s)

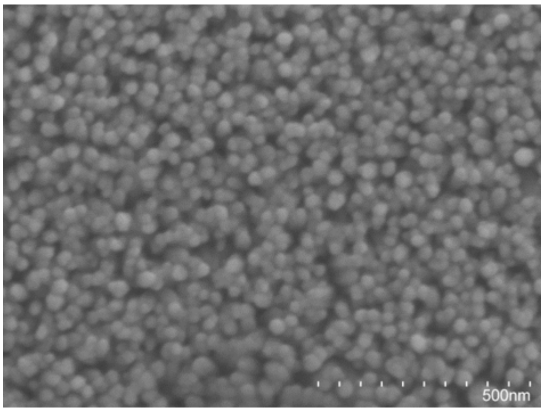

Figure 4.4 SEM image of ZnO C60-2 ($t_d = 150$ s)

Figure 4.1 and Figure 4.2 show the SEM images of fullerene-doped ZnO films. Both films are made up of nanorods with about 50 nm diameters. The difference between the orientations of the nanostructures is evident. The nanorods in ZnO C60-1 ($t_d$ = 150 s) grow in random directions while the nanorods in ZnO C60-2 ($t_d$ = 150 s) grow in a single direction perpendicular to the substrate.

This indicates that the presence of CPTA at the beginning of the electrodeposition process affects the initial nucleation of the doped ZnO film. For the case where CPTA is added in later, the highly oriented nanorod array deposited in the initial 150 s of deposition served as a template for the successive deposition of doped ZnO film. For ZnO C60-1, even though the nanorods grew in random directions, the unevenness of the nanostructured film is not severe. That is, the organic active layer can still completely cover the irregular surface structures, unlike the micron-sized hexagonal flakes discussed in previous chapters.

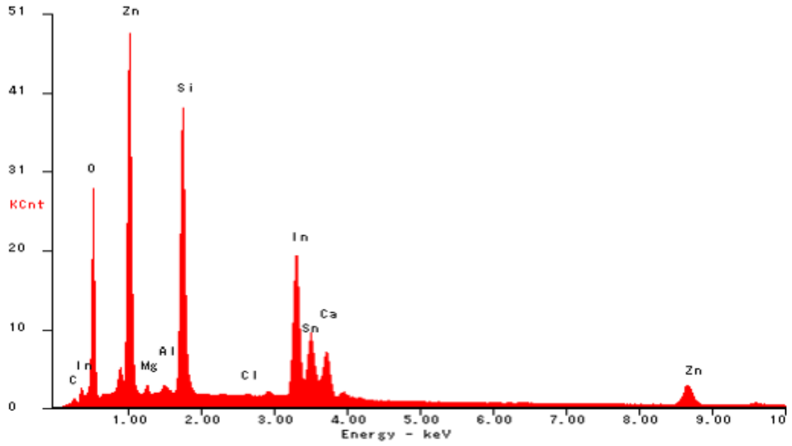

Figure 4.5 EDX Spectrum of ZnO C60-1

The presence of fullerene in the film was observed by EDX analysis on ZnO C60-1 and on undoped ZnO samples. An EDX spectrum for ZnO C60 is shown in Figure 4.5. The atomic % of Zn and C for an undoped ZnO film and for ZnO C60 is presented in Table 1. The larger

C/Zn ratio of the fullerene-doped ZnO indicates the incorporation of the fullerene into the ZnO matrix.

Table 1 EDX Atomic % concentration

| | Zn | C | C/Zn |
|---|---|---|---|
| ZnO | 13.43 | 2.4 | 0.18 |
| ZnO C60-1 | 11.36 | 2.52 | 0.22 |

The optical transmittance of the films were measured by UV-Vis spectrometry. Both films possess high optical transmittance comparable to undoped ZnO at about 80 to 90% in the visible region. The high optical transmittance can be attributed to the small size of the nanorods. Tauc plot analysis was performed on the optical transmittance spectra to estimate the bandgap. Both films had estimated bandgaps of about 3.35 eV, close to that of undoped ZnO at 3.3 eV.

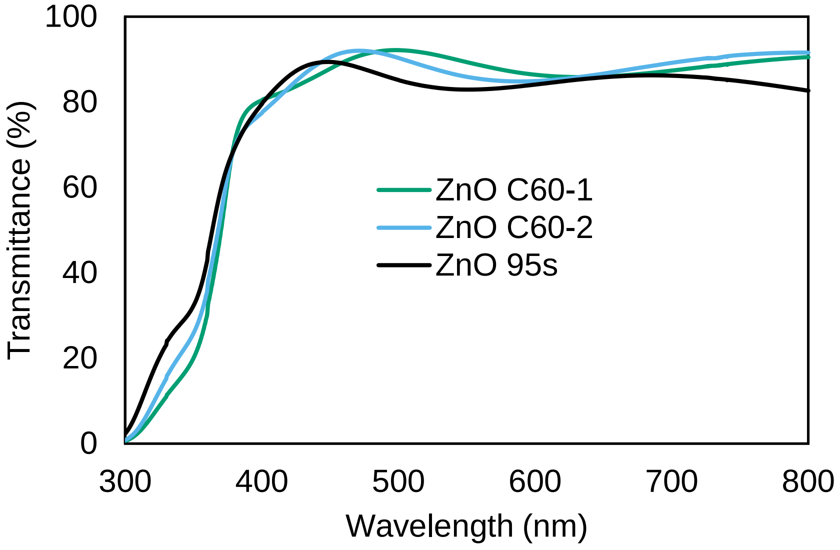

Figure 4.6 Optical transmittance of fullerene-doped ZnO samples

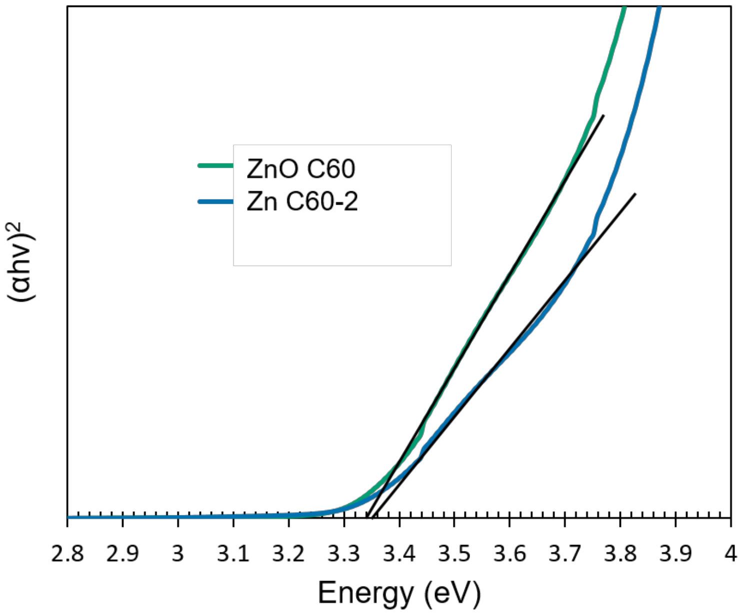

Figure 4.7 Tauc plot of ZnO C60 samples

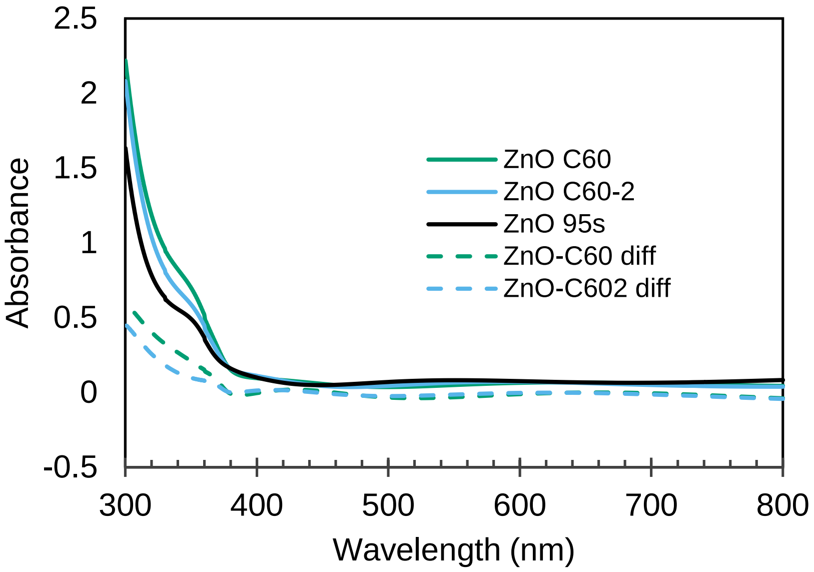

Figure 4.8 Absorbance spectra of undoped and fullerene-doped ZnO samples

Figure 4.8 shows the absorbance spectra of the undoped ZnO and fullerene-doped ZnO samples. These were derived from the UV-Vis optical transmittance spectra of the samples. The variance in the spectra of the doped and undoped samples can be seen below 400 nm.

Above 400 nm, the spectra of the samples are very similar. The dashed lines represent the difference between the absorbance spectra of the fullerene-doped film and the undoped ZnO. The difference between these spectra indicate fullerene incorporation because the shape of the spectral difference corresponds to the absorbance of fullerenes. The shape of the spectral difference is similar to the absorbance spectra of pyrrolidino(60)fullerene derivatives, where the absorbance is high from 300 and decreases to 0 a little bit over 400 nm [9].

The *JV*-characteristics of the fullerene-doped ZnO films together with undoped ZnO film is shown in Figure 4.8 and the summary of the device parameters are shown in Table 2. The undoped ZnO film was grown in the same conditions as the fullerene doped films, just without the addition of the CPTA solution.

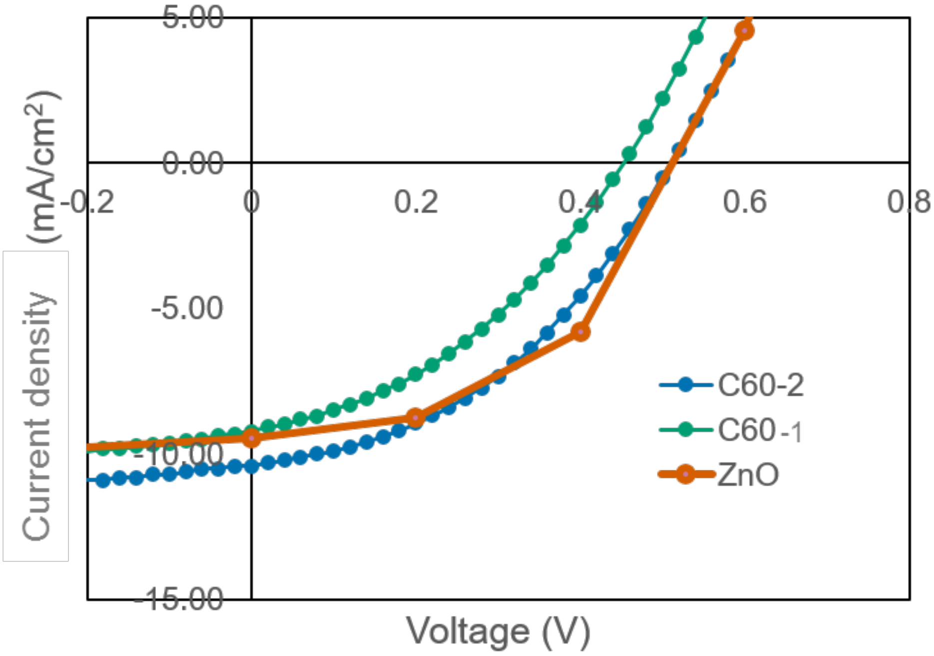

Figure 4.9 *JV*-characteristic of undoped ZnO and ZnO C60 samples

Among the three samples, the device made from undoped ZnO had the best *PCE* at 2.32%. The higher *PCE* between the fullerene-doped films was obtained from ZnO C60-1 at 2.20%.

ZnO C60-2 had the highest $J_{SC}$ at 10.38 mA/cm$^2$ while that of ZnO C60 is almost the same as the undoped ZnO.

The $V_{OC}$ of undoped ZnO and ZnO C60-2 are similar 0.51 V while ZnO C60-1 is at 0.45 V. The largest difference in parameters between the fullerene-doped and undoped samples is seen in the values of *FF*. The undoped ZnO sample had *FF* of 47.9 while the fullerene-doped samples possessed 41.5 (ZnO C60-2) and 38.2 (ZnO C60-1). Although the fullerene-doped samples had better shunt resistance compared to the undoped sample, their series resistance was worse.

The series resistance in the device is attributed to the bulk conductivity of each of the functional layers and the contact resistance between them [10]. An increase in the series resistance is produced due to poor conductivity through the functional layers and reduced charge carrier injection to the electrodes [11].

Table 2 Summary of device parameters, average and standard deviation in brackets.

| | $J_{SC}$ (mA/cm$^2$) | $V_{OC}$ (V) | *FF* | *PCE* (%) | Series Resistance (ohm) | Shunt Resistance (ohm) |
|---|---|---|---|---|---|---|
| ZnO C60-2 | 10.38<br>[10.03±0.56] | 0.51<br>[0.50±0.007] | 41.5<br>[36.54±4.70] | 2.20<br>[1.84±0.35] | 235<br>[313±96] | 3003<br>[2224±708] |
| ZnO C60-1 | 9.21<br>[8.47±1.28] | 0.45<br>[0.45±0.004] | 38.2<br>[39.2±1.66] | 1.56<br>[1.50±0.15] | 255.4<br>[263±14] | 2145<br>[2303±14] |
| ZnO | 9.46<br>[9.13±0.40] | 0.51<br>[0.51±0.005] | 47.9<br>[49±3.0] | 2.32<br>[2.28±0.06] | 188.5<br>[169±24] | 878.8<br>[849±42] |

The higher series resistance in the fullerene-doped samples indicate that charge carrier injection to the electrode is reduced compared to undoped ZnO. It might be caused by the presence of CPTA in the bulk of the ZnO nanorod crystals. The larger series resistance may be attributed to the lower crystal quality of the ZnO nanorod bulk for transport as fullerene incorporation in the bulk will disrupt the ZnO crystal matrix.

On the other hand, the fullerene-doped samples exhibit improved shunt resistances. Shunt resistance is determined by the quality of the functional films and their interfaces [10]. A larger value of shunt resistance is favored in solar cell devices. Reduction in shunt resistance is produced due to imperfections within the photoactive film or current leaks at the interface between the layers in the device [11]. The improved shunt resistance of the fullerene-doped samples indicate reduced leakage current and improved charge transfer at the interface of ZnO and the organic active layer. Previous studies on the incorporation of fullerene derivatives as interlayers between metal oxides and organic active layers have shown that the fullerene interlayer can passivate electron traps on the surfaces of metal oxides such as ZnO and $TiO_2$ [12]. In the electrodeposition of fullerene-doped ZnO, fullerene was incorporated not only in the bulk of the nanorod but also on its surfaces. The fullerenes on the surface of the ZnO may passivate the surface defects. As a result of passivation, recombination of carriers is suppressed particularly at the interfaces. This brings about a decrease in the leakage current which manifests as an increase in the shunt resistance of the device.

## 4.4 Summary

The interfacial layers in hybrid solar cells, found between the interfaces of the charge separation and charge collection, play a crucial role in determining the efficiency and lifetime of the devices. While fullerene-based interfacial layers are compatible materials, there are only limited publications on the topic.

In this research, fullerene-doped ZnO interfacial layers were grown by developing a novel electrochemical deposition technique using the water soluble fullerene derivative, $C_{60}$ pyrrolidine tris-acid (CPTA). Nanorod structures were successfully grown. By adding the CPTA solution after an initial layer of highly ordered ZnO nanorods were grown, a highly ordered doped ZnO film was grown. The doped films were then used to fabricate hybrid solar cells with organic active layers to determine the effect of the fullerene/ZnO layer on the devices.

Compared to the hybrid solar cell fabricated using undoped ZnO, the devices fabricated using the fullerene-doped ZnO had a larger series resistance and shunt resistance. The larger series resistance could be attributed to the incorporation of fullerene in the ZnO bulk. The fullerene disrupts the ZnO crystal matrix and degrades the conductivity of the crystal thereby increasing series resistance.

The improvement in shunt resistance indicates an improvement in charge transfer at the interface between ZnO and the active layer. This can be attributed to the fullerenes deposited on the surface of the ZnO film. Fullerenes have been shown to passivate surface defects. As a result, recombination is suppressed particularly at the interface of ZnO and the active layer.

Because fullerene doping improves shunt resistance due to incorporation of fullerenes at the surface but degrades series resistance due to incorporation of fullerenes in the bulk, an improved fullerene-doped ZnO film grown by electrochemical deposition should consider selective doping on the surface of the film. Incorporation of fullerenes on the surface while preventing incorporation of fullerene in the bulk should reduce the series resistance while maintaining the improvement in shunt resistance. One way this could be done is by introducing the dopant source much later in the deposition.

# References

[1] J. Lian, Y. Yuan, E. Peng and J. Huang, "Interfacial Layers in Organic Solar Cells," in *Organic and Hybrid Solar Cells*, Switzerland, Springer, 2014, p. 121.

[2] C. H. Hsieh, Y. J. Chen, P. J. Li, C. H. Chen, M. Dubosc, R. M. Liang and C. S. Hsu, *J. Am. Chem. Soc.*, vol. 132, p. 4887, 2010.

[3] Y. Vaynzof, D. Kabra, L. Zhao, P. K. H. Ho, A. T. S. Wee and R. H. Friend, *Appl. Phys. Lett.*, vol. 97, p. 033309, 2010.

[4] T. Stubhan, M. Salinas, A. Ebel, F. C. Krebs, A. Hirsch, M. Halik and C. J. Barbec, *Adv. Energy Mater.*, vol. 5, p. 532, 2012.

[5] P. Li, G. Sun, J. Li, T. Jiu and J. Fang, *Solar Energy Mater. Solar Cells*, vol. 126, p. 36, 2014.

[6] P. Zhong, W. Que, Y. N. Liang, X. Yin, Y. Liao, L. B. Kong and X. Hu, *RSC Advances*, vol. 3, p. 17904, 2013.

[7] C. T. Chen, F. C. Hsu, S. W. Kuan and Y. F. Chen, *Solar Energy Mater. and Solar Cells*, vol. 95, p. 740, 2011.

[8] "C60 ピロリジントリス-酸 97% | Sigma-Aldrich," 31 December 2015. [Online]. Available: http://www.sigmaaldrich.com/catalog/product/aldrich/709085?lang=ja&region=JP.

[9] C. Du, J. Xu, Y. Li, W. Xu and D. Zhu, *Chinese Sci. Bull.,* vol. 46, p. 1156, 2001.

[10] H. L. Yip, S. K. Hau, N. S. Baek, H. Ma and A. K. Y. Jen, *Adv. Mater.,* vol. 20, p. 2376, 2008.

[11] Z. Ge, S. Chen, R. Peng and A. Islam, in *Organic and Hybrid Solar Cells*, H. Huang and J. Huang, Eds., Switzerland, Springer Intl. Pub., 2014.

[12] L. Hu, L. Chen, X. Hu and Y. Chen, *J. Mater. Chem. C,* vol. 2, p. 10282, 2014.

[13] S. P. Anthony, J. I. Lee and J. K. Kim, "Tuning optical bandgap of vertically aligned ZnO nanowire arrays grown by homoepitaxial electrodeposition," *Applied Physics Letters,* vol. 90, p. 103107, 2007.

[14] M. Ohyama, H. Kozuka and T. Yoko, *J. Am. Chem. Soc.*, vol. 81, p. 1622, 1998.

# 5 Conclusion

## 5.1 Conclusions

The application of nanostructures in hybrid solar cells have been shown to be a good strategy in improving its performance. One-dimensional nanostructures, with direct paths for a charge transport and high surface area for light harvesting, are emerging as promising candidates for building solar cells. A method suitable for the low cost fabrication of ZnO nanostructure films is electrochemical deposition. Its versatile, low temperature, and fast production philosophy is in line with the goal to produce more affordable devices. It is important, therefore, to understand controlled nanostructure growth for electrodeposited ZnO to be successful in hybrid solar cell applications. Furthermore, methods to tailor the optoelectronic properties and interfaces of the ZnO by electrodeposition should be developed and analyzed.

The significant results that this study contributes are summarized. First, the role of nucleation and the concentration of KCl towards the control of nanorod microstructure were demonstrated. Second, nanostructured Al-doped ZnO from chloride electrolyte was demonstrated with $AlCl_3 \cdot 6H_2O$ as dopant source. Bandgap widening arising from Al doping shows that this method is a useful way of changing the optoelectronic properties of the film. And third, deposition of fullerene-doped ZnO by electrodeposition from a chloride electrolyte was demonstrated with CPTA as dopant source. These results and analysis are valuable in developing nanostructured ZnO films through structural control and doping for hybrid solar cell applications.

Due to the morphology and surface energy of ITO, electrodeposition of ZnO nanorod arrays on bare ITO substrates is not straightforward. In Chapter 1, a ZnO seed layer is deposited on ITO by sol-gel deposition. The ZnO seed layer was shown to promote the growth of highly ordered nanorods with homogeneous diameters. Its effect on the nucleation was observed through the chronoamperometric transient curves which indicated simultaneous nucleation and fast nuclei coalescence.

Micron-sized hexagonal flakes, however, grew together with the nanorod array. Due to their large size, they are incompatible for the inverted hybrid solar cells fabricated in this study. Because Cl- ions preferentially adsorbed on the Zn (0001) plane favor the growth of flakes, decreasing the concentration of the supporting electrolyte, KCl, from 0.1 M to 0.05 M was shown to be successful in inhibiting the number and size of hexagonal flakes. Decreased KCl concentration also favored the growth of nanorods with tapered tips. In addition, the evolution of the nanorod array structure to a thick and compact ZnO film was seen through long deposition times (30 and 60 min). Following these guidelines, a more optimized ZnO nanostructured film was grown. Its function as a cathode buffer layer was demonstrated in a hybrid solar cell device (*PCE* = 2.9%). A summary of the best device characteristics are shown in Table 5.1.

Deposition of Al-doped ZnO by electrodeposition from a chloride electrolyte was demonstrated with $AlCl_3{\cdot}6H_2O$. The presence of Al in the ZnO film was confirmed by EDX and XPS analysis. Studying the Al2p spectra of the doped ZnO film suggest that Al is incorporated into ZnO by substitution of Zn. Bandgap widening was observed for Al-doped ZnO films. Nanorod arrays were obtained from electrolytes with Al/Zn ratio 0.5% (3 mM $ZnCl_2$). However, the growth of hexagonal flakes was not inhibited by decreasing the KCl concentration from 0.05 M to 0.025M. Furthermore, the dopant decreased the pH of the electrolyte resulting in the corrosion of the ZnO seed layer. These suggests that the growth mechanism for the flakes in this particular electrolyte is different and cannot simply be explained by preferred adsorption of $Cl^-$ ions to the ZnO (0001) plane. Due to the presence of hexagonal flakes, the performance of a device with undoped ZnO is better. The highest *PCE* obtained for a device with Al-doped ZnO nanostructured film was 1.7%.

Table 5.1 Summary of device characteristics of the best devices per chapter

| | *Voc* (V) | *Jsc* (mA/cm$^2$) | *FF* (%) | *PCE* (%) |
|---|---|---|---|---|
| Ch. 2: ZnO NR | 0.51 | 12.19 | 46.92 | 2.92 |
| Ch. 3: 0.5% AZO (ZnO seeded) | 0.44 | 8.94 | 43.4 | 1.71 |
| Ch. 4: ZnO C60-2 | 0.51 | 10.38 | 41.5 | 2.20 |

Deposition of fullerene-doped ZnO by electrodeposition from a chloride electrolyte was demonstrated with water-soluble fullerene derivative, CPTA, as dopant source. Nanorod structures were grown and the films had high optical transmittance. The presence of fullerene in the ZnO was confirmed by EDX where a higher C/Zn ratio was measured for the fullerene-doped ZnO than undoped ZnO. Hybrid solar cells with fullerene-doped ZnO had larger series resistance and shunt resistance. The larger series resistance may be attributed to the lower crystal quality of the ZnO nanorod bulk for transport as a result of fullerene incorporation. The favorable increase in the shunt resistance, on the other hand, could be attributed to reduced surface defect states via passivation by fullerenes to reduce the leakage current. The highest *PCE* obtained for a device with fullerene-doped ZnO nanostructured film was 2.2%.

## 5.2 Suggestions for future work

This study was able to show the electrodeposition of ZnO nanostructured films and their application in inverted hybrid solar cells. In addition, by doping Al and fullerene into ZnO, changing the optoelectronic property and interfacial property of the ZnO film was demonstrated. There are still issues and challenges to clarify.

1. Low temperature ZnO seed layer deposition

   In this study, ZnO seed layer deposition was achieved by sol-gel method. This includes heating in an oven for 350 $^{o}$C. For this technique, the high temperature was recognized to favor the preferential growth of nanocrystals along the c-axis.

   As it is, the sol-gel method is successful in aiding nucleation of nanorod arrays but it makes the process incompatible with a wider array of substrates, in particular most flexible substrates. An advantage of growing ZnO on flexible substrates is its application in roll-to-roll process. This process is appealing for its efficient and low-cost production of solar cells and other devices on flexible substrates.

   Finding a low-temperature method to deposit the seed layer will be beneficial towards the goal of fabricating more affordable devices.

2. Understand chlorine doping

This study has demonstrated ZnO deposition methods all from chloride electrolytes. Previous studies on the electrodeposition of ZnO from a chloride based electrolyte have reported on the incorporation of chlorine in their ZnO nanostructures. While the effect of decreasing the chlorine ion concentration to control the nanostructure has been explored in this study, understanding the mechanism of chlorine doping is interesting due to its effect on the optoelectronic properties of the film. How it chlorine doping manifests during growth of doped ZnO has yet to be understood.

3. Understand the mechanism of hexagonal flake growth for electrodeposition of Al-doped ZnO.

In Chapter 3, several attempts were undertaken to inhibit the growth of hexagonal flakes. Results indicate, however, that decreasing the chlorine content is not effective and that the low pH caused by the addition of $AlCl_3 \cdot 6H_2O$ corrodes the ZnO seed layer. These suggest that the growth of hexagonal flakes cannot be simply explained by the preferential adsorption of $Cl^-$ ions on the ZnO (0001) plane. In order to grow more optimized Al-doped nanostructured films, the mechanism of growth needs to be understood.

To inhibit the growth of hexagonal flakes, one strategy is to further decrease the concentration of $AlCl_3 \cdot 6H_2O$ in the electrolyte while also growing a buffer layer of ZnO. In Chapter 2, it was shown that a ZnO-seeded ITO substrate promotes high density nucleation which is conducive for the growth of nanorod arrays. Growing a ZnO buffer layer will make sure the AZO film is grown on nanostructured ZnO layer instead of on bare ITO. While electrodeposition of AZO on a ZnO buffer layer was demonstrated in Chapter 3, it was grown from an electrolyte with Al/Zn ratio of 2.5%. In Chapter 3, it was also shown that decreasing the Al/Zn ratio in the electrolyte affected the morphology of the film. At Al/Zn ratio 2.5%, the film had a morphology of interconnected hexagonal flakes. Decreasing the Al/Zn ratio to 0.5% lead to the growth of nanorod arrays with isolated hexagonal flakes. Growing AZO on a ZnO buffer layer using an electrolyte with Al/Zn ratio of 0.5% or lower may lead to the growth of AZO nanorod arrays without hexagonal flakes.

Using a different dopant source, for example aluminum nitrate $Al(NO_3)_3{\cdot}9H_2O$, is also an interesting point of further study. In this study, $AlCl_3{\cdot}6H_2O$ is used as the dopant source. Comparing the effects of these dopants on the resulting morphology might elucidate the role of $Al^{3+}$ ion on the growth mechanism of hexagonal flakes. In Chapter 2, it was shown that decreasing the concentration of KCl in the electrolyte to 0.05M inhibits the growth of hexagonal flakes as this decreases the adsorption of $Cl^-$ ions to the (0001) plane. In Chapter 3, however, hexagonal flakes were still grown even with decreased KCl concentration at 0.025M. By using a nitrate-based dopant, the $Cl^-$ ion concentration in the electrolyte can be decreased further.

4. Perform selective doping od CPTA on the surface of ZnO film

In Chapter 4, fullerene-doped ZnO was grown by electrochemical deposition. Compared to hybrid solar cells fabricated with undoped ZnO, devices fabricated with fullerene-doped ZnO exhibited increased series resistance and increased shunt resistance. The beneficial increase in the shunt resistance could be attributed to the incorporation of CPTA on the surface of the ZnO. Here, the fullerene can passivate surface defects and suppress recombination. On the other hand, the detrimental increase of the shunt resistance could be attributed to the incorporation of CPTA in the bulk of the ZnO crystal. The presence of fullerene in the bulk disrupts the crystal lattice thereby degrading the conductivity of ZnO.

An improved film with increased shunt resistance and decreased series resistance could be grown by selective doping of the CPTA on the surface of the nanostructured ZnO film. Avoiding incorporation of CPTA in the bulk might improve the series resistance of the device. Selective doping on the surface of the ZnO can be achieved by introducing CPTA solution much later in the process of deposition.

# List of Publications

1. J. Damasco Ty, N. Dannehl, D. Schlettwein and H. Yanagi, “Hybrid Organic-Inorganic Solar Cells with Electrodeposited Al-doped ZnO”, J. Nanosci. Nanotechnol., Accepted.
2. J. Damasco Ty and H. Yanagi, “Electrochemical Deposition of Zinc Oxide Nanorods for Hybrid Solar Cells”, Jpn. J. Appl. Phys. 54, 04DK05 (2015).